DISCLAIMER

This report was prepared as an account of work sponsored by an agency of the United States Government. Neither the United States Government nor any agency thereof, nor any of their employees, makes any warranty, express or implied, or assumes any legal liability or responsibility for the accuracy, completeness, or usefulness of any information, apparatus, product, or process disclosed, or represents that its use would not infringe privately owned rights. Reference herein to any specific commercial product, process, or service by trade name, trademark, manufacturer, or otherwise does not necessarily constitute or imply its endorsement, recommendation, or favoring by the United States Government or any agency thereof. The views and opinions of authors expressed herein do not necessarily state or reflect those of the United States Government or any agency thereof. Reference herein to any social initiative (including but not limited to Diversity, Equity, and Inclusion (DEI); Community Benefits Plans (CBP); Justice 40; etc.) is made by the Author independent of any current requirement by the United States Government and does not constitute or imply endorsement, recommendation, or support by the United States Government or any agency thereof.

SANDIA REPORT

SAND2026-16676
Printed January 2026

Sandia National Laboratories

Modeling Material Interfaces with the Six-Equation Model in FLEXO

Griffin S. Cearley, Alan K. Stagg, Jeffery M. Woolstrum, Michael M. Crockatt, Brian N. Granzow

Prepared by
Sandia National Laboratories
Albuquerque, New Mexico 87185
Livermore, California 94550

Issued by Sandia National Laboratories, operated for the United States Department of Energy by National Technology & Engineering Solutions of Sandia, LLC.

NOTICE: This report was prepared as an account of work sponsored by an agency of the United States Government. Neither the United States Government, nor any agency thereof, nor any of their employees, nor any of their contractors, subcontractors, or their employees, make any warranty, express or implied, or assume any legal liability or responsibility for the accuracy, completeness, or usefulness of any information, apparatus, product, or process disclosed, or represent that its use would not infringe privately owned rights. Reference herein to any specific commercial product, process, or service by trade name, trademark, manufacturer, or otherwise, does not necessarily constitute or imply its endorsement, recommendation, or favoring by the United States Government, any agency thereof, or any of their contractors or subcontractors. The views and opinions expressed herein do not necessarily state or reflect those of the United States Government, any agency thereof, or any of their contractors.

Printed in the United States of America. This report has been reproduced directly from the best available copy.

Available to DOE and DOE contractors from

U.S. Department of Energy
Office of Scientific and Technical Information
P.O. Box 62
Oak Ridge, TN 37831

Telephone: (865) 576-8401
Facsimile: (865) 576-5728
E-Mail: reports@osti.gov
Online ordering: http://www.osti.gov/scitech

Available to the public from

U.S. Department of Commerce
National Technical Information Service
5301 Shawnee Road
Alexandria, VA 22312

Telephone: (800) 553-6847
Facsimile: (703) 605-6900
E-Mail: orders@ntis.gov
Online order: https://classic.ntis.gov/help/order-methods

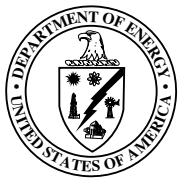

ABSTRACT

FLEXO is a multiphysics code developed at Sandia National Laboratories for predictive simulation of pulsed power target physics with extended magnetohydrodynamics modeling. Given this application space, FLEXO must be able to perform high-fidelity simulations of pulsed-power systems that include multiple materials. This work presents the augmentation of FLEXO with a six-equation model for multimaterial flow. We design and analyze discretizations of the six-equation model, emphasizing desirable properties for robust multimaterial simulation. We also present solution limiting, bounds preservation, and pressure equilibration/relaxation techniques that enhance the robustness of the overall multimaterial scheme. We present a suite of test problems to document these new capabilities of the FLEXO code.

Acknowledgment

We would like to acknowledge helpful collaboration with Thomas Voth, Nathaniel Hamlin, Matthew Martin, Kyle Cochrane, and Thomas Gardiner. We would also like to acknowledge Steve Bova and Luke Shulenburger for project management and funding support.

This page intentionally left blank.

CONTENTS

LIST OF FIGURES

This page intentionally left blank.

ACRONYMS & DEFINITIONS

FLEXO Flux-Limited Extended-MHD Ohm's Law

XMHD Extended magnetohydrodynamics

MagLIF Magnetized Liner Inertial Fusion

DG Discontinuous Galerkin

GPU Graphical processing unit

EOS Equation of state

RKDG Runge-Kutta discontinuous Galerkin

LLF Local Lax-Friedrichs

HLL Harten-Lax-van Leer

HLLC Harten-Lax-van Leer-Contact

This page intentionally left blank.

1. INTRODUCTION

Flux-Limited Extended-MHD Ohm's Law (FLEXO) is a multiphysics code for simulating target physics on pulsed-power systems with extended magnetohydrodynamics (XMHD) modeling featuring Hall physics [36]. Multimaterial modeling is crucial for these targets, which are often composed of multiple materials and exhibit complex interface hydrodynamics during compression. For example, Magnetized Liner Inertial Fusion (MagLIF) experiments [42] feature an outer liner material that is magnetically driven to implode a pre-heated lower-density fusion fuel. These targets may also feature additional layers between the liner and fuel [41], further complicating the interface dynamics during target implosion and stagnation. A great amount of effort has been expended on diagnosing, simulating, and ultimately controlling the growth of interfacial instabilities in MagLIF systems [37, 40, 49], which are a major source of degradation of the target and therefore pose a large technical barrier for the success of MagLIF. Thus, development of robust, high-fidelity, and parallelizable numerical algorithms for multimaterial physics is extremely important in this field.

The discontinuous Galerkin (DG) finite element method [9] is a numerical method that utilizes a polynomial basis of arbitrary order with compact support in each element, coupling solutions via numerical flux functions evaluated at element interfaces. This approach has received much attention from researchers in recent years, due to its arbitrary high-order accuracy and superconvergence properties [5] in addition to its compactness and parallelizability. These are ideal properties for a production-level code for designing pulsed-power targets: high-order accuracy is important for resolving the small-scale, low-density features involved in the seeding of the helical magneto-Rayleigh-Taylor instability [37, 47] as well as the potentially turbulent mixing that occurs at the liner-fuel interface. Furthermore, the method's parallelizability lends itself very well to the large, 3-D computations required for this application, including the use of graphical processing unit (GPU) architectures.

Despite these advantages, the discontinuous Galerkin method has not been applied to multimaterial or multifluid flows as extensively as might be expected. This is likely due to issues with robustness in discontinuity capturing with the DG method, as well as the complexity of applying schemes developed for single-fluid shock capturing to material interfaces, generally referred to as *interface capturing*. This approach contrasts with *interface tracking*, in which the interface is explicitly tracked, e.g., via Lagrangian tracers, mesh alterations, or a level-set function. Rather, the interface is captured via discontinuous material properties or color functions (e.g., volume fractions). Using a high-order numerical method, these discontinuous functions require application of selective dissipation to suppress oscillations. Interface capturing features a much more equitable balance of the computational burden across the domain, unlike interface tracking which concentrates computational expense in elements near the interface. This is advantageous for large parallel calculations, in which load balancing is an important consideration. Furthermore, interface capturing approaches do not require interface reconstruction or remeshing/mesh distortion, which are conceptually and

practically difficult to extend to a 3-D high-order solution. For these reasons, adoption of the DG method in the interface tracking literature has been even slower than in the interface capturing literature.

This work aims to integrate into the FLEXO code an interface capturing approach in the framework of the discontinuous Galerkin finite element method. This report is organized as follows: in Chapter 2, we describe the six-equation model used here. In Chapter 3, we describe our DG discretization for solving the phasic-total-energy six-equation model, with particular emphasis on the non-conservative terms in the model and their discretization. In Chapters 4 and 5, we describe the limiting scheme used to regularize discontinuities and the bounds-preservation scheme used to maintain physically valid states, respectively. In Chapter 6, we describe our approaches for equilibrating/relaxing material pressures, which is important for robust solution of the six-equation model. In Chapter 7, we include results for a suite of verification problems. Then, in Chapter 8, we include results for a few large-scale, application-relevant FLEXO simulations using the capabilities established in this document. In Chapter 9 we provide conclusions and discuss ongoing development areas to improve the multimaterial capabilities in FLEXO.

2. GOVERNING EQUATIONS

The single-velocity six-equation two-phase model of multimaterial flow was originally introduced by Saurel et al. [32] as an alternative to the five-equation model of Kapila [21] to circumvent some numerical issues (e.g., a non-monotonic mixture sound speed across interfaces) inherent to the five-equation model. Another benefit of the six-equation model is that it admits the use of distinct and arbitrary (i.e., from a tabular source) equation of state (EOS) for each material without the need to iterate on a common pressure. This benefit is realized because each material's energy is solved for separately. As a result, the materials may naturally be out of pressure equilibrium in mixed zones.

However, the six-equation model of Saurel et al. involves the solution of internal energies of the mixing phases, which requires the solution of an additional conservation law governing the mixture energy to ensure correct jump conditions across discontinuities. The phasic-total-energy six-equation model of Pelanti and Shuye [28, 29], which is mathematically equivalent to that of Saurel et al. (see Appendix A), was introduced to avoid this complication. Instead, the phasic (i.e., partial) total energy density of each mixing phase is evolved, implicitly enforcing overall conservation of energy. The phasic-total-energy six-equation model is written:

$$\frac{\partial}{\partial t}\alpha_k + \vec{u}\cdot\nabla\alpha_k = \sum_{j=1}^{N_m}\mu_{kj}(p_k - p_j), \tag{2.1a}$$

$$\frac{\partial}{\partial t}[\alpha_k\rho_k] + \nabla\cdot[\alpha_k\rho_k\vec{u}] = 0, \tag{2.1b}$$

$$\frac{\partial}{\partial t}[\rho\vec{u}] + \nabla\cdot[\rho\vec{u}\otimes\vec{u} + p\boldsymbol{I}] = 0, \tag{2.1c}$$

$$\frac{\partial}{\partial t}[\alpha_k\rho_k E_k] + \nabla\cdot[\vec{u}(\alpha_k\rho_k E_k + \alpha_k p_k)] + \mathcal{Y}_k = -\sum_{j=1}^{N_m} p_{I,kj}\mu_{kj}(p_k - p_j), \tag{2.1d}$$

where the index k spans the number of materials, $k = 1, .., N_m$, and $\boldsymbol{I}$ is the identity matrix. Here the material k volume fraction is α_k, partial mass density is $\alpha_k\rho_k$, and partial total energy density is $\alpha_k\rho_k E_k = \alpha_k\mathcal{E}_k + \frac{1}{2}\alpha_k\rho_k\vec{u}\cdot\vec{u}$, where $\mathcal{E}_k = \rho_k\varepsilon_k$ is the internal energy density of material k. The mixture (bulk) density is $\rho = \sum_k \alpha_k\rho_k$ and the mixture (bulk) pressure is $p = \sum_k \alpha_k p_k$. The system requires an EOS for each material pressure, $p_k = p_k(\varepsilon_k, \rho_k)$. We do not assume a form for this relationship in this work, unless otherwise stated. The system necessarily contains nonconservative terms in the volume fraction equation and energy equation, the latter of which is written as:

$$\mathcal{Y}_k = \vec{u}\cdot\left[z_k\nabla p - \nabla(\alpha_k p_k)\right]. \tag{2.2}$$

Here $z_k = \alpha_k\rho_k/\rho$ is the mass fraction of material k. The right-hand terms are the pressure relaxation source terms, which drive the pressures to equilibrate in elements where multiple materials

exist. Within these terms, $p_{I,kj} = p_{I,jk}$ is the interface pressure between materials j and k, and $\mu_{kj} = \mu_{jk}$ is the pressure relaxation coefficient between materials j and k.

We note that while the partial total energy densities of each material are not conserved due to the presence of the nonconservative and source terms, we may sum Eqn. (2.1d) over each k material to obtain a statement of conservation of the mixture (bulk) total energy $\rho E = \sum_k \alpha_k \rho_k E_k$,

$$\frac{\partial}{\partial t}[\rho E_k] + \nabla \cdot [\vec{u}(\rho E + p)] = 0, \tag{2.3}$$

thus, total energy is conserved using this modeling approach.

While this model is implemented in the FLEXO XMHD code, the discussion in this report regards the hydrodynamic equations in the context of multimaterial modeling. Thus, we defer description of the XMHD modeling, numerical solution, and capabilities to the Reference [2].

We discuss approaches to discretizing Eqns. (2.1) with the discontinuous Galerkin (DG) finite element method, with a focus on the nonconservative terms, in Chapter 3. Approaches for modeling/solution of the pressure relaxation source terms in Eqns. (2.1) are discussed in Chapter 6.

3. DISCONTINUOUS GALERKIN DISCRETIZATION

The DG method approximates the solution vector $\mathbf{q}$ using a polynomial expansion on a spatial element Ω_e, which is a subset of the domain $\Omega = \bigcup_{e=1}^{N_e} \Omega_e$, comprised of N_e elements,

$$\mathbf{q}(\vec{x})|_{\vec{x}\in\Omega_e} \approx \mathbf{q}_e = \sum_{j=1}^{N_b} \widehat{\mathbf{q}}_j^e \phi_j(x), \tag{3.1}$$

where N_b is the number of locally supported basis functions $\phi_j(x)$, which are at most P-th order. In 1-D, we utilize $N_b = P + 1$ number of Legendre basis functions for an overall solution order of P. For 2-D and 3-D calculations, we use a tensor product of the 1-D bases in each coordinate direction, resulting in $N_b = (P+1)^2$ and $N_b = (P+1)^3$ basis functions, respectively. The solution degrees of freedom $\widehat{\mathbf{q}}_j^e$ are discrete unknowns that are advanced in time.

In this chapter, we describe a selection of different approaches to discretize the governing equations, Eqns. (2.1), by the discontinuous Galerkin method. In this section, we neglect entirely the pressure relaxation source terms on the right-hand side of Eqns. (2.1), deferring discussion of their solution for later chapters. We then analyze these discretizations with emphasis on their *well-balancedness*, which is an important attribute of numerical schemes featuring nonconservative terms.

3.1. Discontinuous Galerkin Discretization for Conservative Equations

We utilize a typical Runge-Kutta discontinuous Galerkin (RKDG) method [11] for the equations in the six-equation model, Eqns. (2.1), that may be written entirely in divergence form, i.e., Eqns. (2.1b) and (2.1c). These equations can be written as,

$$\frac{\partial}{\partial t}\mathbf{q} + \nabla \cdot \vec{\mathbf{f}}(\mathbf{q}) = 0. \tag{3.2}$$

The equations that obey Eqn. (3.2) comprise the conservative subsystem of the system Eqns. (2.1).

We create the DG weak form by considering the modal expansion of the solution vector, Eqn. (3.1), in the continuous governing equations, Eqn. (3.2), mulitplying by the basis functions ϕ_i^e, and then integrating over the domain:

$$\int_{\Omega_e} \phi_i^e \frac{\partial}{\partial t}\mathbf{q}_e d\Omega + \int_{\Omega_e} \phi_i^e \nabla \cdot \vec{\mathbf{f}}(\mathbf{q}_e) d\Omega = 0, \tag{3.3}$$

where the integration becomes nonzero only within element Ω_e due to the local support of the basis function. We then apply the divergence theorem to separate the flux term into a surface integral and a volume integral,

$$\int_{\Omega_e} \phi_i^e \frac{\partial}{\partial t} \mathbf{q}_e d\Omega + \int_{\partial\Omega_e} \phi_i^e \widehat{\vec{\mathbf{f}}} \cdot \vec{n} ds - \int_{\Omega_e} \vec{\mathbf{f}}(\mathbf{q}_e) \cdot \nabla \phi_i^e d\Omega = 0. \tag{3.4}$$

Appearing in the surface integral is the numerical flux $\widehat{\vec{\mathbf{f}}}$, which due to the discontinuous nature of the solution at element interfaces must depend on the state within Ω_e as well as the element(s) sharing the surface $\partial\Omega_e$. Numerical fluxes from finite-volume schemes, such as Local Lax-Friedrichs (LLF) and Harten-Lax-van Leer (HLL) are common choices. In Appendix B, we describe a few examples of Riemann solvers for Eqns. (2.1). The two right-hand integrals are evaluated numerically using Gaussian quadrature. As has been discussed in Refs. [8, 11], the volume integral present in Eqn. (3.4) should be evaluated with a quadrature rule that is exact for polynomials of order $2P$, and the surface integral should be evaluated with a quadrature rule that is exact for polynomials of order $2P+1$. For Gaussian quadrature, this corresponds to a quadrature rule using at least $N_q = (P+1)^d$ points for volume integrals and $N_q = (P+1)^{d-1}$ points for surface integrals, where d is the number of spatial dimensions of the element.

Inserting the definition for $\mathbf{q}_e$, Eqn. (3.1), we obtain,

$$M_{ij}^e \frac{d}{dt} \widehat{\mathbf{q}}_j^e d\Omega + \int_{\partial\Omega_e} \phi_i^e \widehat{\vec{\mathbf{f}}} \cdot \vec{n} ds - \int_{\Omega_e} \vec{\mathbf{f}}(\mathbf{q}_e) \cdot \nabla \phi_i^e d\Omega = 0, \tag{3.5}$$

where M_{ij}^e is an entry of the elemental mass matrix,

$$M_{ij}^e = \int_{\Omega_e} \phi_i^e \phi_j^e d\Omega, \tag{3.6}$$

which in practice is also evaluated exactly using a sufficient quadrature rule. Now the solution degrees of freedom $\widehat{\mathbf{q}}_j^e$ may be evolved by an explicit time-stepping scheme such as the family of Runge-Kutta schemes [4].

In Sections 3.2-3.4, we describe the discontinuous Galerkin discretizations studied herein for the nonconservative subsystem of Eqns. (2.1), i.e., Eqns. (2.1a) and (2.1d).

3.2. Pandare Discretization for Nonconservative Equations

We now describe the discretization of the nonconservative subsystem of the six-equation model, Eqns. (2.1), using the approach of Pandare et al. [26, 27]. This approach uses the weak form, for Eqn. (2.1a),

$$\int_{\Omega_e} \phi_i^e \frac{\partial}{\partial t} \alpha_k d\Omega + \int_{\partial\Omega_e} \phi_i^e \widehat{(\alpha_k \vec{u})} \cdot \vec{n} ds - \int_{\Omega_e} \alpha_k \nabla \cdot (\vec{u} \phi_i^e) d\Omega = 0, \tag{3.7}$$

where $\widehat{\alpha_k \vec{u}}$ is the numerical flux term from Eqn. (3.4). Here, the divergence of the velocity $\vec{u}$ is to be calculated in a special manner, rather than from the gradients of the DG solution. The authors instead define,

$$\nabla \cdot \vec{u} = \int_{\partial\Omega_e} \vec{u^*} \cdot \vec{n} ds, \tag{3.8}$$

where the velocity $\vec{u}^*$ is taken from the Riemann solver in such a manner that, according to the authors, the discretization is *well-balanced*. This means, generally, that the nonconservative discretization does not cause the accumulation of quantities that should be uniform. In the case of multimaterial hydrodynamics, it means that equilibria of primitive quantities such as velocity and pressure remain uniform in scenarios where the governing equations require so. This concept will be revisited in Section 3.5. The weak form for Eqn. (2.1d) is,

$$\int_{\Omega_e} \phi_i^e \frac{\partial}{\partial t}(\alpha_k \rho_k E_k) d\Omega + \int_{\partial\Omega_e} \phi_i^e [\vec{u}(\widehat{\alpha_k \rho_k E_k + \alpha_k p_k})] \cdot \vec{n} ds - \int_{\Omega_e} \vec{u}(\alpha_k \rho_k E_k + \alpha_k p_k) \cdot \nabla \phi_i^e d\Omega$$
$$- \int_{\Omega_e} \phi_i^e \vec{u} \cdot \nabla(\alpha_k p_k) d\Omega + \int_{\Omega_e} \phi_i^e z_k \vec{u} \cdot \nabla p d\Omega = 0, \tag{3.9}$$

where $[\vec{u}(\widehat{\alpha_k \rho_k E_k + \alpha_k p_k})]$ is the numerical flux term from Eqn. (3.4). Here, the gradient of the partial pressure $\nabla(\alpha_k p_k)$ is to be calculated in a special manner, rather than from the gradients of DG solution. The authors define,

$$\nabla(\alpha_k p_k) = \int_{\partial\Omega_e} (\alpha_k p_k)^* \vec{n} ds, \tag{3.10}$$

where the partial pressure $(\alpha_k p_k)^*$ is taken from the Riemann solver in such a manner that, according to the authors, the discretization is *well-balanced*. The quantity ∇p is calculated from the sum of the quantities $\nabla(\alpha_k p_k)$.

We implemented this approach in the FLEXO code: none of the results in Chapter 7 were obtained using the QUINOA code [23].

3.3. Path-Conservative Discretization for Nonconservative Equations

We now describe the discretization of the nonconservative subsystem of the six-equation model, Eqns. (2.1), using the path-conservative approach for nonconservative equations [6, 12]. At the time of this writing, the present authors are unaware of other work in the literature that has applied the path-conservative discretization to the six-equation model.

The path-conservative approach for discretizing a general nonconservative system of equations, which can be written as,

$$\frac{\partial}{\partial t}\mathbf{q} + \nabla \cdot \vec{\mathbf{f}}(\mathbf{q}) + \vec{\mathbf{h}}(\mathbf{q}) \cdot \nabla \mathbf{q} = 0, \tag{3.11}$$

has been applied to solve nonconservative equations using the discontinuous Galerkin method [18, 31, 51]. In this context, the weak form is given by,

$$\int_{\Omega_e} \phi_i^e \frac{\partial}{\partial t}\mathbf{q}_e d\Omega + \int_{\partial\Omega_e} \phi_i^e \widehat{\vec{\mathbf{f}}} \cdot \vec{n} d\Omega - \int_{\Omega_e} \vec{\mathbf{f}}(\mathbf{q}_e) \cdot \nabla\phi_i^e dx \\ - \int_{\partial\Omega_e} \{\phi_i\}(\vec{\mathbf{h}}\mathbf{q})^* \cdot \vec{n} ds + \int_{\Omega_e} \phi_i^e \vec{\mathbf{h}}(\mathbf{q}_e) \cdot \nabla\mathbf{q}_e d\Omega = 0. \quad (3.12)$$

Here, $\{\phi_i\} = \frac{1}{2}(\phi_i^- + \phi_i^+)$ denotes the average of a quantity across the element interface $\partial\Omega_e$, where ϕ_i^- denotes the value on the interface taken from Ω_e, and ϕ_i^+ denotes the value on the interface taken from the neighboring element sharing the element interface $\partial\Omega_e$. This notation is borrowed from continuous Galerkin literature; for the discontinuous Galerkin method, the basis function ϕ_i^+ of the neighboring element as seen from element Ω_e is zero, such that $\{\phi_i\} = \frac{1}{2}\phi_i^-$. The quantity $\widehat{\vec{\mathbf{f}}}$ is the conservative numerical flux from Eqn. (3.4). Note, however, that the nonconservative terms alter the jump conditions using this approach, so that care must be taken in re-formulating the numerical flux function [14]. The path-conservative term $(\vec{\mathbf{h}}\mathbf{q})^*$ is evaluated as,

$$(\vec{\mathbf{h}}\mathbf{q})^* = \int_0^1 \vec{\mathbf{h}}(\psi(\tau;\mathbf{q}^-,\mathbf{q}^+))\frac{\partial\psi}{\partial\tau}(\tau;\mathbf{q}^-,\mathbf{q}^+)d\tau, \quad (3.13)$$

where we assume a linear path joins the states across the interface, $\psi(\tau;\mathbf{q}^-,\mathbf{q}^+) = \mathbf{q}^- + \tau(\mathbf{q}^+ - \mathbf{q}^-)$.

Considering the form of the path-conservative term Eqn. (3.13), we realize that writing the path $\psi(\tau;\mathbf{q}^-,\mathbf{q}^+)$ directly in terms of the state variables $\mathbf{q} = [\alpha_k, \alpha_k\rho_k, \rho u, \alpha_k\rho_k E_k]$ introduces non-linearity in the quantity $\vec{\mathbf{h}}(\psi)$. Forming the path-conservative term $(\vec{h}q)^*$ for Eqn. (2.1a) in this manner,

$$(\vec{u}\alpha_k)^* = \int_0^1 \frac{\rho\vec{u}^- + \tau(\rho\vec{u}^+ - \rho\vec{u}^-)}{\rho^- + \tau(\rho^+ - \rho^-)}(\alpha_k^+ - \alpha_k^-)d\tau. \quad (3.14)$$

Here we can move the quantity $[[\alpha_k]] = (\alpha_k^+ - \alpha_k^-)$ out of the integral, but what remains cannot be solved analytically and must be solved by quadrature. This is not at all desirable, as we must solve an integral of this type at each element interface during every sub-step of our RKDG scheme. Note that forming the $\frac{\partial\psi}{\partial\tau}$ can also cause this issue, if writing the $\nabla\mathbf{q}$ in the non-conservative term directly in terms of the state vector $\mathbf{q}$ introduces products/quotients of the state variables.

Instead, we can circumvent this issue by ensuring that the non-conservative term is written via a mapping of $\vec{\mathbf{h}}(\mathbf{q})$ in terms of primitive variables that allows these terms to appear linearly in the path-conservative term. Using this approach, the path-conservative term $(\vec{h}q)^*$ for Eqn. (2.1a) evaluates as:

$$(\vec{u}\alpha_k)^* = \int_0^1 [\vec{u}^- + \tau(\vec{u}^+ - \vec{u}^-)][\alpha_k^+ - \alpha_k^-]d\tau = \{\vec{u}\}[[\alpha_k]], \quad (3.15)$$

which requires no quadrature. Similarly, for Eqn. (2.1d), we apply this approach term-by-term:

$$(\vec{u}z_k p)^* = \int_0^1 [(\vec{u}z_k)^- + \tau((\vec{u}z_k)^+ - (\vec{u}z_k)^-)][p^+ - p^-]d\tau = \{\vec{u}z_k\}[[p]], \quad (3.16)$$

$$(\vec{u}\alpha_k p_k)^* = \int_0^1 [\vec{u}^- + \tau(\vec{u}^+ - \vec{u}^-)][(\alpha_k p_k)^+ - (\alpha_k p_k)^-]d\tau = \{\vec{u}\}[[\alpha_k p_k]]. \quad (3.17)$$

Inserting the nonconservative surface terms Eqn. (3.15), Eqn. (3.16), and Eqn. 3.17 into Eqn. (3.12), we obtain for Eqn. (2.1a),

$$\int_{\Omega_e} \phi_i^e \frac{\partial}{\partial t} \alpha_k d\Omega - \int_{\partial\Omega_e} \frac{1}{2} \phi_i^e \{\vec{u}\} [[\alpha_k]] \cdot \vec{n} ds + \int_{\Omega_e} \phi_i^e \vec{u} \cdot \nabla \alpha_k d\Omega = 0, \tag{3.18}$$

and for Eqn. (2.1d):

$$\begin{aligned} \int_{\Omega_e} \phi_i^e \frac{\partial}{\partial t} (\alpha_k \rho_k E_k) \, d\Omega + \int_{\partial\Omega_e} \phi_i^e \vec{u} \widehat{(\alpha_k \rho_k E_k + \alpha_k p_k)} \cdot \vec{n} ds \\ - \int_{\Omega_e} \vec{u} (\alpha_k \rho_k E_k + \alpha_k p_k) \cdot \nabla \phi_i^e d\Omega \\ - \int_{\partial\Omega_e} \frac{1}{2} \phi_i^e \{\vec{u} z_k\} [[p]] \cdot \vec{n} ds + \int_{\Omega_e} \phi_i^e \vec{u} z_k \cdot \nabla p d\Omega \\ + \int_{\partial\Omega_e} \frac{1}{2} \phi_i^e \{\vec{u}\} [[\alpha_k p_k]] \cdot \vec{n} ds - \int_{\Omega_e} \phi_i^e \vec{u} \cdot \nabla \alpha_k p_k d\Omega = 0, \end{aligned} \tag{3.19}$$

where $[\vec{u} \widehat{(\alpha_k \rho_k E_k + \alpha_k p_k)}]$ is the numerical flux term from Eqn. (3.4).

We note that other authors [46] have discretized the volume fraction equation Eqn. (3.18) in a different form using the path-conservative approach (in the context of a five-equation model) and found that it violates *consistency of reduction*, meaning that it does not enforce constancy of volume fraction in a region of constant phase when a velocity gradient is present. By directly discretizing the nonconservative form of Eqn. (3.18), we circumvent this issue.

Furthermore, it has been shown [1] that the path-conservative discretization of nonconservative systems of equations may not converge to the correct solution even if the path is chosen such that the jump conditions are correctly represented. This is a known shortcoming of the path-conservative approach, and is outside the scope of this work.

3.4. Spatial-Averaging Discretization for Nonconservative Equations

We now describe the discretization of the nonconservative subsystem of the six-equation model, Eqns. (2.1), using a more recent approach [46, 50], which has not been extended to this model prior to the current report. We term this the *spatial-averaging* approach to discretization of nonconservative equations.

We begin with our proposed discretization for the volume fraction equation, Eqn. (2.1a). Evaluating the weak form of the equations, written in the form $\partial_t \alpha_k + \nabla \cdot [\alpha_k \vec{u}] - \alpha_k \nabla \cdot \vec{u} = 0$,

$$\int_{\Omega_e} \phi_i^e \frac{\partial}{\partial t} \alpha_k d\Omega + \int_{\partial\Omega_e} \phi_i^e \widehat{\alpha_k \vec{u}} \cdot \vec{n} ds - \int_{\Omega_e} \alpha_k \vec{u} \cdot \nabla \phi_i^e d\Omega - \int_{\Omega_e} \phi_i^e \alpha_k \nabla \cdot \vec{u} d\Omega = 0, \tag{3.20}$$

where $\widehat{\alpha_k \vec{u}}$ is the numerical flux term from Eqn. (3.4).

In order to remove the α_k from the last integral to apply the divergence theorem, we make the approximation that $\alpha_k \approx \overline{\alpha}_k = \frac{1}{|\Omega_e|}\int_{\Omega_e} \alpha_k d\Omega$,

$$\int_{\Omega_e} \phi_i^e \frac{\partial}{\partial t}\alpha_k d\Omega + \int_{\partial\Omega_e} \phi_i^e \widehat{\alpha_k \vec{u}} \cdot \vec{n} ds - \int_{\Omega_e} \alpha_k \vec{u} \cdot \nabla \phi_i^e d\Omega - \overline{\alpha}_k \int_{\Omega_e} \phi_i^e \nabla \cdot \vec{u} d\Omega = 0. \tag{3.21}$$

Rearranging,

$$\int_{\Omega_e} \phi_i^e \frac{\partial}{\partial t}\alpha_k d\Omega + \int_{\partial\Omega_e} \phi_i^e \widehat{\alpha_k \vec{u}} \cdot \vec{n} ds - \int_{\Omega_e} \alpha_k \vec{u} \cdot \nabla \phi_i^e d\Omega - \overline{\alpha}_k \int_{\partial\Omega_e} \phi_i^e \widehat{\vec{u}} \cdot \vec{n} ds + \overline{\alpha}_k \int_{\Omega_e} \vec{u} \cdot \nabla \phi_i^e d\Omega = 0, \tag{3.22}$$

where the nonconservative flux $\widehat{\vec{u}}$ is consistent with the discretization of $\nabla \cdot [\alpha_k \vec{u}]$ in the conservative surface integral term. In Appendix B, we describe a few examples of Riemann solvers and corresponding nonconservative terms. We thus arrive at our weak form for the volume fraction equation,

$$\int_{\Omega_e} \phi_i^e \frac{\partial}{\partial t}\alpha_k d\Omega + \int_{\partial\Omega_e} \phi_i^e (\widehat{\alpha_k \vec{u}} - \overline{\alpha}_k \widehat{\vec{u}}) \cdot \vec{n} ds - \int_{\Omega_e} (\alpha_k - \overline{\alpha}_k) \vec{u} \cdot \nabla \phi_i^e d\Omega = 0. \tag{3.23}$$

We also introduce a similar discretization for the energy equation, Eqn. (2.1d). Evaluating the weak form of the energy equation,

$$\int_{\Omega_e} \phi_i^e \frac{\partial}{\partial t}(\alpha_k \rho_k E_k) d\Omega + \int_{\partial\Omega_e} \phi_i^e \left[\vec{u}(\widehat{\alpha_k \rho_k E_k + \alpha_k p_k})\right] \cdot \vec{n} ds - \int_{\Omega_e} \left[\alpha_k \rho_k E_k + \alpha_k p_k\right] \vec{u} \cdot \nabla \phi_i^e d\Omega + \int_{\Omega_e} \phi_i^e \vec{u} \cdot (z_k \nabla p - \nabla \alpha_k p_k) d\Omega = 0, \tag{3.24}$$

where $[\vec{u}(\widehat{\alpha_k \rho_k E_k + \alpha_k p_k})]$ is the numerical flux term from Eqn. (3.4).

We use an average velocity $\overline{\vec{u}} = \frac{1}{|\Omega_e|}\int_{\Omega_e} \vec{u} d\Omega$ and the average of the product of velocity and mass fraction $\overline{z_k \vec{u}} = \frac{1}{|\Omega_e|}\int_{\Omega_e} z_k \vec{u} d\Omega$ to remove these quantities from the integrals,

$$\int_{\Omega_e} \phi_i^e \frac{\partial}{\partial t}(\alpha_k \rho_k E_k) d\Omega + \int_{\partial\Omega_e} \phi_i^e \left[\vec{u}(\widehat{\alpha_k \rho_k E_k + \alpha_k p_k})\right] \cdot \vec{n} ds - \int_{\Omega_e} \left[\alpha_k \rho_k E_k + \alpha_k p_k\right] \vec{u} \cdot \nabla \phi_i^e d\Omega + \overline{z_k \vec{u}} \cdot \int_{\Omega_e} \phi_i^e \nabla p d\Omega - \overline{\vec{u}} \cdot \int_{\Omega_e} \phi_i^e \nabla \alpha_k p_k d\Omega = 0. \tag{3.25}$$

Now, we may apply the divergence theorem to the last two terms,

$$\int_{\Omega_e} \phi_i^e \frac{\partial}{\partial t}(\alpha_k \rho_k E_k) d\Omega + \int_{\partial\Omega_e} \phi_i^e \left[\vec{u}(\widehat{\alpha_k \rho_k E_k + \alpha_k p_k})\right] \cdot \vec{n} ds - \int_{\Omega_e} \left[\alpha_k \rho_k E_k + \alpha_k p_k\right] \vec{u} \cdot \nabla \phi_i^e d\Omega + \overline{z_k \vec{u}} \cdot \int_{\partial\Omega_e} \phi_i^e \hat{p} \vec{n} ds - \overline{z_k \vec{u}} \cdot \int_{\Omega_e} p \nabla \phi_i^e d\Omega - \overline{\vec{u}} \cdot \int_{\partial\Omega_e} \phi_i^e \widehat{\alpha_k p_k} \vec{n} ds + \overline{\vec{u}} \cdot \int_{\Omega_e} \alpha_k p_k \nabla \phi_i^e d\Omega = 0, \tag{3.26}$$

where $\widehat{\alpha_k p_k}$ is consistent with the discretization of $\nabla[\alpha_k p_k]$ in the conservative surface integral term and $\hat{p}$ is calculated from the sum of these partial pressures. In Appendix B, we describe a few

examples of Riemann solvers and corresponding nonconservative terms. We obtain the weak form for the energy equation,

$$\int_{\Omega_e} \phi_i^e \frac{\partial}{\partial t}(\alpha_k \rho_k E_k) d\Omega + \int_{\partial\Omega_e} \phi_i^e [\vec{u}(\alpha_k \widehat{\rho_k E_k + \alpha_k p_k}) + \overline{z_k \vec{u}}\widehat{p} - \overline{\vec{u}}\widehat{\alpha_k p_k}] \cdot \vec{n} ds$$
$$- \int_{\Omega_e} [\vec{u}(\alpha_k \rho_k E_k + \alpha_k p_k) + \overline{z_k \vec{u}} p - \overline{\vec{u}} \alpha_k p_k] \cdot \nabla \phi_i^e d\Omega = 0. \quad (3.27)$$

3.5. Well-Balancedness of Nonconservative Discretizations

The concept of *well-balancedness* of a numerical method refers to its ability to maintain some physically relevant state of equilibrium when appropriate. A well-balanced method, in the case of Eqns. (2.1), should preserve velocity, phasic pressure, and phasic density equilibria for isolated interfaces. The interface may be represented by sharp or smooth variations of α_k, (the prior case requiring some means of capturing the discontinuity, such as solution limiting) but should not disturb other variables that are meant to remain constant and uniform.

First, we consider how the continuum equations behave in the case of two ideal gases separated by an isolated one-dimensional interface (across which pressures, but not the bulk density, are uniform) moving at a uniform velocity of u. We consider a diffused (i.e., smooth) interface, such that spatial derivatives are well-defined. In this case, the bulk pressure p is initially uniform as are the material pressures p_k and densities ρ_k. For an ideal gas, $\rho_k e_k = \frac{p_k}{\gamma_k - 1}$, where γ_k is the ratio of specific heats for material k. Neglecting the pressure relaxation source term, the volume fraction equations are:

$$\frac{\partial}{\partial t}\alpha_k + u \frac{\partial}{\partial x}\alpha_k = 0, \quad (3.28)$$

for $k = 1, 2$. The density equations simplify to:

$$\frac{\partial}{\partial t}[\alpha_k \rho_k] + \rho_k u \frac{\partial}{\partial x}\alpha_k = 0. \quad (3.29)$$

Which can be combined with Eqn. (3.28) to show,

$$\frac{\partial}{\partial t}\rho_k = 0. \quad (3.30)$$

The momentum equation becomes:

$$\rho \frac{\partial}{\partial t} u = 0, \quad (3.31)$$

indicating that the velocity remains uniform. The energy equations are,

$$\frac{\partial}{\partial t}[\alpha_k \rho_k E_k] + \frac{\partial}{\partial x}[u(\alpha_k \rho_k E_k + \alpha_k p_k)] + u[z_k \frac{\partial}{\partial x} p - \frac{\partial}{\partial x}\alpha_k p_k] = 0. \quad (3.32)$$

Using the definition of $\rho_k \varepsilon_k = \frac{p_k}{\gamma_k - 1}$ for an ideal gas and the conditions for an isolated interface, the energy equations become:

$$\frac{\partial}{\partial t}[\alpha_k \frac{p_k}{\gamma_k - 1}] + \frac{p_k}{\gamma_k - 1} u \frac{\partial}{\partial x}\alpha_k - p_k u \frac{\partial}{\partial x}\alpha_k + \frac{1}{2}u^2 \rho_k \frac{\partial}{\partial t}\alpha_k + \frac{1}{2}u^2 \rho_k u \frac{\partial}{\partial x}\alpha_k + p_k u \frac{\partial}{\partial x}\alpha_k = 0. \quad (3.33)$$

The kinetic energy terms are zero by Eqn. (3.28), and we are left with:

$$\frac{\partial}{\partial t}[\alpha_k \frac{p_k}{\gamma_k - 1}] + \frac{p_k}{\gamma_k - 1} u \frac{\partial}{\partial x}\alpha_k = 0. \quad (3.34)$$

Rearranging, and using Eqn. (3.28), we show that,

$$\frac{\partial}{\partial t} p_k = 0. \quad (3.35)$$

Thus, the material pressures should remain uniform and pressure equilibration/relaxation mechanisms are unnecessary in this case. It is also relatively straightforward to prove that $\frac{\partial}{\partial t} p = 0$. A discretization that respects the equilibria stated by Eqns. (3.30), (3.31), and (3.35) is said to be well-balanced. A similar analysis of the governing equations in the case of a discontinuous material interface results in identical equilibrium conditions.

In the following sections, we analyze the well-balancedness of the discretizations described in Sections 3.2-3.4 in the case of an advecting 1-D interface. In these analyses, the numerical flux function introduced in Eqn. (3.4) is assumed to be chosen as the Local Lax-Friedrichs flux (see Section B.1), without loss of generality.

3.5.1. Analysis of the Pandare Discretization

We will now examine the properties of the Pandare discretization of Section 3.2 in the case of a 1-D isolated interface.

In 1-D, the weak form of the volume fraction equation becomes,

$$\int_{\Omega_e} \phi_i^e \frac{\partial}{\partial t}\alpha_k d\Omega + \int_{\partial\Omega_e} \phi_i^e (\widehat{\alpha_k u}) n ds - \int_{\Omega_e} \alpha_k \frac{\partial}{\partial x}(u\phi_i^e) d\Omega = 0. \quad (3.36)$$

In the case of an isolated interface,

$$\int_{\Omega_e} \phi_i^e \frac{\partial}{\partial t}\alpha_k d\Omega + \int_{\partial\Omega_e} \phi_i^e (\widehat{\alpha_k u}) n ds - u \int_{\Omega_e} \alpha_k \frac{\partial}{\partial x}\phi_i^e d\Omega = 0. \quad (3.37)$$

Here, the numerical flux $\widehat{\alpha_k u}$ contains a stabilization term, so we do not remove u from the flux as it may not be factored from the stabilization term. In the case of pure flow, where α_k is uniform (even in the presence of a velocity gradient), so long as the discretization of $\widehat{u}$ is consistent with the appearance of u in the numerical flux $\widehat{\alpha_k u}$, the volume fraction will remain uniform.

In 1-D, the weak form of the density equation becomes,

$$\int_{\Omega_e} \phi_i^e \frac{\partial}{\partial t}(\alpha_k \rho_k) d\Omega + \int_{\partial\Omega_e} \phi_i^e (\widehat{\alpha_k \rho_k u}) n ds - \int_{\Omega_e} (\alpha_k \rho_k u) \frac{\partial}{\partial x} \phi_i^e d\Omega = 0. \tag{3.38}$$

In the case of an isolated interface,

$$\int_{\Omega_e} \phi_i^e \frac{\partial}{\partial t}(\alpha_k \rho_k) d\Omega + \rho_k \int_{\partial\Omega_e} \phi_i^e (\widehat{\alpha_k u}) n ds - u\rho_k \int_{\Omega_e} \alpha_k \frac{\partial}{\partial x} \phi_i^e d\Omega = 0. \tag{3.39}$$

We may factor out the uniform ρ_k from the numerical flux $\widehat{\alpha_k \rho_k u}$ because it appears in the variable $\alpha_k \rho_k$, not just in the flux $\alpha_k \rho_k u$. Because it appears only in the flux and may not be factored out of the stabilization term, we do not factor out u from $\widehat{\alpha_k \rho_k u}$. We notice that the final two terms of Eqn. (3.39) is ρ_k times the right-hand side of Eqn. (3.37), such that Eqn. (3.39) becomes:

$$\int_{\Omega_e} \phi_i^e \frac{\partial}{\partial t} \rho_k d\Omega = 0. \tag{3.40}$$

In 1-D, the weak form of the momentum equation becomes,

$$\int_{\Omega_e} \phi_i^e \frac{\partial}{\partial t}(\rho u) d\Omega + \int_{\partial\Omega_e} \phi_i^e (\widehat{\rho u^2 + p}) n ds - \int_{\Omega_e} (\rho u^2 + p) \frac{\partial}{\partial x} \phi_i^e d\Omega = 0. \tag{3.41}$$

For an isolated interface, this becomes,

$$\int_{\Omega_e} \phi_i^e \frac{\partial}{\partial t}(\rho u) d\Omega + \int_{\partial\Omega_e} \phi_i^e (\widehat{\rho u^2}) n ds - u^2 \int_{\Omega_e} \rho \frac{\partial}{\partial x} \phi_i^e d\Omega = 0, \tag{3.42}$$

where we have broken up $\widehat{\rho u^2 + p}$ to $\widehat{\rho u^2} + p$ because the pressure appears only in the flux and will not appear in the stabilization term, so the stabilization term remains with the flux $\widehat{\rho u^2}$. As the bulk pressure is uniform initially, the surface and volume integral terms including it cancel by the divergence theorem. Likewise, we factor out only one u to respect that the variable ρu will appear in the stabilization term.

Inserting the definition $\rho = \alpha_1 \rho_1 + \alpha_2 \rho_2$, we can further write $\widehat{(\alpha_1 \rho_1 + \alpha_2 \rho_2) u}$ as $\widehat{\alpha_1 \rho_1 u} + \widehat{\alpha_2 \rho_2 u}$, where the stabilization term is also split up among the two material momentum contributions accordingly. Because the two contributions are linearly additive in both the flux ρu^2 and the variable ρu, this can be done consistently, and we obtain

$$\begin{aligned} \rho \int_{\Omega_e} \phi_i^e \frac{\partial}{\partial t} u d\Omega + u \int_{\Omega_e} \phi_i^e \frac{\partial}{\partial t}(\alpha_1 \rho_1) d\Omega + u \int_{\Omega_e} \phi_i^e \frac{\partial}{\partial t}(\alpha_2 \rho_2) d\Omega \\ + u \int_{\partial\Omega_e} \phi_i^e \widehat{\alpha_1 \rho_1 u} n ds + u \int_{\partial\Omega_e} \phi_i^e \widehat{\alpha_2 \rho_2 u} n ds \\ - u^2 \int_{\Omega_e} \alpha_1 \rho_1 \frac{\partial}{\partial x} \phi_i^e d\Omega - u^2 \int_{\Omega_e} \alpha_2 \rho_2 \frac{\partial}{\partial x} \phi_i^e d\Omega = 0. \end{aligned} \tag{3.43}$$

All but the first term can be identified as u times Eqn. (3.39) and set to zero, leaving us with:

$$\int_{\Omega_e} \phi_i^e \frac{\partial}{\partial t} u d\Omega = 0. \tag{3.44}$$

In 1-D, the weak form for the energy equation can be written,

$$\int_{\Omega_e} \phi_i^e \frac{\partial}{\partial t}(\alpha_k \rho_k E_k) d\Omega + \int_{\partial\Omega_e} \phi_i^e [u(\widehat{\alpha_k \rho_k E_k + \alpha_k p_k})] nds - \int_{\Omega_e} u(\alpha_k \rho_k E_k + \alpha_k p_k) \frac{\partial}{\partial x} \phi_i^e d\Omega$$
$$- \int_{\Omega_e} \phi_i^e u \frac{\partial}{\partial x}(\alpha_k p_k) d\Omega + \int_{\Omega_e} \phi_i^e z_k u \frac{\partial}{\partial x} p d\Omega = 0. \quad (3.45)$$

For an ideal gas,

$$\int_{\Omega_e} \phi_i^e \frac{\partial}{\partial t}(\alpha_k \frac{p_k}{\gamma_k - 1}) d\Omega + \int_{\Omega_e} \phi_i^e \frac{\partial}{\partial t}(\frac{1}{2}\alpha_k \rho_k u^2) d\Omega$$
$$+ \int_{\partial\Omega_e} \phi_i^e [u(\widehat{\alpha_k \frac{p_k}{\gamma_k - 1} + \frac{1}{2}\alpha_k \rho_k u^2 + \alpha_k p_k})] nds$$
$$- \int_{\Omega_e} u(\alpha_k \frac{p_k}{\gamma_k - 1} + \frac{1}{2}\alpha_k \rho_k u^2 + \alpha_k p_k) \frac{\partial}{\partial x} \phi_i^e d\Omega$$
$$- \int_{\Omega_e} \phi_i^e u \frac{\partial}{\partial x}(\alpha_k p_k) d\Omega + \int_{\Omega_e} \phi_i^e z_k u \frac{\partial}{\partial x} p d\Omega = 0. \quad (3.46)$$

We may separate the numerical flux $u(\alpha_k \frac{p_k}{\gamma_k - 1} + \widehat{\frac{1}{2}\alpha_k \rho_k} u^2 + \alpha_k p_k)$ into $u(\alpha_k \widehat{\frac{p_k}{\gamma_k - 1} + \frac{1}{2}\alpha_k \rho_k u^2}) + \widehat{u\alpha_k p_k}$, where the term $\widehat{u\alpha_k p_k}$ does not contain a stabilization term, as it appears only in the flux. Then we can further write $u(\alpha_k \widehat{\frac{p_k}{\gamma_k - 1} + \frac{1}{2}\alpha_k \rho_k u^2})$ as $\widehat{u\alpha_k \frac{p_k}{\gamma_k - 1}} + \widehat{\frac{1}{2}\alpha_k \rho_k u^3}$, where the stabilization term is also split up among the internal energy and kinetic energy contributions accordingly. Because the internal energy and kinetic energy contributions are linearly additive in both the flux $u\alpha_k \rho_k E_k$ and the variable $\alpha_k \rho_k E_k$, this can be done consistently. We obtain,

$$\int_{\Omega_e} \phi_i^e \frac{\partial}{\partial t}(\alpha_k \frac{p_k}{\gamma_k - 1}) d\Omega + \int_{\Omega_e} \phi_i^e \frac{\partial}{\partial t}(\frac{1}{2}\alpha_k \rho_k u^2) d\Omega$$
$$+ \int_{\partial\Omega_e} \phi_i^e u \widehat{\alpha_k \frac{p_k}{\gamma_k - 1}} nds + \int_{\partial\Omega_e} \phi_i^e \widehat{\frac{1}{2}\alpha_k \rho_k u^3} nds + \int_{\partial\Omega_e} \phi_i^e \widehat{u\alpha_k p_k} nds$$
$$- \int_{\Omega_e} [u(\alpha_k \frac{p_k}{\gamma_k - 1} + \frac{1}{2}\alpha_k \rho_k u^2 + \alpha_k p_k)] \frac{\partial}{\partial x} \phi_i^e d\Omega$$
$$- \int_{\Omega_e} \phi_i^e u \frac{\partial}{\partial x}(\alpha_k p_k) d\Omega + \int_{\Omega_e} \phi_i^e z_k u \frac{\partial}{\partial x} p d\Omega = 0. \quad (3.47)$$

For the isolated interface,

$$\int_{\Omega_e} \phi_i^e \frac{\partial}{\partial t}(\alpha_k \frac{p_k}{\gamma_k - 1}) d\Omega + \frac{p_k}{\gamma_k - 1} \int_{\partial\Omega_e} \phi_i^e (\widehat{u\alpha_k}) nds - u \frac{p_k}{\gamma_k - 1} \int_{\Omega_e} \alpha_k \frac{\partial}{\partial x} \phi_i^e d\Omega$$
$$+ \frac{1}{2}\rho_k u^2 \int_{\Omega_e} \phi_i^e \frac{\partial}{\partial t} \alpha_k d\Omega + \frac{1}{2}\rho_k u^2 \int_{\partial\Omega_e} \phi_i^e (\widehat{u\alpha_k}) nds - \frac{1}{2}\rho_k u^3 \int_{\Omega_e} \alpha_k \frac{\partial}{\partial x} \phi_i^e d\Omega$$
$$+ u \int_{\partial\Omega_e} \phi_i^e (\widehat{\alpha_k p_k}) nds - u \int_{\Omega_e} \alpha_k p_k \frac{\partial}{\partial x} \phi_i^e d\Omega$$
$$- u \int_{\Omega_e} \phi_i^e \frac{\partial}{\partial x}(\alpha_k p_k) d\Omega = 0. \quad (3.48)$$

We eliminate the kinetic energy terms using Eqn. (3.37),

$$\int_{\Omega_e} \phi_i^e \frac{\partial}{\partial t}(\alpha_k \frac{p_k}{\gamma_k - 1}) d\Omega + \frac{p_k}{\gamma_k - 1} \int_{\partial\Omega_e} \phi_i^e (\widehat{u\alpha_k}) n ds - u \frac{p_k}{\gamma_k - 1} \int_{\Omega_e} \alpha_k \frac{\partial}{\partial x} \phi_i^e d\Omega + u \int_{\partial\Omega_e} \phi_i^e (\widehat{\alpha_k p_k}) n ds - u \int_{\Omega_e} \alpha_k p_k \frac{\partial}{\partial x} \phi_i^e d\Omega - u \int_{\Omega_e} \phi_i^e \frac{\partial}{\partial x}(\alpha_k p_k) d\Omega = 0. \quad (3.49)$$

If the $\frac{\partial}{\partial x}\alpha_k\rho_k$ in the final volume integral above were indeed the derivative of the DG solution $\alpha_k\rho_k$, we would be able to combine the volume integrals containing $\alpha_k p_k$, and apply the divergence theorem to obtain:

$$\int_{\Omega_e} \phi_i^e \frac{\partial}{\partial t}(\alpha_k \frac{p_k}{\gamma_k - 1}) d\Omega + \frac{p_k}{\gamma_k - 1} \int_{\partial\Omega_e} \phi_i^e (\widehat{u\alpha_k}) n ds - u \frac{p_k}{\gamma_k - 1} \int_{\Omega_e} \alpha_k \frac{\partial}{\partial x} \phi_i^e d\Omega + u \int_{\partial\Omega_e} \phi_i^e [\widehat{\alpha_k p_k} - (\alpha_k p_k)^*)] n ds = 0. \quad (3.50)$$

At this point, given that the discretization for $(\alpha_k p_k)^*$ is constructed in such a way as to be identical to $\widehat{\alpha_k p_k}$, we would be able to use Eqn. (3.37) to recover:

$$\int_{\Omega_e} \phi_i^e \frac{\partial}{\partial t} p_k d\Omega = 0, \quad (3.51)$$

such that the uniformity of the material pressure p_k would be maintained. However, the Pandare discretization approximates the derivative $\frac{\partial}{\partial x}\alpha_k\rho_k$ using Eqn. (3.10), so Eqn. (3.50) onward does not apply, and we cannot ensure that $\int_{\Omega_e} \phi_i^e \frac{\partial}{\partial t} p_k d\Omega = 0$ and we cannot ensure that the material pressure remains uniform.

In Reference [26], numerical results are shown depicting this discretization to be well-balanced for the case of an isolated advecting interface. It should be noted that these results show numerical results indicating that the discretization is well-balanced in terms of the bulk pressure p. While this is possible with material pressures p_k that are not themselves well-balanced, our perspective, based on the analysis of Section 3.5, is that this is a necessary but not sufficient condition for a truly well-balanced discretization of this type.

3.5.2. Analysis of the Path-Conservative Discretization

We will now examine the properties of the path-conservative discretization of Section 3.3 in the case of an isolated interface.

In 1-D, the weak form of the volume fraction equation becomes,

$$\int_{\Omega_e} \phi_i^e \frac{\partial}{\partial t} \alpha_k d\Omega - \int_{\partial\Omega_e} \frac{1}{2} \phi_i^e \{u\} [[\alpha_k]] n ds + \int_{\Omega_e} \phi_i^e u \frac{\partial}{\partial x} \alpha_k d\Omega = 0. \quad (3.52)$$

We note that, in the case of pure flow, where α_k is uniform, even in the presence of a velocity gradient, the volume fraction will remain uniform.

In the case of an isolated interface,

$$\int_{\Omega_e} \phi_i^e \frac{\partial}{\partial t}\alpha_k d\Omega - u\int_{\partial\Omega_e} \frac{1}{2}\phi_i^e [[\alpha_k]] nds + u\int_{\Omega_e} \phi_i^e \frac{\partial}{\partial x}\alpha_k d\Omega = 0. \tag{3.53}$$

We apply the divergence theorem to the last integral to obtain,

$$\int_{\Omega_e} \phi_i^e \frac{\partial}{\partial t}\alpha_k d\Omega + u\int_{\partial\Omega_e} \phi_i^e \{\alpha_k\} nds - u\int_{\Omega_e} \alpha_k \frac{\partial}{\partial x}\phi_i^e d\Omega = 0. \tag{3.54}$$

The weak form of the density equation becomes,

$$\int_{\Omega_e} \phi_i^e \frac{\partial}{\partial t}(\alpha_k\rho_k) d\Omega + \int_{\partial\Omega_e} \phi_i^e \widehat{[\alpha_k\rho_k u]} nds - \int_{\Omega_e} (\alpha_k\rho_k u)\frac{\partial}{\partial x}\phi_i^e d\Omega. \tag{3.55}$$

In the case of an isolated interface,

$$\int_{\Omega_e} \phi_i^e \frac{\partial}{\partial t}(\alpha_k\rho_k) d\Omega + u\rho_k\int_{\partial\Omega_e} \phi_i^e \widehat{[\alpha_k]} nds - u\rho_k\int_{\Omega_e} \alpha_k \frac{\partial}{\partial x}\phi_i^e d\Omega. \tag{3.56}$$

Notice that this does not quite reduce to a repeat of Eqn. (3.54), as the surface integral contains $\{\alpha_k\}$, which is only the central flux term (not including the stabilization term) of $\widehat{[\alpha_k]}$. As numerical dissipation is applied to the volume fraction field via Eqn. (3.53), while the re-worked version of this equation Eqn. (3.54) may appear to be missing a source of dissipation, in practice this is not so. So, we conjecture that $\widehat{[\alpha_k]}$ is sufficiently approximated by $\{\alpha_k\}$ for the purposes of well-balancedness, and continue with the analysis. The results of Chapter 7 verify this conjecture. Thus, we obtain,

$$\int_{\Omega_e} \phi_i^e \frac{\partial}{\partial t}\rho_k d\Omega = 0. \tag{3.57}$$

In 1-D, the weak form of the momentum equation becomes,

$$\int_{\Omega_e} \phi_i^e \frac{\partial}{\partial t}(\rho u) d\Omega + \int_{\partial\Omega_e} \phi_i^e \widehat{(\rho u^2 + p)} nds - \int_{\Omega_e} (\rho u^2 + p)\frac{\partial}{\partial x}\phi_i^e d\Omega = 0. \tag{3.58}$$

For an isolated interface, this becomes,

$$\int_{\Omega_e} \phi_i^e \frac{\partial}{\partial t}(\rho u) d\Omega + u\int_{\partial\Omega_e} \phi_i^e (\widehat{\rho u}) nds - u^2\int_{\Omega_e} \rho\frac{\partial}{\partial x}\phi_i^e d\Omega = 0, \tag{3.59}$$

where we have broken up $\widehat{\rho u^2 + p}$ to $\widehat{\rho u^2} + p$ and factored out one u as in Section 3.5.1. Inserting the definition $\rho = \alpha_1\rho_1 + \alpha_2\rho_2$, we can further write $(\alpha_1\widehat{\rho_1 + \alpha_2\rho_2})u$ as $\widehat{\alpha_1\rho_1 u} + \widehat{\alpha_2\rho_2 u}$ as in Section 3.5.1, obtaining:

$$\begin{aligned}\rho\int_{\Omega_e} \phi_i^e \frac{\partial}{\partial t} u d\Omega + u\int_{\Omega_e} \phi_i^e \frac{\partial}{\partial t}(\alpha_1\rho_1) d\Omega + u\int_{\Omega_e} \phi_i^e \frac{\partial}{\partial t}(\alpha_2\rho_2) d\Omega \\ + u\int_{\partial\Omega_e} \phi_i^e \widehat{\alpha_1\rho_1 u} nds + u\int_{\partial\Omega_e} \phi_i^e \widehat{\alpha_2\rho_2 u} nds \\ - u^2\int_{\Omega_e} \alpha_1\rho_1\frac{\partial}{\partial x}\phi_i^e d\Omega - u^2\int_{\Omega_e} \alpha_2\rho_2\frac{\partial}{\partial x}\phi_i^e d\Omega = 0.\end{aligned} \tag{3.60}$$

All but the first term can be identified as u times Eqn. (3.56) and set to zero, leaving us with:

$$\int_{\Omega_e} \phi_i^e \frac{\partial}{\partial t} u d\Omega = 0. \tag{3.61}$$

such that velocity equilibrium is maintained.

In 1-D, the weak form of the phasic energy equation becomes,

$$\begin{aligned}
&\int_{\Omega_e} \phi_i^e \frac{\partial}{\partial t}(\alpha_k \rho_k E_k) d\Omega + \int_{\partial\Omega_e} \phi_i^e [u(\widehat{\alpha_k \rho_k E_k + \alpha_k p_k})] n ds - \int_{\Omega_e} [u(\alpha_k \rho_k E_k + \alpha_k p_k)] \frac{\partial}{\partial x} \phi_i^e d\Omega \\
&- \int_{\partial\Omega_e} \frac{1}{2} \phi_i^e \{u z_k\} [[p]] n ds + \int_{\Omega_e} \phi_i^e u z_k \frac{\partial}{\partial x} p d\Omega + \int_{\partial\Omega_e} \frac{1}{2} \phi_i^e \{u\} [[\alpha_k p_k]] n ds - \int_{\Omega_e} \phi_i^e u \frac{\partial}{\partial x} \alpha_k p_k d\Omega = 0.
\end{aligned} \tag{3.62}$$

For an ideal gas,

$$\begin{aligned}
&\int_{\Omega_e} \phi_i \frac{\partial}{\partial t}(\alpha_k \frac{p_k}{\gamma_k - 1} + \frac{1}{2}\alpha_k \rho_k u^2) d\Omega + \int_{\partial\Omega_e} \phi_i^e [u(\widehat{\alpha_k \frac{p_k}{\gamma_k - 1} + \frac{1}{2}\alpha_k \rho_k u^2} + \alpha_k p_k)] n ds \\
&\qquad - \int_{\Omega_e} [u(\alpha_k \frac{p_k}{\gamma_k - 1} + \frac{1}{2}\alpha_k \rho_k u^2 + \alpha_k p_k)] \frac{\partial}{\partial x} \phi_i^e d\Omega \\
&- \int_{\partial\Omega_e} \frac{1}{2} \phi_i^e \{u z_k\} [[p]] n ds + \int_{\Omega_e} \phi_i^e u z_k \frac{\partial}{\partial x} p d\Omega + \int_{\partial\Omega_e} \frac{1}{2} \phi_i^e \{u\} [[\alpha_k p_k]] n ds - \int_{\Omega_e} \phi_i^e u \frac{\partial}{\partial x} \alpha_k p_k d\Omega = 0.
\end{aligned} \tag{3.63}$$

In the case of an isolated interface,

$$\begin{aligned}
&\int_{\Omega_e} \phi_i \frac{\partial}{\partial t}(\alpha_k \frac{p_k}{\gamma_k - 1} + \frac{1}{2}\alpha_k \rho_k u^2) d\Omega + \int_{\partial\Omega_e} \phi_i^e [u(\widehat{\alpha_k \frac{p_k}{\gamma_k - 1} + \frac{1}{2}\alpha_k \rho_k u^2} + \alpha_k p_k)] n ds \\
&\qquad - u \int_{\Omega_e} [\alpha_k \frac{p_k}{\gamma_k - 1} + \frac{1}{2}\alpha_k \rho_k u^2 + \alpha_k p_k] \frac{\partial}{\partial x} \phi_i^e d\Omega \\
&\qquad + u \int_{\partial\Omega_e} \frac{1}{2} \phi_i^e [[\alpha_k p_k]] n ds - u \int_{\Omega_e} \phi_i^e \frac{\partial}{\partial x} \alpha_k p_k d\Omega = 0.
\end{aligned} \tag{3.64}$$

We apply the divergence theorem as to obtain Eqn. (3.54),

$$\begin{aligned}
&\int_{\Omega_e} \phi_i \frac{\partial}{\partial t}(\alpha_k \frac{p_k}{\gamma_k - 1} + \frac{1}{2}\alpha_k \rho_k u^2) d\Omega + \int_{\partial\Omega_e} \phi_i^e [u(\widehat{\alpha_k \frac{p_k}{\gamma_k - 1} + \frac{1}{2}\alpha_k \rho_k u^2} + \alpha_k p_k)] n ds \\
&\qquad - u \int_{\Omega_e} [\alpha_k \frac{p_k}{\gamma_k - 1} + \frac{1}{2}\alpha_k \rho_k u^2 + \alpha_k p_k] \frac{\partial}{\partial x} \phi_i^e d\Omega \\
&\qquad - u \int_{\partial\Omega_e} \phi_i^e \{\alpha_k p_k\} n ds + u \int_{\Omega_e} \alpha_k p_k \frac{\partial}{\partial x} \phi_i^e d\Omega = 0.
\end{aligned} \tag{3.65}$$

We may separate the numerical flux $u(\alpha_k \frac{p_k}{\gamma_k - 1} + \widehat{\frac{1}{2}\alpha_k \rho_k} u^2 + \alpha_k p_k)$ into $u(\widehat{\alpha_k \frac{p_k}{\gamma_k - 1} + \frac{1}{2}\alpha_k \rho_k} u^2) + \widehat{u \alpha_k p_k}$, where the term $\widehat{u \alpha_k p_k}$ does not contain a stabilization term, as it appears only in the flux.

Then we can further write $u(\alpha_k \widehat{\frac{p_k}{\gamma_k - 1}} + \widehat{\frac{1}{2}\alpha_k \rho_k u^2})$ as $\widehat{u\alpha_k \frac{p_k}{\gamma_k - 1}} + \widehat{\frac{1}{2}\alpha_k \rho_k u^3}$, where the stabilization term is also split up among the internal energy and kinetic energy contributions accordingly. Because the internal energy and kinetic energy contributions are linearly additive in both the flux $u\alpha_k \rho_k E_k$ and the variable $\alpha_k \rho_k E_k$, this can be done consistently. We obtain,

$$\begin{aligned}
&\int_{\Omega_e} \phi_i^e \frac{\partial}{\partial t}(\alpha_k \frac{p_k}{\gamma_k - 1}) d\Omega + \int_{\Omega_e} \phi_i^e \frac{\partial}{\partial t}(\frac{1}{2}\alpha_k \rho_k u^2) d\Omega \\
&\qquad + \int_{\partial\Omega_e} \phi_i^e \widehat{u\alpha_k \frac{p_k}{\gamma_k - 1}} nds + \int_{\partial\Omega_e} \phi_i^e \widehat{\frac{1}{2}\alpha_k \rho_k u^3} nds + \int_{\partial\Omega_e} \phi_i^e \widehat{u\alpha_k p_k} nds \\
&- u \int_{\partial\Omega_e} \phi_i^e \{\alpha_k p_k\} nds - u \int_{\Omega_e} [(\alpha_k \frac{p_k}{\gamma_k - 1} + \frac{1}{2}\alpha_k \rho_k u^2 + \alpha_k p_k) - \alpha_k p_k] \frac{\partial}{\partial x} \phi_i^e d\Omega = 0. \quad (3.66)
\end{aligned}$$

Noting that $u\{\alpha_k p_k\}$ and $\widehat{[u\alpha_k p_k]}$ are the same quantity, we simplify,

$$\begin{aligned}
&\int_{\Omega_e} \phi_i^e \frac{\partial}{\partial t}(\alpha_k \frac{p_k}{\gamma_k - 1}) d\Omega + \int_{\Omega_e} \phi_i^e \frac{\partial}{\partial t}(\frac{1}{2}\alpha_k \rho_k u^2) d\Omega \\
&\qquad + \int_{\partial\Omega_e} \phi_i^e \widehat{u\alpha_k \frac{p_k}{\gamma_k - 1}} nds + \int_{\partial\Omega_e} \phi_i^e \widehat{\frac{1}{2}\alpha_k \rho_k u^3} nds \\
&\qquad - u \int_{\Omega_e} [\alpha_k \frac{p_k}{\gamma_k - 1} + \frac{1}{2}\alpha_k \rho_k u^2] \frac{\partial}{\partial x} \phi_i^e d\Omega = 0. \quad (3.67)
\end{aligned}$$

Removing the velocity u from integrals where possible,

$$\begin{aligned}
&\int_{\Omega_e} \phi_i^e \frac{\partial}{\partial t}(\alpha_k \frac{p_k}{\gamma_k - 1}) d\Omega + \frac{p_k}{\gamma_k - 1} \int_{\partial\Omega_e} \phi_i^e (\widehat{u\alpha_k}) nds - u \frac{p_k}{\gamma_k - 1} \int_{\Omega_e} \alpha_k \frac{\partial}{\partial x} \phi_i^e d\Omega \\
&\quad + \frac{1}{2}\rho_k u^2 \int_{\Omega_e} \phi_i^e \frac{\partial}{\partial t} \alpha_k d\Omega + \frac{1}{2}\rho_k u^2 \int_{\partial\Omega_e} \phi_i^e (\widehat{u\alpha_k}) nds - \frac{1}{2}\rho_k u^3 \int_{\Omega_e} \alpha_k \frac{\partial}{\partial x} \phi_i^e d\Omega = 0, \quad (3.68)
\end{aligned}$$

we may use Eqn. (3.54) to recover,

$$\int_{\Omega_e} \phi_i^e \frac{\partial}{\partial t} p_k d\Omega = 0, \quad (3.69)$$

such that the uniformity of the material pressure p_k is maintained. It is relatively straightforward to show that if we guarantee the condition $\sum_k \alpha_k = 1$ for all time, the bulk pressure p is well-balanced as well.

3.5.3. Analysis of the Spatial-Averaging Discretization

We will now examine the properties of the spatial-averaging discretization of Section 3.4 in the case of an isolated interface. In 1-D the weak form for the volume fraction equation becomes:

$$\int_{\Omega_e} \phi_i^e \frac{\partial}{\partial t} \alpha_k d\Omega + \int_{\partial\Omega_e} \phi_i^e (\widehat{\alpha_k u} - \overline{\alpha}_k \widehat{u}) nds - \int_{\Omega_e} (\alpha_k - \overline{\alpha}_k) u \frac{\partial}{\partial x} \phi_i^e d\Omega = 0. \quad (3.70)$$

For an isolated interface, $\widehat{u} = u$ is uniform initially, and we have,

$$\int_{\Omega_e} \phi_i^e \frac{\partial}{\partial t} \alpha_k d\Omega + \int_{\partial\Omega_e} \phi_i^e (\widehat{\alpha_k u}) n ds - u \int_{\Omega_e} \alpha_k \frac{\partial}{\partial x} \phi_i^e d\Omega = 0. \tag{3.71}$$

Here, the numerical flux $\widehat{\alpha_k u}$ contains a stabilization term, so we do not remove u from the flux as it may not be factored from the stabilization term.

We also note that, in the case of pure flow, where α_k is uniform, even in the presence of a velocity gradient, so long as the discretization of $\widehat{u}$ is consistent with the appearance of u in the numerical flux $\widehat{\alpha_k u}$, the volume fraction will remain uniform.

In 1-D, the weak form of the density equation becomes,

$$\int_{\Omega_e} \phi_i^e \frac{\partial}{\partial t} (\alpha_k \rho_k) d\Omega + \int_{\partial\Omega_e} \phi_i^e (\widehat{\alpha_k \rho_k u}) n ds - \int_{\Omega_e} \alpha_k \rho_k u \frac{\partial}{\partial x} \phi_i^e d\Omega = 0. \tag{3.72}$$

In the case of an isolated interface,

$$\int_{\Omega_e} \phi_i^e \frac{\partial}{\partial t} (\alpha_k \rho_k) d\Omega + \rho_k \int_{\partial\Omega_e} \phi_i^e (\widehat{\alpha_k u}) n ds - u\rho_k \int_{\Omega_e} \alpha_k \frac{\partial}{\partial x} \phi_i^e d\Omega = 0. \tag{3.73}$$

We may factor out the uniform ρ_k from the numerical flux $\widehat{\alpha_k \rho_k u}$ because it appears in the variable $\alpha_k \rho_k$, not just in the flux $\alpha_k \rho_k u$. Because it appears only in the flux and may not be factored out of the stabilization term, we do not factor out u from $\widehat{\alpha_k \rho_k u}$. Similar to the preceding analyses, we notice that the final two terms of Eqn. (3.73) is ρ_k times the right-hand side of Eqn. (3.71), such that Eqn. (3.73) becomes:

$$\int_{\Omega_e} \phi_i^e \frac{\partial}{\partial t} \rho_k d\Omega = 0. \tag{3.74}$$

In 1-D, the weak form of the momentum equation becomes,

$$\int_{\Omega_e} \phi_i^e \frac{\partial}{\partial t} (\rho u) d\Omega + \int_{\partial\Omega_e} \phi_i^e (\widehat{\rho u^2 + p}) n ds - \int_{\Omega_e} (\rho u^2 + p) \frac{\partial}{\partial x} \phi_i^e d\Omega = 0. \tag{3.75}$$

For an isolated interface,

$$\int_{\Omega_e} \phi_i^e \frac{\partial}{\partial t} (\rho u) d\Omega + u \int_{\partial\Omega_e} \phi_i^e (\widehat{\rho u}) n ds - u^2 \int_{\Omega_e} \rho \frac{\partial}{\partial x} \phi_i^e d\Omega = 0, \tag{3.76}$$

where we have broken up $\widehat{\rho u^2 + p}$ to $\widehat{\rho u^2} + p$ and factored out one u as in Section 3.5.1. Inserting the definition $\rho = \alpha_1 \rho_1 + \alpha_2 \rho_2$, we can further write $(\widehat{\alpha_1 \rho_1 + \alpha_2 \rho_2})u$ as $\widehat{\alpha_1 \rho_1 u} + \widehat{\alpha_2 \rho_2 u}$ as in Section 3.5.1, obtaining:

$$\begin{aligned} \rho \int_{\Omega_e} \phi_i^e \frac{\partial}{\partial t} u d\Omega + u \int_{\Omega_e} \phi_i^e \frac{\partial}{\partial t} (\alpha_1 \rho_1) d\Omega + u \int_{\Omega_e} \phi_i^e \frac{\partial}{\partial t} (\alpha_2 \rho_2) d\Omega \\ + u \int_{\partial\Omega_e} \phi_i^e (\widehat{\alpha_1 \rho_1 u}) n ds + u \int_{\partial\Omega_e} \phi_i^e (\widehat{\alpha_2 \rho_2 u}) n ds \\ - u^2 \int_{\Omega_e} \alpha_1 \rho_1 \frac{\partial}{\partial x} \phi_i^e d\Omega - u^2 \int_{\Omega_e} \alpha_2 \rho_2 \frac{\partial}{\partial x} \phi_i^e d\Omega = 0. \end{aligned} \tag{3.77}$$

All but the first term can be identified as u times Eqn. (3.73) and set to zero, leaving us with

$$\int_{\Omega_e} \phi_i^e \frac{\partial}{\partial t} u d\Omega = 0, \tag{3.78}$$

such that velocity equilibrium is maintained.

The weak form of the energy equation becomes, in 1-D,

$$\int_{\Omega_e} \phi_i^e \frac{\partial}{\partial t}(\alpha_k \rho_k E_k) d\Omega + \int_{\partial\Omega_e} \phi_i^e [u(\alpha_k \widehat{\rho_k E_k + \alpha_k p_k}) + \overline{z_k u}\widehat{p} - \overline{u}\widehat{\alpha_k p_k}] n ds$$
$$- \int_{\Omega_e} [u(\alpha_k \rho_k E_k + \alpha_k p_k) + \overline{z_k u} p - \overline{u}\alpha_k p_k] \frac{\partial}{\partial x} \phi_i^e d\Omega = 0. \tag{3.79}$$

For an ideal gas,

$$\int_{\Omega_e} \phi_i^e \frac{\partial}{\partial t}(\alpha_k \frac{p_k}{\gamma_k - 1}) d\Omega + \int_{\Omega_e} \phi_i^e \frac{\partial}{\partial t}(\frac{1}{2}\alpha_k \rho_k u^2) d\Omega$$
$$+ \int_{\partial\Omega_e} \phi_i^e [u(\alpha_k \frac{p_k}{\gamma_k - 1} + \widehat{\frac{1}{2}\alpha_k \rho_k u^2 + \alpha_k p_k}) + \overline{z_k u}\widehat{p} - \overline{u}\widehat{\alpha_k p_k}] n ds$$
$$- \int_{\Omega_e} [u(\alpha_k \frac{p_k}{\gamma_k - 1} + \frac{1}{2}\alpha_k \rho_k u^2 + \alpha_k p_k) + \overline{z_k u} p - \overline{u}\alpha_k p_k] \frac{\partial}{\partial x} \phi_i^e d\Omega = 0. \tag{3.80}$$

As in Section 3.5.2, we separate the numerical flux $u(\alpha_k \frac{p_k}{\gamma_k - 1} + \widehat{\frac{1}{2}\alpha_k \rho_k} u^2 + \alpha_k p_k)$, obtaining,

$$\int_{\Omega_e} \phi_i^e \frac{\partial}{\partial t}(\alpha_k \frac{p_k}{\gamma_k - 1}) d\Omega + \int_{\Omega_e} \phi_i^e \frac{\partial}{\partial t}(\frac{1}{2}\alpha_k \rho_k u^2) d\Omega$$
$$+ \int_{\partial\Omega_e} \phi_i^e u \widehat{\alpha_k \frac{p_k}{\gamma_k - 1}} n ds + \int_{\partial\Omega_e} \phi_i^e \widehat{\frac{1}{2}\alpha_k \rho_k u^3} n ds + \int_{\partial\Omega_e} \phi_i^e \widehat{u \alpha_k p_k} n ds$$
$$+ \int_{\partial\Omega_e} \phi_i^e \overline{z_k u}\widehat{p} n ds - \int_{\partial\Omega_e} \phi_i^e \overline{u}\widehat{\alpha_k p_k} n ds$$
$$- \int_{\Omega_e} [u(\alpha_k \frac{p_k}{\gamma_k - 1} + \frac{1}{2}\alpha_k \rho_k u^2 + \alpha_k p_k) + \overline{z_k u} p - \overline{u}\alpha_k p_k] \frac{\partial}{\partial x} \phi_i^e d\Omega = 0. \tag{3.81}$$

For the isolated interface,

$$\int_{\Omega_e} \phi_i^e \frac{\partial}{\partial t}(\alpha_k \frac{p_k}{\gamma_k - 1}) d\Omega + \frac{p_k}{\gamma_k - 1} \int_{\partial\Omega_e} \phi_i^e (\widehat{u\alpha_k}) n ds - u \frac{p_k}{\gamma_k - 1} \int_{\Omega_e} \alpha_k \frac{\partial}{\partial x} \phi_i^e d\Omega$$
$$+ \frac{1}{2}\rho_k u^2 \int_{\Omega_e} \phi_i^e \frac{\partial}{\partial t} \alpha_k d\Omega + \frac{1}{2}\rho_k u^2 \int_{\partial\Omega_e} \phi_i^e (\widehat{u\alpha_k}) n ds - \frac{1}{2}\rho_k u^3 \int_{\Omega_e} \alpha_k \frac{\partial}{\partial x} \phi_i^e d\Omega$$
$$+ u \int_{\partial\Omega_e} \phi_i^e [\widehat{\alpha_k p_k} - \widehat{\alpha_k p_k}] n ds + up \int_{\partial\Omega_e} \phi_i^e \overline{z_k} n ds - up \int_{\Omega_e} \overline{z_k} \frac{\partial}{\partial x} \phi_i^e d\Omega = 0. \tag{3.82}$$

We recognize that the quantity $\overline{z_k}$ is constant across an element Ω_e, so that similar to p in the momentum equation, it does not contribute. Also, we eliminate the kinetic energy terms using Eqn. (3.71),

$$\int_{\Omega_e} \phi_i^e \frac{\partial}{\partial t}(\alpha_k \frac{p_k}{\gamma_k - 1}) d\Omega + \frac{p_k}{\gamma_k - 1} \int_{\partial\Omega_e} \phi_i^e \widehat{u\alpha_k} n ds \\ + u \int_{\partial\Omega_e} \phi_i^e [\widehat{\alpha_k p_k} - \widehat{\alpha_k p_k}] n ds - u \frac{p_k}{\gamma_k - 1} \int_{\Omega_e} \alpha_k \frac{\partial}{\partial x} \phi_i^e d\Omega = 0. \quad (3.83)$$

As long as the discretization for $\frac{\partial}{\partial x}\alpha_k \rho_k$ is consistent in the numerical flux and the nonconservative term within the surface integral, we can use Eqn. (3.71) to recover:

$$\int_{\Omega_e} \phi_i^e \frac{\partial}{\partial t} p_k d\Omega = 0, \quad (3.84)$$

such that the uniformity of the material pressure p_k is maintained. It is relatively straightforward to show that if we guarantee the condition $\sum_k \alpha_k = 1$ for all time, the bulk pressure p is well-balanced as well.

This page intentionally left blank.

4. SOLUTION LIMITING

Solution limiting is a post-processing step, typically employed at each time-stage of a Runge-Kutta time-stepping method, which limits the allowable values of gradients in the numerical solution to reduce small-scale variation (i.e., numerical oscillations) in the solution. In general, spurious oscillations occur when capturing discontinuous solutions with high-order numerical methods, so some means of reducing solution variation is required. While solution limiting is only one approach that can be used to regularize discontinuities, the wealth of research that has been developed for many decades in the context of slope limiting for high-order finite volume schemes has been widely adapted to limiting discontinuous Galerkin solutions.

It is important in the simulation of material interfaces that the limiting scheme we utilize preserves equilibria of primitive variables. It has been shown that limiting schemes that do not operate on the primitive variables (or characteristic variables) themselves may introduce errors into the primitive variables, violating equilibrium conditions in the primitive variables. This can be avoided by deducing the slopes of our primitive variables, limiting them directly, and recomputing the limited solutions of the conserved variables. This can be shown to not violate the equilibria of primitive variables, such as pressure and temperature [7, 18].

In this chapter, we describe the solution limiting scheme used in the FLEXO code. First, we describe the transformation between the modal representation of the state variables $[\alpha_k, \alpha_k\rho_k, \rho\vec{u}, \alpha_k\rho_k E_k]$ and the modal representation of the primitive variables $[\alpha_k, \rho_k, \vec{u}, \rho_k\varepsilon_k]$. Then, we describe the limiting of the multi-dimensional modal primitive variable solutions.

4.1. Modal Primitive Transformation

In FLEXO, we utilize a Legendre (modal) polynomial basis for the DG solution, so the slope of the solution may be returned trivially by indexing the degrees of freedom appropriately. However, it is important in a multimaterial context that the slopes of the appropriately chosen primitive variables are being limited directly, and that these limited values are then used to compute the slopes of the state variables.

We start with a $P = 1$ modal representation of the state variables $\mathbf{q} = [\alpha_k, \alpha_k\rho_k, \rho\vec{u}, \alpha_k\rho_k E_k]$ in a 3-D reference element Ω_e, $\xi \times \eta \times \gamma \in [-1, 1] \times [-1, 1] \times [-1, 1]$:

$$\mathbf{q}_e = \widehat{\mathbf{q}}_0^e + \widehat{\mathbf{q}}_1^e\xi + \widehat{\mathbf{q}}_2^e\eta + \widehat{\mathbf{q}}_3^e\gamma + \widehat{\mathbf{q}}_4^e\xi\eta + \widehat{\mathbf{q}}_5^e\xi\gamma + \widehat{\mathbf{q}}_6^e\eta\gamma + \widehat{\mathbf{q}}_7^e\xi\eta\gamma. \tag{4.1}$$

In order to unambiguously obtain a modal representation of the primitive variables on Ω_e, we cast this representation to a nodal one, where the degrees of freedom are defined on a collection of $(P + 1)^3$ (to ensure the nodal-modal mapping is invertible) nodes. For convenience, we choose the

element-interior Gaussian quadrature points used for evaluating volume integrals, shown in Fig. 4-1. The modal-to-nodal mapping of the state variables is attained by simply interpolating the

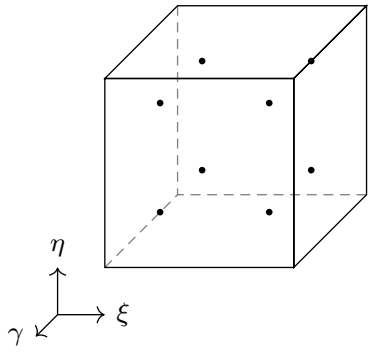

Figure 4-1. Gauss quadrature points (nodes) in 3-D reference element for $P = 1$.

basis:

$$\mathbf{Q}_e(\vec{\xi}_q) = \widehat{\mathbf{q}}_0^e + \widehat{\mathbf{q}}_1^e \xi_q + \widehat{\mathbf{q}}_2^e \eta_q + \widehat{\mathbf{q}}_3^e \gamma_q + \widehat{\mathbf{q}}_4^e \xi_q \eta_q + \widehat{\mathbf{q}}_5^e \xi_q \gamma_q + \widehat{\mathbf{q}}_6^e \eta_q \gamma_q + \widehat{\mathbf{q}}_7^e \xi_q \eta_q \gamma_q, \tag{4.2}$$

where $\mathbf{Q}_e$ denotes the nodal representation of the state variables in element Ω_e. Next, we convert these nodal values to the primitive variables: $\mathbf{Q}_e^* = [\alpha_k, \rho_k, \vec{u}, \rho_k \varepsilon_k]$. Now we use projection to convert the nodal primitive values to a modal representation of the primitive variables $\mathbf{q}_e^*$,

$$\int_{\Omega_e} \phi_i^e \mathbf{q}_e^* d\xi = \int_{\Omega_e} \phi_i^e \mathbf{Q}_e^* d\xi. \tag{4.3}$$

Now that we have a modal representation of the primitive variables, $\mathbf{q}_e^*$, we limit this solution as described in Section 4.2 to obtain the limited modal primitive variables $\widetilde{\mathbf{q}}_e^*$. Then, we interpolate the limited primitive variables back to the interior nodes to obtain $\widetilde{\mathbf{Q}}_e^*(\vec{\xi}_q)$, where we calculate the limited nodal state variables $\widetilde{\mathbf{Q}}_e(\vec{\xi}_q)$, then we use the projection,

$$\int_{\Omega_e} \phi_i^e \widetilde{\mathbf{q}}^e d\xi = \int_{\Omega_e} \phi_i^e \widetilde{\mathbf{Q}}^e d\xi, \tag{4.4}$$

to recover the higher-order terms of the limited 3-D modal representation. By limiting primitive variables and combining their limited slopes in the nodal representation to compute the slopes of the state variables, we do not introduce error into the primitive variables or disturb their equilibria. This is performed during each substep of the Runge-Kutta time-stepping method.

4.2. Modal Slope Limiting

Here, we describe the procedure used to limit the 3-D modal primitive variables from the prior section. We have the modal representation of the primitive variables on element Ω_e,

$$\mathbf{q}_e^* = \widehat{\mathbf{q}}_0^{e*} + \widehat{\mathbf{q}}_1^{e*} \xi + \widehat{\mathbf{q}}_2^{e*} \eta + \widehat{\mathbf{q}}_3^{e*} \gamma + \widehat{\mathbf{q}}_4^{e*} \xi\eta + \widehat{\mathbf{q}}_5^{e*} \xi\gamma + \widehat{\mathbf{q}}_6^{e*} \eta\gamma + \widehat{\mathbf{q}}_7^{e*} \xi\eta\gamma. \tag{4.5}$$

Along each direction, we limit the first-order coefficient by evaluating the slope limiter values as, for example,

$$\boldsymbol{\theta}_{\xi} = \frac{\Delta_{\xi}\mathbf{q}}{\widehat{\mathbf{q}}_1^{e*}}, \tag{4.6}$$

for the vector of primitive variables, where the trial slope is determined by

$$\Delta_{\xi}\mathbf{q} = \text{minmod}(\text{minmod}(\frac{\Delta_L\bar{\mathbf{q}}^*}{\Delta_L\bar{\xi}}, \frac{\Delta_R\bar{\mathbf{q}}^*}{\Delta_R\bar{\xi}}), \widehat{\mathbf{q}}_1^{e*}), \tag{4.7}$$

where the $\bar{()}$ denotes a cell-average and Δ_L and Δ_R are the jumps in a quantity between the element Ω_e and its left and right neighboring elements in the ξ direction. The minmod() function is written briefly as a function of two arguments below:

$$\text{minmod}(a, b) = \frac{1}{2}(\text{sgn}(a) + \text{sgn}(b))\min(|a|, |b|). \tag{4.8}$$

In order to ensure that the limited point-wise values of volume fraction sum to 1,

$$\sum_k \widetilde{(\alpha_k)}^e(\vec{\xi}) = 1, \tag{4.9}$$

we synchronize the values of the solution limiter to be applied to the volume fractions α_k, θ_{ξ,α_k}, as:

$$\theta_{\xi,\alpha_k} = \min_k \theta_{\xi,\alpha_k}. \tag{4.10}$$

We note that this only guarantees Eqn. (4.9) if the volume fractions sum to unity prior to limiting.

We then calculate the slope limiter values for the higher-dimensional cross-terms as, for example,

$$\boldsymbol{\theta}_{\xi\eta} = \min(\boldsymbol{\theta}_{\xi}, \boldsymbol{\theta}_{\eta}), \tag{4.11}$$

and

$$\boldsymbol{\theta}_{\xi\eta\gamma} = \min(\min(\boldsymbol{\theta}_{\xi}, \boldsymbol{\theta}_{\eta}), \boldsymbol{\theta}_{\gamma}). \tag{4.12}$$

This is a greatly simplified version of the concept introduced in Ref. [24]. We note that our approach discards information from the higher-dimensional cross-terms entirely, which is not ideal but is suitable for our current purposes. Then we apply the slope limiters to obtain the limited modal representation of the primitive variables on element Ω_e:

$$\begin{aligned}\widetilde{\mathbf{q}}_e^* = \widehat{\mathbf{q}}_0^{e*} + \widehat{\mathbf{q}}_1^{e*}\boldsymbol{\theta}_{\xi}\xi + \widehat{\mathbf{q}}_2^{e*}\boldsymbol{\theta}_{\eta}\eta + \widehat{\mathbf{q}}_3^{e*}\boldsymbol{\theta}_{\gamma}\gamma \\ + \widehat{\mathbf{q}}_4^{e*}\boldsymbol{\theta}_{\xi\eta}\xi\eta + \widehat{\mathbf{q}}_5^{e*}\boldsymbol{\theta}_{\xi\gamma}\xi\gamma + \widehat{\mathbf{q}}_6^{e*}\boldsymbol{\theta}_{\eta\gamma}\eta\gamma + \widehat{\mathbf{q}}_7^{e*}\boldsymbol{\theta}_{\xi\eta\gamma}\xi\eta\gamma.\end{aligned} \tag{4.13}$$

This page intentionally left blank.

5. BOUNDS PRESERVATION

When solving a system of equations via the DG method, even when using a limiting procedure to limit oscillations near discontinuities, variables may attain unphysical values [15, 30]. This is particularly true when a variable is discontinuous with a very small value on one side, as volume fraction α_k often is. Depending on the variable and its value, unphysical values in the solution can cause a simulation to crash. So, to improve simulation robustness, we employ a relatively simple bounds-preservation approach in the FLEXO code. This bounds-preservation approach has been designed to be consistent with the six-equation model, Eqns. (2.1), in a manner that respects equilibria similar to the limiting scheme described in Chapter 4. This chapter details the bounds-preservation approach used here, with special emphasis on the aspects that are needed to avoid erroneously disturbing equilibria and introducing errors into the solution for the present multimaterial approach.

5.1. Volume Fraction Bounds Preservation

Preserving physicality of the volume fractions α_k is especially important, as the variation in quantities across material interfaces are often "carried" entirely by the volume fractions, and are only present in the state variables in Eqns. (2.1) because these state variables $(\alpha_k\rho_k, \rho u, \alpha_k\rho_k E_k)$ are weighted by the volume fraction. Furthermore, we require that the volume fractions sum to unity at all points in the computational domain, even after bounds preservation has been applied.

We consider a $P = 1$ representation in a 1-D reference element Ω_e, $\xi \in [-1, 1]$:

$$\begin{aligned} (\alpha_k)^e &= (\alpha_k)_0^e + (\alpha_k)_1^e \xi, \quad (\alpha_k\rho_k)^e = (\alpha_k\rho_k)_0^e + (\alpha_k\rho_k)_1^e \xi, \\ (\rho u)^e &= (\rho u)_0^e + (\rho u)_1^e \xi, \quad (\alpha_k\rho_k E_k)^e = (\alpha_k\rho_k E_k)_0^e + (\alpha_k\rho_k E_k)_1^e \xi, \end{aligned} \tag{5.1}$$

subject to a user-input, minimum allowable volume fraction value α_{floor}. We first ensure that the volume fraction mean values are greater than or equal to the minimum allowable value. If not, we set $\widetilde{(\alpha_k)}_0^e = \alpha_{\text{floor}}$, where the tilde indicates that the variable has been bounds preserved, if necessary. As each of the N_m material volume fractions is subject to the same minimum allowable value, the value α_{floor} is used to deduce a maximum allowable value as well, $\alpha_{\text{ceil}} = 1 - \alpha_{\text{floor}}(N_m - 1)$. We also check that the volume fraction mean values are all below this value. If not, we set $\widetilde{(\alpha_k)}_0^e = \alpha_{\text{ceil}}$. We then re-normalize the element-averaged volume fractions over all materials, ensuring that:

$$\sum_k \widetilde{(\alpha_k)}_0^e = 1. \tag{5.2}$$

In order to preserve the equilibrium of other quantities that are weighted by α_k, we need to change their element mean values accordingly:

$$\begin{aligned}
\widetilde{(\rho_k\alpha_k)}_0^e &= \widetilde{(\alpha_k)}_0^e (\rho_k)_0^e / (\alpha_k)_0^e, \\
\widetilde{(\rho u)}_0^e &= \sum_k \left[\widetilde{(\rho_k\alpha_k)}_0^e \right] u_0^e, \\
\widetilde{(\alpha_k\rho_k E_k)}_0^e &= \widetilde{(\alpha_k)}_0^e (\rho_k E_k)_0^e / (\alpha_k)_0^e.
\end{aligned} \tag{5.3}$$

This ensures that the means of the primitive variables ρ_k, u, and $\rho_k E_k$ are unchanged by the bounds preservation of the variables α_k. This procedure affects conservation in exchange for boundedness, which may be undesirable. In practice, the volume fraction mean values very rarely become unbounded using the spatial-averaging discretization of Section 3.4, and this doesn't occur in any of the test problems of Chapter 7. Ref. [46] shows that this can be guaranteed by a sufficiently small timestep restriction.

Now, we apply the bounding criteria at a sampling of points in element Ω_e, denoted ξ_q, to limit the slope of the volume fraction. This is done by computing corresponding slope limiter values $\theta_{q,k}$, in the case that the point-wise value $\left[\widetilde{(\alpha_k)}_0^e + (\alpha_k)_1^e \xi_q \right]$ is less than α_{floor}, as:

$$\theta_{q,k} = \frac{\widetilde{(\alpha_k)}_0^e - \alpha_{\text{floor}}}{\widetilde{(\alpha_k)}_0^e - \left[\widetilde{(\alpha_k)}_0^e + (\alpha_k)_1^e \xi_q \right]}, \tag{5.4}$$

provided that the element mean $\widetilde{(\alpha_k)}_0^e$ is greater than or equal to α_{floor} to ensure $\theta_{q,k} \in [0, 1]$. We take the slope limiter value for the k-th material's volume fraction as,

$$\theta_k = \min_q \theta_{q,k}. \tag{5.5}$$

In order to ensure that the bounded point-wise values of volume fraction sum to 1,

$$\sum_k \widetilde{(\alpha_k)}^e(\xi) = 1, \tag{5.6}$$

we synchronize the $\theta_{q,k}$ values as:

$$\theta = \min_k \theta_k. \tag{5.7}$$

Now, we may apply the θ values to the volume fraction, as well as to the variables that are weighted by the volume fraction:

$$\begin{aligned}
\widetilde{(\alpha_k)}_1^e &= \theta \left[(\alpha_k)_1^e \right], \\
\widetilde{(\alpha_k\rho_k)}_1^e &= \theta \left[(\alpha_k\rho_k)_1^e \right], \\
\widetilde{(\rho u)}_1^e &= \sum_k \left[\widetilde{(\alpha_k\rho_k)}_1^e \right] u_1^e, \\
\widetilde{(\alpha_k\rho_k E_k)}_1^e &= \theta \left[(\alpha_k\rho_k E_k)_1^e \right].
\end{aligned} \tag{5.8}$$

This approach is sufficient to ensure that the primitive variables ρ_k, u, and $\rho_k E_k$ are not disturbed by the volume fraction bounds-preservation procedure. Thus, we obtain the variables:

$$\begin{aligned} \widetilde{(\alpha_k)}^e &= \widetilde{(\alpha_k)}_0^e + \widetilde{(\alpha_k)}_1^e \xi, \quad \widetilde{(\alpha_k \rho_k)}^e = \widetilde{(\alpha_k \rho_k)}_0^e + \widetilde{(\alpha_k \rho_k)}_1^e \xi, \\ \widetilde{(\rho u)}^e &= \widetilde{(\rho u)}_0^e + \widetilde{(\rho u)}_1^e \xi, \quad \widetilde{(\alpha_k \rho_k E_k)}^e = \widetilde{(\alpha_k \rho_k E_k)}_0^e + \widetilde{(\alpha_k \rho_k E_k)}_1^e \xi, \end{aligned} \tag{5.9}$$

where the volume fractions have been bounds-preserved and the other variables have been altered accordingly, in a manner that preserves equilibria of the primitive variables.

5.2. State Variable Bounds Preservation

An additional step of bounds preservation can be applied to the state variables $\alpha_k \rho_k$ and $\alpha_k \rho_k E_k$. This is useful for problems that feature large gradients in density, pressure, and/or temperature. This section assumes volume fraction bounds preservation has already been applied as described in Section 5.1.

5.2.1. Partial Density Bounds Preservation

We consider a $P = 1$ representation in a 1-D reference element Ω_e, $\xi \in [-1, 1]$:

$$\begin{aligned} (\alpha_k)^e &= (\alpha_k)_0^e + (\alpha_k)_1^e \xi, \quad (\alpha_k \rho_k)^e = (\alpha_k \rho_k)_0^e + (\alpha_k \rho_k)_1^e \xi, \\ (\rho u)^e &= (\rho u)_0^e + (\rho u)_1^e \xi, \quad (\alpha_k \rho_k E_k)^e = (\alpha_k \rho_k E_k)_0^e + (\alpha_k \rho_k E_k)_1^e \xi, \end{aligned} \tag{5.10}$$

subject to user-input, minimum allowable material density values $\rho_{k,\text{floor}}$. We first ensure that the mean value of $\alpha_k \rho_k$ is greater than or equal to the minimum permissible value:

$$(\alpha_k \rho_k)_{0,\text{floor}} = (\alpha_k)_0^e \rho_{k,\text{floor}}. \tag{5.11}$$

If not, we set $\widetilde{(\alpha_k \rho_k)}_0^e = (\alpha_k \rho_k)_{0,\text{floor}}$. In this case, to preserve the equilibrium of other quantities that are weighted by $\alpha_k \rho_k$, we need to change their element mean values accordingly:

$$\begin{aligned} \widetilde{(\rho u)}_0^e &= \sum_k \left[\widetilde{(\rho_k \alpha_k)}_0^e \right] u_0^e, \\ \widetilde{(\alpha_k \rho_k E_k)}_0^e &= \widetilde{(\alpha_k \rho_k)}_0^e (E_k)_0^e / (\alpha_k \rho_k)_0^e. \end{aligned} \tag{5.12}$$

Now, we apply the bounding criteria at a sampling of points in element Ω_e, denoted ξ_q, to limit the slope of the partial density. This is done by computing corresponding slope limiter values $\theta_{q,k}$, in the case that the point-wise value $\left[\widetilde{(\alpha_k \rho_k)}_0^e + (\alpha_k \rho_k)_1^e \xi_q \right]$ is less than $(\alpha_k \rho_k)_{q,\text{floor}} = \left[\widetilde{(\alpha_k)}_0^e + (\alpha_k)_1^e \xi_q \right] \rho_{k,\text{floor}}$, as:

$$\theta_{q,k} = \frac{\widetilde{(\alpha_k \rho_k)}_0^e - (\alpha_k \rho_k)_{q,\text{floor}}}{\widetilde{(\alpha_k \rho_k)}_0^e - \left[\widetilde{(\alpha_k \rho_k)}_0^e + (\alpha_k \rho_k)_1^e \xi_q \right]}, \tag{5.13}$$

provided that the element mean $\widetilde{(\alpha_k\rho_k)}_0^e$ is greater than or equal to $(\alpha_k\rho_k)_{q,\text{floor}}$ to ensure $\theta_{q,k} \in [0,1]$. We take the slope limiter value for the k-th material's partial density as,

$$\theta_k = \min_q \theta_{q,k}. \tag{5.14}$$

Now, we may apply the θ_k values to the partial density, as well as to the variables that are weighted by the partial density:

$$\begin{aligned}
\widetilde{(\alpha_k\rho_k)}_1^e &= \theta_k \left[(\alpha_k\rho_k)_1^e\right], \\
\widetilde{(\rho u)}_1^e &= \sum_k \left[\widetilde{(\alpha_k\rho_k)}_1^e\right] u_1^e, \\
\widetilde{(\alpha_k\rho_k E_k)}_1^e &= \theta_k \left[(\alpha_k\rho_k E_k)_1^e\right].
\end{aligned} \tag{5.15}$$

This approach is sufficient to ensure that the primitive variables u and $\rho_k E_k$ are not disturbed by the partial density bounds-preservation procedure. Thus, we obtain the variables:

$$\begin{aligned}
\widetilde{(\alpha_k\rho_k)}^e &= \widetilde{(\alpha_k\rho_k)}_0^e + \widetilde{(\alpha_k\rho_k)}_1^e \xi, \\
\widetilde{(\rho u)}^e &= \widetilde{(\rho u)}_0^e + \widetilde{(\rho u)}_1^e \xi, \\
\widetilde{(\alpha_k\rho_k E_k)}^e &= \widetilde{(\alpha_k\rho_k E_k)}_0^e + \widetilde{(\alpha_k\rho_k E_k)}_1^e \xi,
\end{aligned} \tag{5.16}$$

where the phasic densities have been bounds-preserved and the other variables have been altered accordingly, in a manner that preserves equilibria of the primitive variables.

It is important to note that altering the partial total energies, as in Eqns. (5.12) and (5.16), will preserve equilibria of the quantity E_k, not of $\rho_k E_k$. Therefore, it will correspond to a change in the material pressure p_k in general. This is likely undesirable, and can be avoided by simply not applying the change in $\alpha_k\rho_k$ to the quantity $\alpha_k\rho_k E_k$.

5.2.2. Partial Total Energy Bounds Preservation

We consider a $P = 1$ representation in a reference element Ω_e in 1-D, $\xi \in [-1, 1]$:

$$(\alpha_k\rho_k E_k)^e = (\alpha_k\rho_k E_k)_0^e + (\alpha_k\rho_k E_k)_1^e \xi, \tag{5.17}$$

subject to user-input, minimum allowable material temperature values $T_{k,\text{floor}}$. We first ensure that the mean value of $\alpha_k\rho_k E_k$ is greater than or equal to the minimum permissible value:

$$(\alpha_k\rho_k E_k)_{0,\text{floor}} = (\alpha_k\rho_k)_0^e \left[e_k((\rho_k)_0^e, T_{k,\text{floor}}) + \frac{1}{2}(u_0^e)^2\right]. \tag{5.18}$$

If not, we set $\widetilde{(\alpha_k\rho_k E_k)}_0^e = (\alpha_k\rho_k E_k)_{0,\text{floor}}$. Now, we apply the bounding criteria at a sampling of points in element Ω_e, denoted ξ_q, to limit the slope of the partial total energy. This is

done by computing corresponding slope limiter values $\theta_{q,k}$, in the case that the point-wise value $\left[(\widetilde{\alpha_k\rho_k E_k})_0^e + (\alpha_k\rho_k E_k)_1^e\xi_q\right]$ is less than,

$$(\alpha_k\rho_k E_k)_{q,\text{floor}} = \left[(\alpha_k\rho_k)_0^e + (\alpha_k\rho_k)_1^e\xi_q\right]\left[e_k((\rho_k)_q^e, T_{k,\text{floor}}) + \frac{1}{2}(u_q^e)^2\right], \tag{5.19}$$

where

$$(\rho_k)_q^e = \frac{(\alpha_k\rho_k)_0^e + (\alpha_k\rho_k)_1^e\xi_q}{(\alpha_k)_0^e + (\alpha_k)_1^e\xi_q}, \tag{5.20}$$

and

$$u_q^e = \frac{(\rho u)_0^e + (\rho u)_1^e\xi_q}{\sum_k\left[(\alpha_k)_0^e + (\alpha_k)_1^e\xi_q\right]}, \tag{5.21}$$

by the following equation:

$$\theta_{q,k} = \frac{(\widetilde{\alpha_k\rho_k E_k})_0^e - (\alpha_k\rho_k E_k)_{q,\text{floor}}}{(\widetilde{\alpha_k\rho_k E_k})_0^e - \left[(\widetilde{\alpha_k\rho_k E_k})_0^e + (\alpha_k\rho_k E_k)_1^e\xi_q\right]}, \tag{5.22}$$

provided that the element mean $(\widetilde{\alpha_k\rho_k E_k})_0^e$ is greater than or equal to $(\alpha_k\rho_k E_k)_{q,\text{floor}}$ to ensure $\theta_{q,k} \in [0,1]$. We take the slope limiter value for the k-th material's partial total energy density as,

$$\theta_k = \min_q \theta_{q,k}. \tag{5.23}$$

Now, we may apply the θ_k values to the partial total energy:

$$(\widetilde{\alpha_k\rho_k E_k})_1^e = \theta_k\left[(\alpha_k\rho_k E_k)_1^e\right]. \tag{5.24}$$

Thus, we obtain the variables:

$$(\widetilde{\alpha_k\rho_k E_k})^e = (\widetilde{\alpha_k\rho_k E_k})_0^e + (\widetilde{\alpha_k\rho_k E_k})_1^e\xi, \tag{5.25}$$

where the partial total energies have been bounds-preserved.

This page intentionally left blank.

6. PRESSURE EQUILIBRATION AND RELAXATION

The six-equation model, Eqns. (2.1), contains source terms in the volume fraction (Eqn. (2.1a)) and energy (Eqn. (2.1d)) equations that act to drive material pressures to their equilibrium values. Thus far, we have ignored these terms in this document. While our analysis of well-balancedness of numerical discretizations in Section 3.5 shows that material pressures p_k should remain uniform across isolated interfaces, one should not expect that these pressures will remain uniform in problems featuring waves such as shocks and rarefactions. In general, if one does not treat these terms, the material pressures p_k may attain unreasonable values, particularly at locations where the corresponding volume fractions α_k are very small. This can be especially problematic in simulations using tabular equations of state, where the pressure values may result in a state that is out of bounds with respect to the tabulated range. Even if one uses a bounds preservation scheme, like that of Chapter 5, this can still put the state of a material in a region of the EOS table that is unreasonable for the simulation conditions, e.g., a different phase.

In the present section, we present a hierarchy of approaches to treat these pressure relaxation terms in Eqns. (2.1). The simplest approach is the *pressure equilibration* approach, inspired by the approach used in the QUINOA code [23]. This involves manually adjusting the material pressures p_k to the mixture pressure p. The next approach is the *instantaneous pressure relaxation* approach [28, 32], in which it is assumed that the timescale associated with the relaxation of the material pressures to their equilibrium value goes to zero. We have extended this approach to arbitrary equations of state and number of materials, which results in iterative root finding via Newton's method to find the equilibrium pressure values. This approach is useful but may encounter robustness issues due to non-convergence. We have found that the most robust approach is to combine the instantaneous relaxation algorithm with the equilibration algorithm.

6.1. Pressure Equilibration

This approach, like that employed in the QUINOA code [23], is essentially a brute-force manipulation of pressure values in the solution to force the material pressures p_k to an equilibrium. This approach avoids the numerical expense of iteration or evaluating the source terms in Eqns. (2.1) explicitly. The underlying assumption of this approach is that while material pressures p_k may be poorly behaved in regions where the corresponding volume fraction α_k is very small, the mixture pressure p tends to be well-behaved. This assumption is well-founded: we observe that when a wave travels through a single-material region where all volume fractions but one are very small and all are uniform, the dominant material is subject to the single material Euler equations, and it is this material's pressure that comprises the vast majority of p.

For this approach, we first interpolate the modal representation of the state variables $[\alpha_k,\ \alpha_k\rho_k,\ \rho\vec{u},\ \alpha_k\rho_k E_k]$ to the element-interior Gaussian quadrature points as in Chapter 4 to obtain a nodal representation of our DG solution on element Ω_e. For each node, we then compute the value of p as well as the values of α_k, ρ_k, ε_k, and p_k for each k. As these are the initial (unequilibrated) values, we henceforth denote them with the superscript $()^0$. If the α_k^0 value is below the maximum volume fraction value to be equilibrated, $\alpha_{\max}$, we assess the internal energy at the bulk pressure p, $\varepsilon_k^1 = \varepsilon_k(\rho_k^0, p)$. Assuming that, in the case that material k is described by an EOS table, this state is on the table, we can simply assess the change in total phasic energy as $\Delta\alpha_k\rho_k E_k = (\alpha_k\rho_k)^0(\varepsilon_k^1 - \varepsilon_k^0)\theta_k$, where the function θ, defined as,

$$\theta_k = \begin{cases} 0 & \text{for } \alpha_k \geq \alpha_{\max} \\ 1 - \frac{\alpha - \alpha_{\min}}{\alpha_{\max} - \alpha_{\min}} & \text{for } \alpha_{\min} < \alpha_k < \alpha_{\max} \\ 1 & \text{for } \alpha_k \leq \alpha_{\min} \end{cases}, \tag{6.1}$$

allows for a continuous "switch" between conditions in which the pressures are to be left alone and equilibrated, as well as makes use of the minimum volume fraction $\alpha_{\min}$, below which everything is equilibrated. When the $\alpha_{\min}$ and $\alpha_{\max}$ values are not both equal to one, we refer to that as "partial pressure equilibration," as the material pressures will not be entirely equilibrated but for a range of volume fraction values will only be equilibrated partially. One would want to do this, perhaps, to establish a better initial state for a more sophisticated but less robust relaxation method, such as the instantaneous pressure relaxation method of Section 6.2. In this work, any time we refer to "partial pressure equilibration," we are taking $\alpha_{\min} = 5 \times 10^{-3}$ and $\alpha_{\max} = 1 \times 10^{-2}$. When we refer to "total pressure equilibration," we are taking $\alpha_{\min} = \alpha_{\max} = 1$.

If the state (ρ_k^0, p) is out of bounds, our approach becomes a bit more complex. We illustrate this case in Figure 6-1. While we cannot attain the simple equilibrium state (ρ_k^0, p), we can move p_k towards p by compromising the material density ρ_k. As we keep the quantity $\alpha_k\rho_k$ constant during this procedure, this corresponds to a change in α_k. This is justified, as Eqn. (2.1a) has a source term from pressure relaxation as well.

The procedure for calculating the equilibrated state in the case that the equilibrated state is out of bounds is subject to the value $\Delta\alpha_{\min}$, the smallest allowable change in volume fraction during the equilibration process. If the equilibrated state (ρ_k^0, p) is off the table (in the case of Fig. 6-1, this state is below the bounding isotherm T_k^b), we evaluate the temperature of the initial state, $T_k^0 = T_k(\rho_k^0, p)$. Then, we calculate the new density $\rho_k^{1*} = \rho_k(T_k^0, p)$ that totally equilibrates the material to the bulk pressure along the original isotherm T_k^0. As the quantity $(\alpha_k\rho_k)^0$ should not change during this process, the change in density $\Delta\rho_k = \rho_k^{1*} - \rho_k^0$ corresponds to a change in volume fraction, $\Delta\alpha_k^* = \alpha_k^{1*} - \alpha_k^0$, where $\alpha_k^{1*} = (\alpha_k\rho_k)^0/\rho_k^{1*}$. This change in volume fraction may be unacceptably large and should be limited each time the equilibration procedure is applied. If $|\Delta\alpha_k^*| > \Delta\alpha_{\min}$, we calculate instead the new volume fraction $\alpha_k^1 = \alpha_k^0 + \text{sign}(\Delta\alpha_k^*)\Delta\alpha_{\min}$, and back out the new density $\rho_k^1 = (\alpha_k\rho_k)^0/\alpha_k^1$, as well as the new pressure and energy $p_k^1 = p_k(\rho_k^1, T_k^0)$ and $\varepsilon_k^1 = \varepsilon_k(\rho_k^1, T_k^0)$. While this approach changes the volume fraction, potentially violating the requirement of $\sum_k \alpha_k = 1$, we apply the volume fraction bounds preservation approach of Section 5.1 afterward, which re-normalizes the volume fraction means ensuring that $\sum_k \alpha_k = 1$, at least in the mean values.

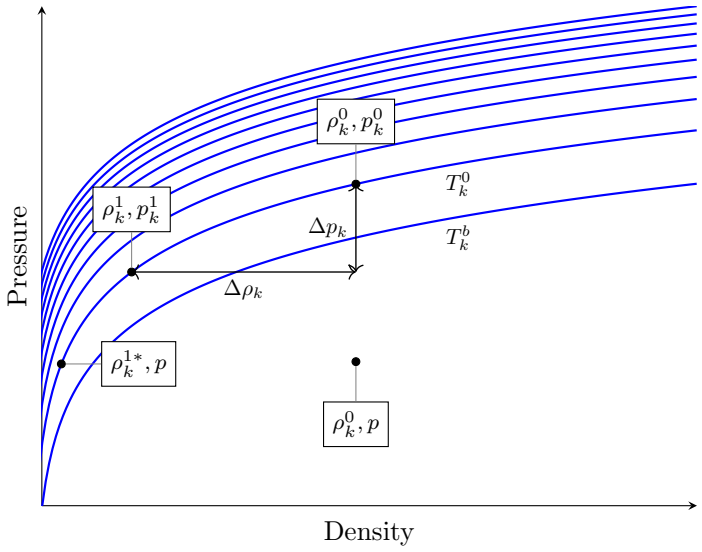

Figure 6-1. Table isotherms (blue lines) and states (black dots) depicting a scenario in which the equilibrated state (ρ_k^0, p) is out of the table bounds. In this case, the equilibration algorithm will use the state (ρ_k^1, p_k^1) instead.

In general, in the case where the equilibrated state is out-of-bounds, there will not be an ideal value of $\Delta\alpha_{\min}$ that allows for a completely equilibrated pressure and a correct solution. With large changes in volume fraction permitted (i.e., large values of $\Delta\alpha_{\min}$), the dynamics of the problem may be affected, causing the bulk pressure to not match exact solutions. However, the pressures are more likely to be completely equilibrated with higher $\Delta\alpha_{\min}$ values. On the other hand, with very restrictive values of $\Delta\alpha_{\min}$, the material pressures attain more extreme out-of-equilibrium values, while the overall solution (including the bulk pressure p) will resemble the solution without pressure equilibrium/relaxation more closely. Therefore, there can be a bit of trial and error in finding an ideal value of $\Delta\alpha_{\min}$. For this work, we use the value $\Delta\alpha_{\min} = 1 \times 10^{-7}$ except where otherwise noted.

It is also crucial that, in the case that the equilibrated state is out of bounds for one or more materials, the other material pressures be altered to avoid changing the bulk pressure p during the equilibration procedure. Fortunately, it is very unlikely that all the materials are out of bounds at the same point, especially in a simulation where some means of pressure equilibration and/or relaxation has been applied throughout the simulated time. This is accomplished by recognizing that $p = \sum_k \alpha_k p_k = \sum_{k_{IB}} \alpha_k p_k + \sum_{k_{OB}} \alpha_k p_k$, where k_{IB} are the material indices of in-bounds materials and k_{OB} are the material indices of out-of-bounds materials. We can recalculate the material pressures for the in-bounds materials (which have not undergone a volume fraction change) assuming an equal division of partial pressure. For an in-bound material, this amounts to calculating

$$p_k^1 = \frac{p - \sum_{k_{OB}} \alpha_k p_k}{N_{m,IB} \alpha_k}, \tag{6.2}$$

where $N_{m,IB}$ is the number of in-bounds materials. We then recalculate $\varepsilon_k^1 = e_k(\rho_k^1, p_k^1)$.

With all the material pressures p_k^1 and energies ε_k^1 obtained, where α_k^1 may be different from α_k^0 for

out-of-bounds materials, we calculate the change in total phasic energy as,

$$\Delta\alpha_k\rho_k E_k = \left[(\alpha_k\rho_k)^0\Delta\varepsilon_k + (\rho_k E_k)^0\Delta\alpha_k\right]\theta_k, \tag{6.3}$$

to account for the volume fraction changes upon the phasic total energy. Finally, we increment the phasic total energies and volume fractions for that nodal point:

$$(\alpha_k\rho_k E_k)^1 = (\alpha_k\rho_k E_k)^0 + \Delta\alpha_k\rho_k E_k, \tag{6.4}$$

and

$$(\alpha_k)^1 = (\alpha_k)^0 + \Delta\alpha_k. \tag{6.5}$$

We perform this procedure for each interior node on each element of the computational mesh, then use the approach of Chapter 4 to project the equilibrated nodal solution back to a modal representation. This is performed during each substep of the Runge-Kutta time-stepping method.

6.2. Instantaneous Pressure Relaxation

In this section, we extend the instantaneous pressure relaxation approach [28, 32] to an arbitrary number of materials and arbitrary (i.e., tabular) equations of state. This approach assumes that the pressure relaxation terms in Eqns. (2.1) drive the pressures to equilibrium instantaneously. In this limit, the governing equations with $\vec{u} = 0$ may be manipulated to yield an algebraic system for the relaxed pressure and volume fraction. Ref. [28] demonstrated that, for a two-material system using the stiffened gas EOS, this system can be analytically solved for the relaxed state. However, our demands require a nonlinear solution of the algebraic system, as the number of materials present and their EOS may be arbitrary. This approach is more sophisticated, though less robust than the equilibration approach of Section 6.1.

We consider an operator-splitting approach, where after updating the system's degrees of freedom using the advective update we are left with the following system of ordinary differential equations,

$$\frac{\partial}{\partial t}\alpha_k = \sum_{j=1}^{N_m}\mu_{kj}(p_k - p_j), \tag{6.6a}$$

$$\frac{\partial}{\partial t}\alpha_k\rho_k = 0, \tag{6.6b}$$

$$\frac{\partial}{\partial t}\rho\vec{u} = 0, \tag{6.6c}$$

$$\frac{\partial}{\partial t}\alpha_k\rho_k E_k = -\sum_{j=1}^{N_m} p_{I,kj}\mu_{kj}(p_k - p_j). \tag{6.6d}$$

We note that $\mu_{kj} = \mu_{jk}$ and in the limit $\mu_{kj} \to +\infty$, corresponding to the timescale of pressure relaxation between p_k and p_j approaching zero, these pressures will approach an equilibrium value $p_{I,kj}$. When this limit applies to all the relaxation coefficients μ_{kj}, the pressures all equilibrate to a

common pressure, $p_{I,kj} \rightarrow p_I$. Discretizing these equations, where we seek the $()^*$ state and begin with the $()^0$ state, we find that

$$(\alpha_k \rho_k)^* = (\alpha_k \rho_k)^0, \qquad (\rho \vec{u})^* = (\rho \vec{u})^0, \tag{6.7}$$

and

$$\frac{\partial}{\partial t} \alpha_k \rho_k E_k = \frac{\partial}{\partial t} \alpha_k \mathcal{E}_k = -p_I \frac{\partial}{\partial t} \alpha_k \tag{6.8}$$

Note that summing Eqn. (6.8) over k reveals that the total energy will be conserved, $\sum_k \partial_t (\alpha_k \rho_k E_k) = \partial_t (\rho E) = 0$, as will the phasic energy density, $\sum_k \partial_t (\alpha_k \mathcal{E}_k) = \partial_t (\mathcal{E}) = 0$ such that $(\rho E)^* = (\rho E)^0$ and $\mathcal{E}^* = \mathcal{E}^0$. Integrating Eqn. (6.8),

$$(\alpha_k E_k)^* - (\alpha_k E_k)^0 = (\alpha_k \mathcal{E}_k)^* - (\alpha_k \mathcal{E}_k)^0 = -\hat{p}_{Ik} (\alpha_k^* - \alpha_k^0) \tag{6.9}$$

Where $\hat{p}_{Ik} = \frac{1}{\alpha_k^* - \alpha_k^0} \int_0^{\Delta t} p_I \frac{\partial \alpha_k}{\partial t} \mathrm{d}t$ is the average interface pressure.

If we enforce mechanical equilibrium, $p_I^* = p_k^* = p^*$, we have N_m equations for $N_m + 1$ unknowns (p^* and α_k^*). We add also the saturation condition, $\sum_k \alpha_k = 1$, so that we now have $N_m + 1$ equations for solving the $N_m + 1$ unknowns.

Solving for α_k^* in Eqn. (6.9),

$$\alpha_k^* = \alpha_k^0 \left(\frac{\mathcal{E}_k^0 + \hat{p}_{Ik}}{\mathcal{E}_k^* + \hat{p}_{Ik}} \right). \tag{6.10}$$

And utilizing the saturation condition,

$$1 = \sum_k \alpha_k^0 \left(\frac{\mathcal{E}_k^0 + \hat{p}_{Ik}}{\mathcal{E}_k^* + \hat{p}_{Ik}} \right) = \sum_k f_k (\rho_k^*, p^*). \tag{6.11}$$

As in Ref. [28], we approximate the value $\hat{p}_{Ik} = \frac{1}{2}(p^* + p_I^0)$, where $p_I^0 = \frac{\sum_k \sum_{k' \neq k} p_k^0 B_{k'}^0}{\sum_k B_k^0}$ and $B_k^0 = \rho_k^0 (c_k^0)^2$. The unknown internal energy density is $\mathcal{E}_k^* = \mathcal{E}_k (\rho_k^*, p^*)$, where $\rho_k^* = (\rho_k \alpha_k)^* / \alpha_k^* = (\rho_k \alpha_k)^0 / \alpha_k^*$.

In Ref. [28], the authors substitute the analytical EOS (stiffened gas) into Eqn. (6.11) so that solving for p^* will result in solving a N-th order polynomial, which was done simply for the $N_m = 2$ case in this reference. This is not possible in general, where our gases obey arbitrary EOS relations, and the $N_m > 2$ case will increase the degree of polynomial to be solved. Instead, we use Newton's method to obtain p^*, in a similar (though more general) manner to that employed in Ref. [32]. In the case of a tabular material, we utilize the differential of a material's pressure,

$$dp_k = \kappa_k d\mathcal{E}_k + \chi_k d\rho_k, \tag{6.12}$$

where $\kappa_k = \frac{\partial p_k}{\partial \mathcal{E}_k}$ and $\chi_k = \frac{\partial p_k}{\partial \rho_k}$. We use an iterative Newton method to obtain p^*, and α_k^* (or, equivalently, ρ_k^*), resulting in,

$$(p^*)^{n+1} = (p^*)^n - \frac{\sum_k f_k \left[(\rho_k^*)^n, (p^*)^n \right] - 1}{\sum_k \frac{\partial f_k}{\partial p^*} \left[(\rho_k^*)^n, (p^*)^n \right]}, \tag{6.13a}$$

$$(\alpha_k^*)^{n+1} = f_k \left[(\rho_k^*)^n, (p^*)^{n+1} \right] \tag{6.13b}$$

where $\frac{\partial f_k}{\partial p^*}(\rho_k^*, p^*) = \frac{\frac{1}{2}}{\frac{\partial \mathcal{E}_k}{\partial p_k}(\rho_k^*, p^*)+\frac{1}{2}} = \frac{\frac{1}{2}}{\frac{1}{\kappa_k(\rho_k^*, p^*)}+\frac{1}{2}}$. We begin with the initial guess $(p^*)^0 = p$, $(\alpha_k^*)^0 = \alpha_k^0$, and iterate to calculate $(p^*)^{n+1}$ and $(\alpha_k^*)^{n+1}$ until these values no longer change within a certain threshold.

Like the equilibration approach of Section 6.1, we perform this procedure on nodally-interpolated values on each element of the computational mesh, then use the approach of Chapter 4 to project the equilibrated nodal solution back to a modal representation. This is performed during each substep of the Runge-Kutta time-stepping method.

We have observed that the robustness of this approach can be mixed when the EOS is described using tables. As a result, we often use the partial pressure equilibration approach of Section 6.1 to provide a more tractable initial state for the instantaneous pressure relaxation algorithm. Furthermore, when this algorithm fails to converge or converges on an unphysical state, we use the total equilibration approach of Section 6.1 instead for that node.

We are currently implementing a finite-pressure relaxation scheme, in which the pressure source terms in Eqns. (2.1a) and (2.1d) are modeled and integrated explicitly, as in Tipton et al. [33] and Pandare et al. [26]. The results with this approach were not yet available when this report was released.

7. VERIFICATION

In this chapter, we test the discretizations of Chapter 3, with particular emphasis on the concept of *well-balancedness* and the differences between the nonconservative discretization approaches using a set of verification problems. Each discretization was implemented in the FLEXO code.

In particular, we plot the numerical solutions and study their errors using a few common error metrics for DG methods. We utilize the global L_2 error in the solution,

$$L_2 = \sqrt{\frac{1}{|\Omega|}\sum_{e=1}^{N_e}\int_{\Omega_e}(q - q^{\text{exact}})^2 d\Omega}, \tag{7.1}$$

and the L_∞ error in the cell-averages,

$$L_\infty = \max_{e=1,\ldots,N_e}\left|\frac{1}{|\Omega_e|}\int_{\Omega_e} q d\Omega - \frac{1}{|\Omega_e|}\int_{\Omega_e} q^{\text{exact}} d\Omega\right|, \tag{7.2}$$

for both the state variables $(\alpha_k\rho_k, \rho u, \alpha_k\rho_k E_k, \alpha_k)$ and primitive variables $(\rho_k, u, p_k, \alpha_k)$. To ensure non-polynomial exact solutions are integrated sufficiently, we use $N_q = 4$ quadrature points for the error evaluations. The optimal rate of convergence for the RKDG method for smooth problems in the global L_2 error is $P + 1$, whereas the cell-average L_∞ error is expected to superconverge at a rate of $2P + 1$.

Each problem in this Chapter was run with $P = 1$, $CFL = 0.5$ and a three-stage Runge Kutta time-stepping method. Additionally, for each of these problems, we choose the "trace" volume fraction to be $\alpha_{\text{trace}} = 1 \times 10^{-8}$. This is the value at which we initialize the volume fraction values α_k that correspond to materials that are not physically present in regions that are meant to be "single-material." Each simulation was ran using the Local Lax-Friedrichs flux, described in Section B.1. The results in this chapter are dimensionless unless units are provided.

7.1. Advection of Smooth 1-D Single-Density Interface

We simulated the advection of a smooth, 1-D, two-material, single-density interface on $x \in [-1, 1]$ with periodic boundaries, upon which we impose the initial condition:

$$\begin{bmatrix}\rho_k \\ u \\ p_k \\ \alpha_1 \\ \alpha_2\end{bmatrix} = \begin{bmatrix} 1.0 \\ 1.0 \\ 1.0 \\ \frac{1}{2}\Big[(1.0 - 2\alpha_{\text{trace}})\cos(\pi x) + 1.0\Big] \\ 1.0 - \alpha_1 \end{bmatrix}. \tag{7.3}$$

For this problem, both material equations of state are described analytically by the ideal gas law, with $\gamma_1 = 1.4$ and $\gamma_2 = 2.0$. This problem was run for a simulated time of $t = 2.0$, corresponding to one period of advection.

Convergence results using the Pandare discretization of Section 3.2 are depicted in Fig. 7-1. We note that all state variables converge at optimal rates, with the exception of the momentum ρu, which converges at a faster rate. For well-balanced schemes, as will be seen, the error for this state variable should be very small, near machine precision. The well-balancedness of the discretization can be further assessed by viewing the convergence behavior of the primitive variables ρ_k, u, and p_k, all of which should be near machine precision for all resolutions for a well-balanced method. The error in ρ_k and u is indeed not small, though they do converge at the same rate as the state variables. The error in p_k, however, is large and converges at a rate that appears to be greater than $m = 1$, though less than optimal in both error measures. Based on this behavior of the material pressures p_k as compared to ρ_k and u, the discretization is not well-balanced for p_k, and this is affecting the errors in ρ_k and u, which themselves would be well-balanced. These errors can be observed as well in the error profiles of Fig. 7-2. It is interesting to note that the error in one material's pressure p_k seems to occur at locations where that material's volume fraction α_k is very small, which we refer to as "trace" regions for that material. These results support that the Pandare discretization is not well-balanced.

Convergence results using the path-conservative discretization of Section 3.3 are depicted in Fig. 7-3. The state variables converge at optimal rates. The primitive variables ρ_k, u, and p_k, are all observed to be near machine precision, demonstrating the behavior of a variable that has "bottomed out", accumulating rounding errors and so increasing slightly with increased resolution. These results verify that the path-conservative discretization is well-balanced.

Convergence results using the spatial-averaging discretization of Section 3.4 are depicted in Fig. 7-4. The state variables converge at optimal rates. The primitive variables ρ_k, u, and p_k are all near machine precision. These results verify that the spatial-averaging discretization is well-balanced.

These results are consistent with the analysis of Section 3.5.

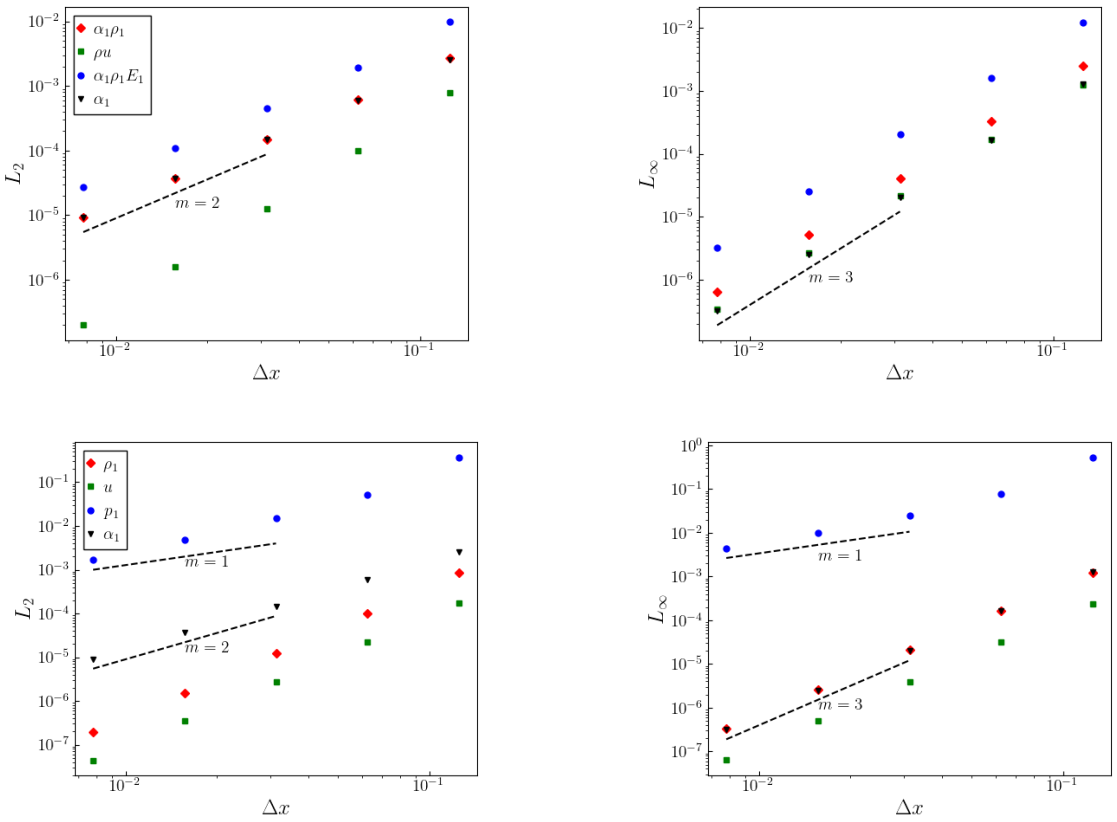

Figure 7-1. Errors in the state variables (top row) and primitive variables (bottom row) for the smooth 1-D single-density interface advection problem after 1 period using the Pandare discretization (Section 3.2). The slopes m of the dashed lines are labeled in each figure.

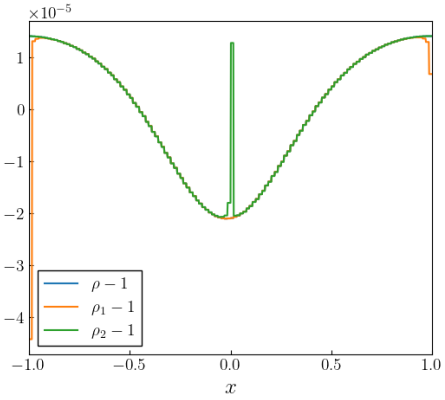

(a) Density error

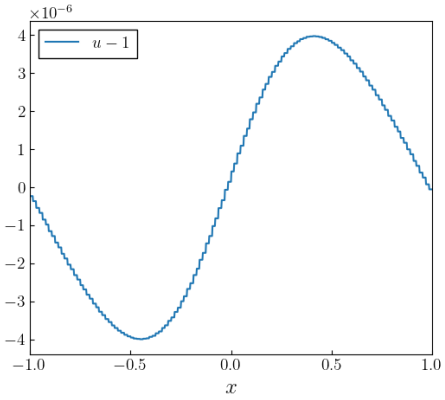

(b) Velocity error

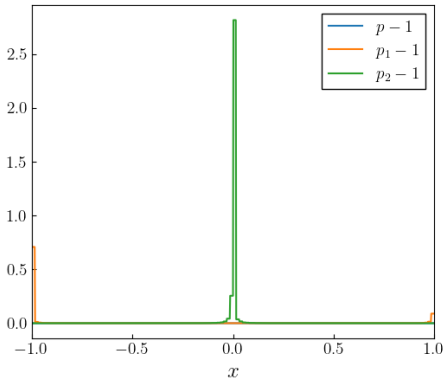

(c) Pressure error

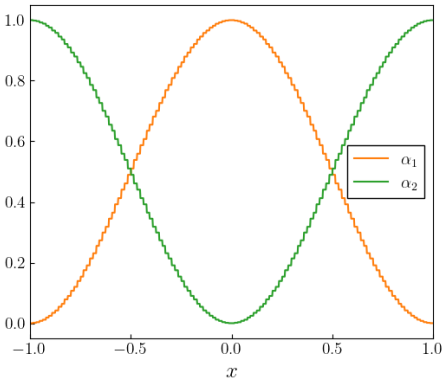

(d) Volume fraction

Figure 7-2. Primitive variable error profiles (a) - (c) and profiles (d) for the smooth 1-D single-density interface advection problem after 1 period using the Pandare discretization (Section 3.2) with $N_e = 64$ elements.

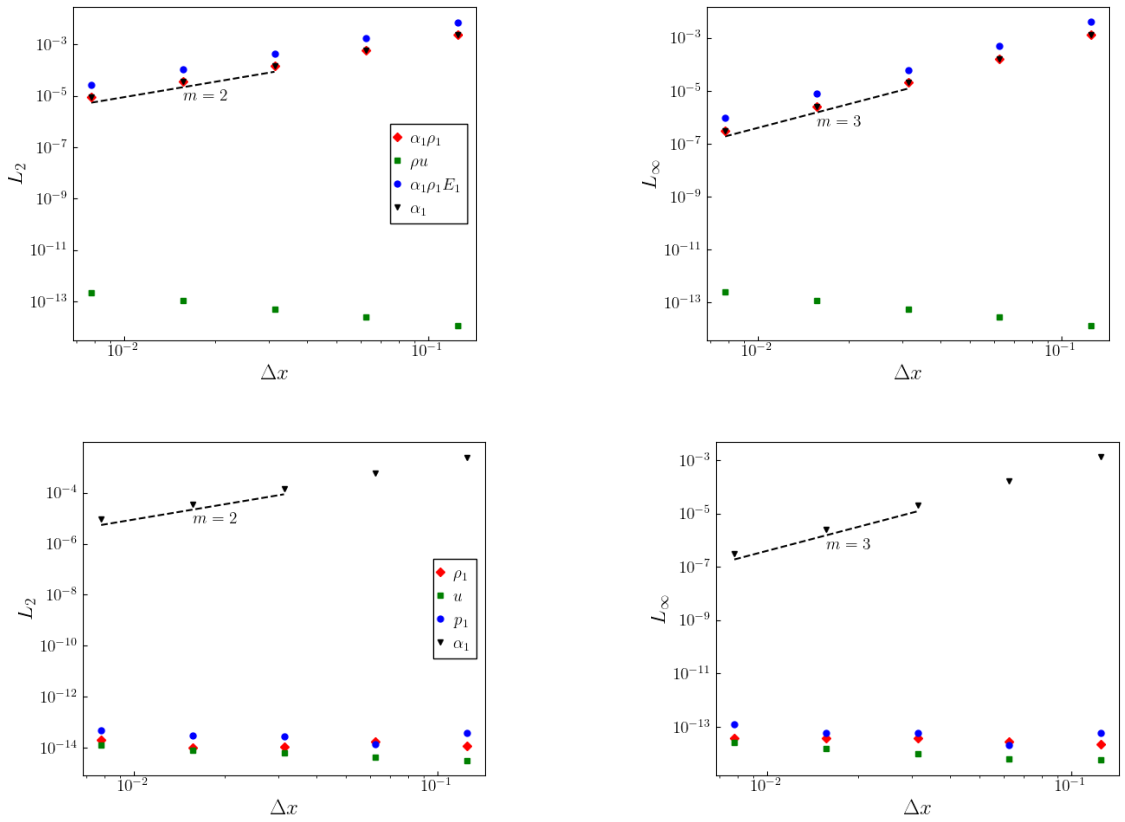

Figure 7-3. Errors in the state variables (top row) and primitive variables (bottom row) for the smooth 1-D single-density interface advection problem after 1 period using the path-conservative discretization (Section 3.3). The slopes m of the dashed lines are labeled in each figure.

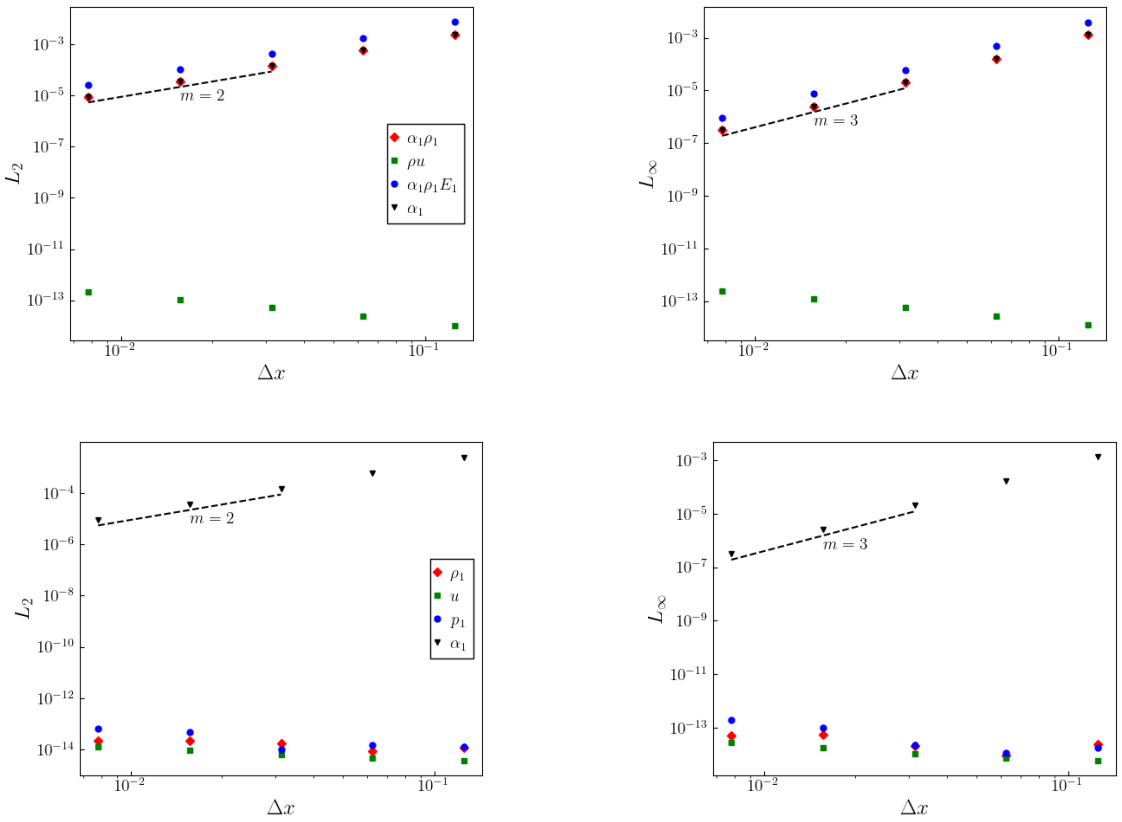

Figure 7-4. Errors in the state variables (top row) and primitive variables (bottom row) for the smooth 1-D single-density interface advection problem after 1 period using the spatial-averaging discretization (Section 3.4). The slopes m of the dashed lines are labeled in each figure.

7.2. Advection of Smooth 1-D Interface

We simulated the advection of a smooth, 1-D, two-material interface on $x \in [-1, 1]$ with periodic boundaries, upon which we impose the initial condition:

$$\begin{bmatrix} \rho_1 \\ \rho_2 \\ u \\ p_k \\ \alpha_1 \\ \alpha_2 \end{bmatrix} = \begin{bmatrix} 1.0 \\ 0.1 \\ 1.0 \\ 1.0 \\ \frac{1}{2}\Big[(1.0 - 2\alpha_{\text{trace}})\cos(\pi x) + 1.0\Big] \\ 1.0 - \alpha_1 \end{bmatrix}. \tag{7.4}$$

For this problem, both material equations of state are described analytically by the ideal gas law, with $\gamma_1 = 1.4$ and $\gamma_2 = 2.0$. This problem was run for a simulated time of $t = 2.0$, corresponding to one period of advection.

The errors using the Pandare discretization, shown in Fig. 7-5, converge optimally for the state variables. However, the primitive errors show that the discretization is not well-balanced, as can also be seen in the profiles of Fig. 7-6. It is important to note that unlike the problem of Section 7.1, in this case the bulk density ρ is not trivially advected, so the momentum ρu is not expected to be near machine precision. For the path-conservative discretization, the results in Fig. 7-7 demonstrate optimal convergence and the discretization is well-balanced, with errors in material densities ρ_k and pressures p_k, as well as the bulk velocity u, near machine precision. Likewise, using the spatial-averaging discretization, the errors depicted in Fig. 7-8 converge optimally and the discretization is well-balanced. These results are consistent with the results of Section 7.1.

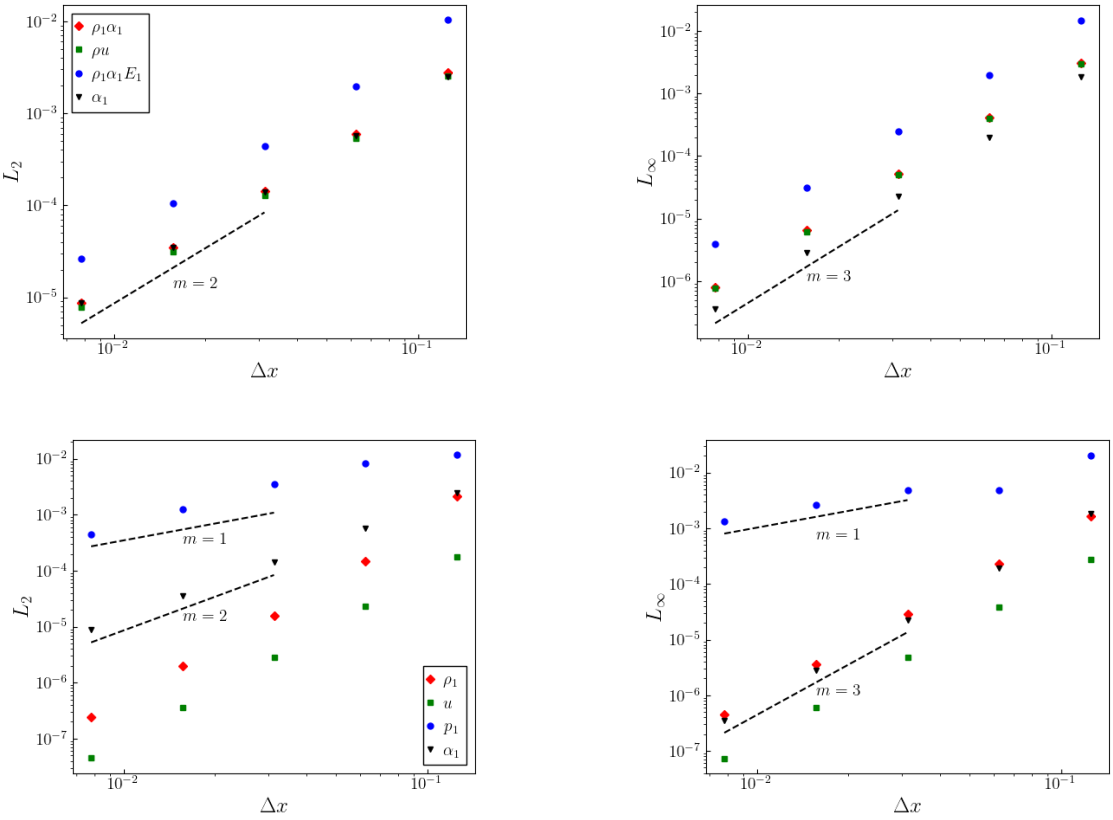

Figure 7-5. Errors in the state variables (top row) and primitive variables (bottom row) for the smooth 1-D interface advection problem after 1 period using the Pandare discretization (Section 3.2). The slopes m of the dashed lines are labeled in each figure.

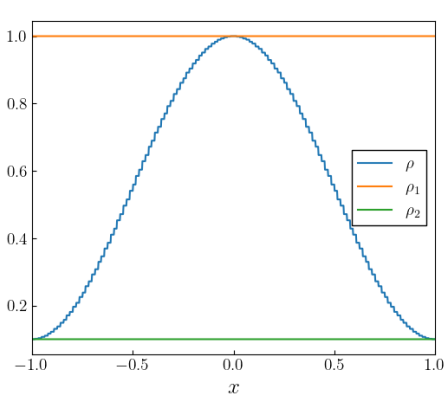

(a) Density

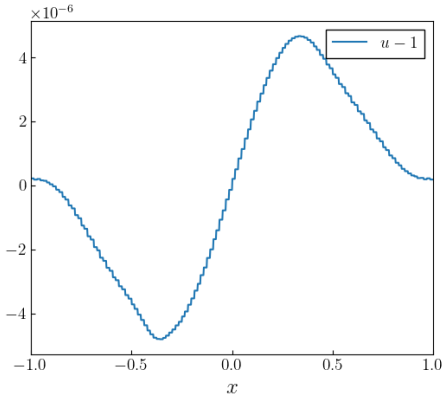

(b) Velocity error

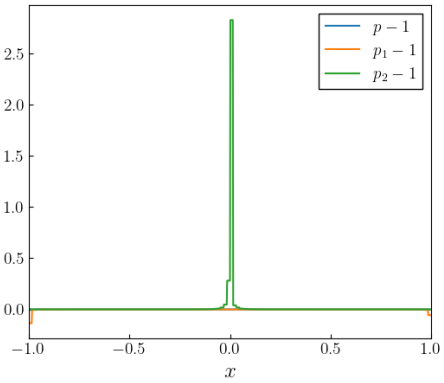

(c) Pressure error

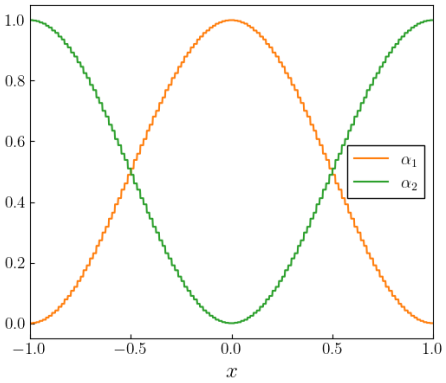

(d) Volume fraction

Figure 7-6. Primitive variable error profiles (b) - (c) and profiles (a) and (d) for the smooth 1-D single-density interface advection problem after 1 period using the Pandare discretization (Section 3.2) with $N_e = 64$ elements.

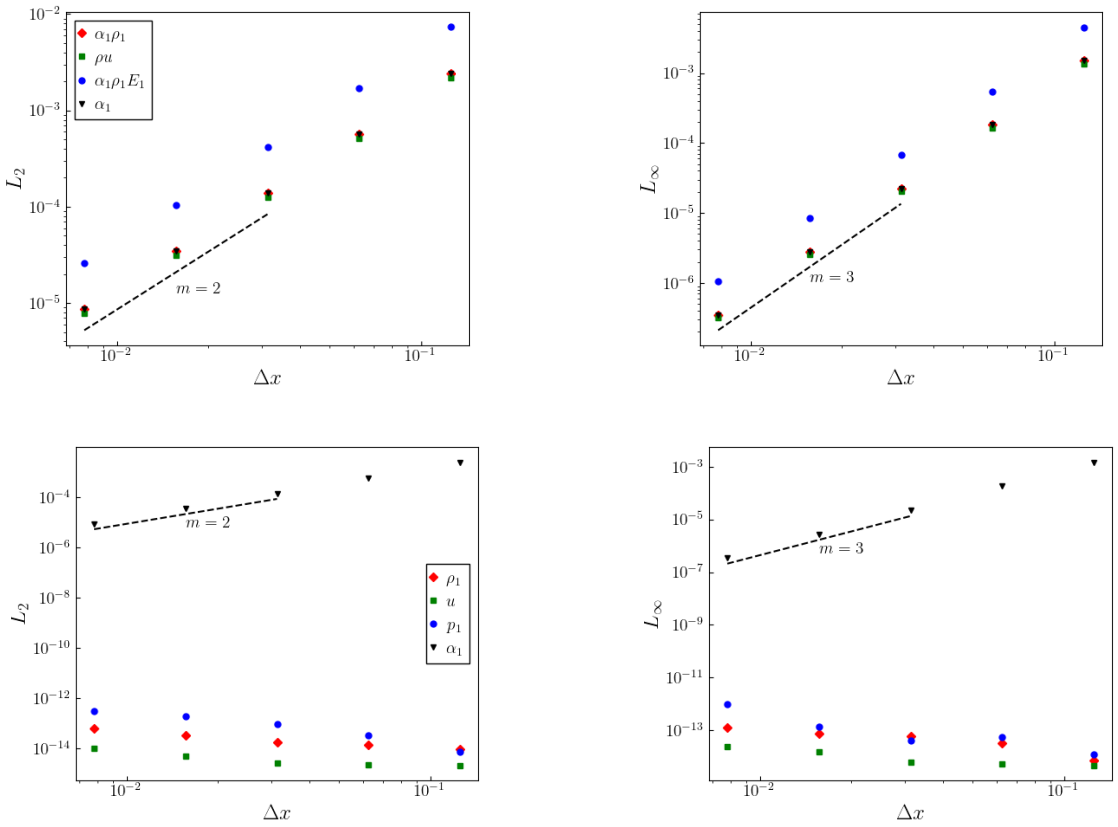

Figure 7-7. Errors in the state variables (top row) and primitive variables (bottom row) for the smooth 1-D interface advection problem after 1 period using the path-conservative discretization (Section 3.3). The slopes m of the dashed lines are labeled in each figure.

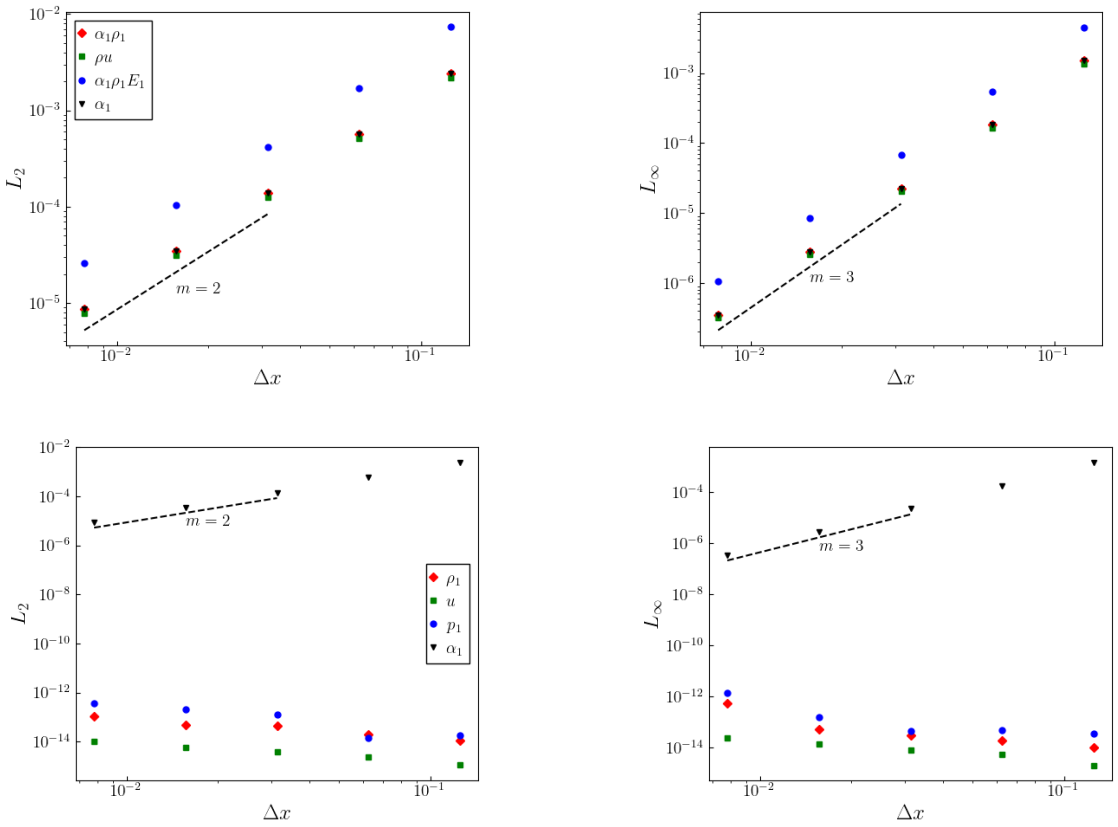

Figure 7-8. Errors in the state variables (top row) and primitive variables (bottom row) for the smooth 1-D interface advection problem after 1 period using the spatial-averaging discretization (Section 3.4). The slopes m of the dashed lines are labeled in each figure.

7.3. Advection of Smooth 2-D Interface

We simulated the advection of a smooth, 2-D, two-material interface on $(x, y) \in [-1, 1] \times [-1, 1]$ with periodic boundaries, upon which we impose the initial condition:

$$\begin{bmatrix} \rho_1 \\ \rho_2 \\ \vec{u} \\ p_k \\ \alpha_1 \\ \alpha_2 \end{bmatrix} = \begin{bmatrix} 1.0 \\ 0.1 \\ [1.0, 1.0] \\ 1.0 \\ \frac{1}{2}\Big[(1.0 - 2\alpha_{\text{trace}})\cos(\pi x)\cos(\pi y) + 1.0\Big] \\ 1.0 - \alpha_1 \end{bmatrix}. \tag{7.5}$$

As before, both material equations of state are described analytically by the ideal gas law, with $\gamma_1 = 1.4$ and $\gamma_2 = 2.0$. This problem was run for a simulated time of $t = 2.0$, corresponding to one period of advection.

The errors using the Pandare discretization, shown in Fig. 7-9, converge optimally for the state variables, but the discretization is not well-balanced. For the path-conservative discretization, the results in Fig. 7-10 demonstrate optimal convergence and that the discretization is well-balanced. Similarly, using the spatial-averaging discretization, the errors depicted in Fig. 7-11 converge optimally and the discretization is well-balanced. These results are consistent with the results of Section 7.2.

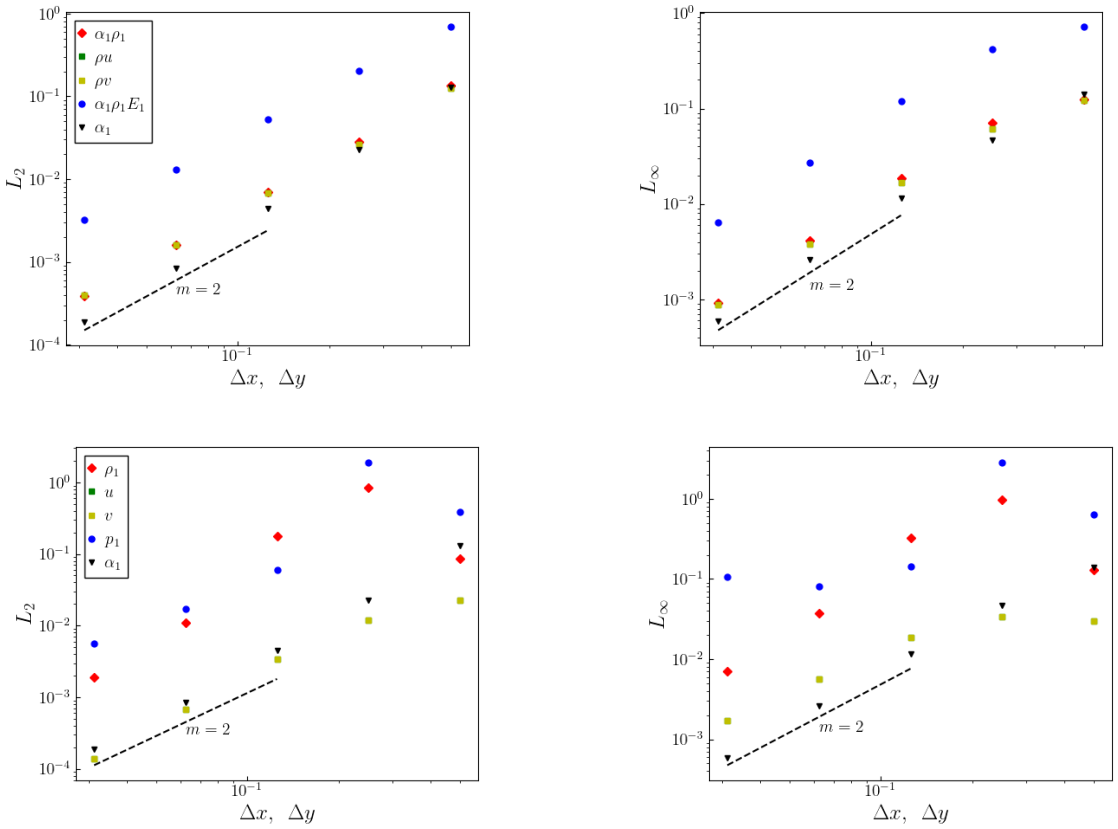

Figure 7-9. Errors in the state variables (top row) and primitive variables (bottom row) for the smooth 2-D interface advection problem after 1 period using the Pandare discretization (Section 3.2). The slopes m of the dashed lines are labeled in each figure.

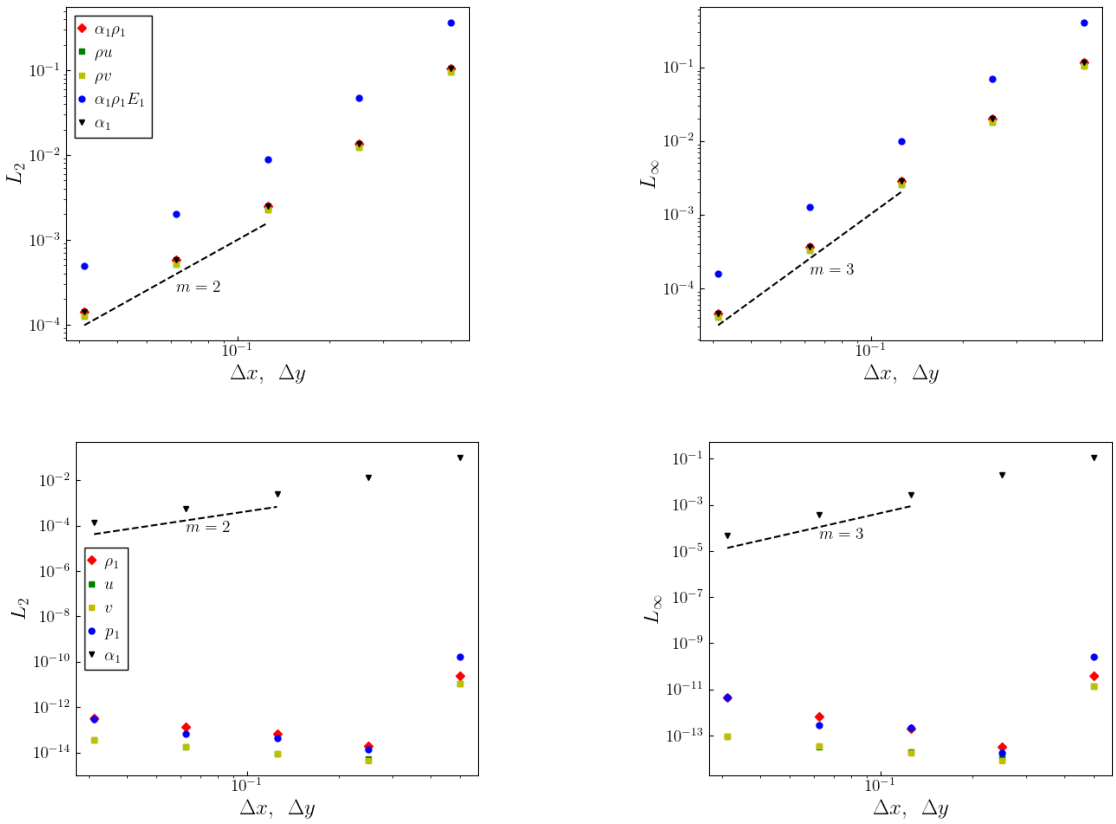

Figure 7-10. Errors in the state variables (top row) and primitive variables (bottom row) for the smooth 2-D interface advection problem after 1 period using the path-conservative discretization (Section 3.3). The slopes m of the dashed lines are labeled in each figure.

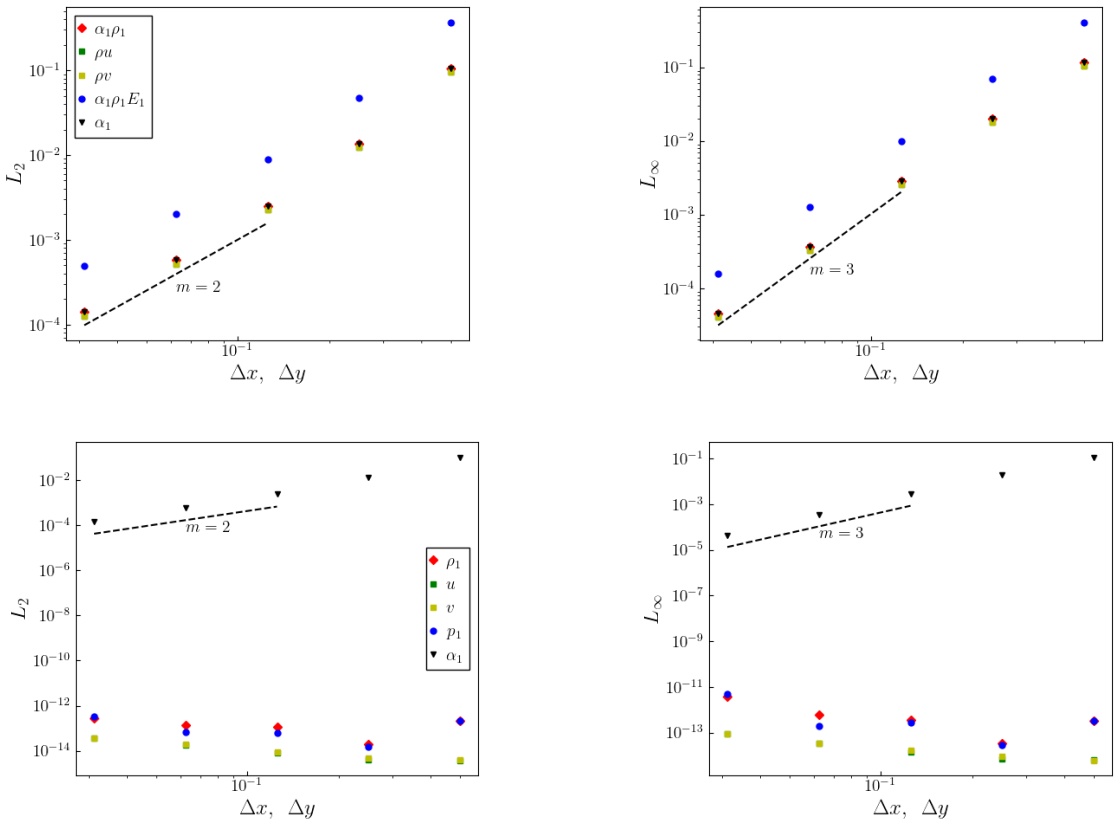

Figure 7-11. Errors in the state variables (top row) and primitive variables (bottom row) for the smooth 2-D interface advection problem after 1 period using the spatial-averaging discretization (Section 3.4). The slopes m of the dashed lines are labeled in each figure.

7.4. Advection of Sharp 1-D Single-Density Interface

We simulated the advection of a sharp, 1-D, two-material interface on $x \in [-1, 1]$ with $N_e = 64$ elements and periodic boundaries, upon which we impose the initial condition:

$$\begin{bmatrix} \rho_k \\ u \\ p_k \\ \alpha_1 \\ \alpha_2 \end{bmatrix} = \begin{bmatrix} 1.0 \\ 1.0 \\ 1.0 \\ 1.0 - \alpha_{\text{trace}} \\ \alpha_{\text{trace}} \end{bmatrix}, \quad \text{for } |x| > 0.5, \qquad \begin{bmatrix} \rho_k \\ u \\ p_k \\ \alpha_1 \\ \alpha_2 \end{bmatrix} = \begin{bmatrix} 1.0 \\ 1.0 \\ 1.0 \\ \alpha_{\text{trace}} \\ 1.0 - \alpha_{\text{trace}} \end{bmatrix}, \quad \text{for } |x| < 0.5. \tag{7.6}$$

For this problem, both material equations of state are described analytically by the ideal gas law, with $\gamma_1 = 1.4$ and $\gamma_2 = 2.0$. This problem was run for a simulated time of $t = 2.0$, corresponding to one period of advection. As this problem advects a discontinuity, we use the solution limiting procedure described in Chapter 4. This scheme is designed to not introduce errors in the variables that should remain uniform for a well-balanced discretization. This problem does not require any bounds preservation.

Profiles using the Pandare discretization of Section 3.2 are depicted in Fig. 7-12. The pressure errors and density errors are of order $O(10^{-8})$, and the velocity errors are of order $O(10^{-9})$. For the path-conservative discretization of Section 3.3, profiles are depicted in Fig. 7-13. The pressure errors are of order $O(10^{-13})$. The density errors of order $O(10^{-14})$, and the velocity errors are of order $O(10^{-14})$. Profiles using the spatial-averaging discretization of Section 3.4 are depicted in Fig. 7-14. The pressure errors are of order $O(10^{-13})$. The density errors are of order $O(10^{-14})$, and the velocity errors are of order $O(10^{-14})$. These results demonstrate that the Pandare discretization is not well balanced, whereas the path-conservative and spatial-averaging discretizations are well-balanced. Furthermore, these results show that the limiting scheme of Chapter 4 preserves the equilibria conditions expected for an isolated interface.

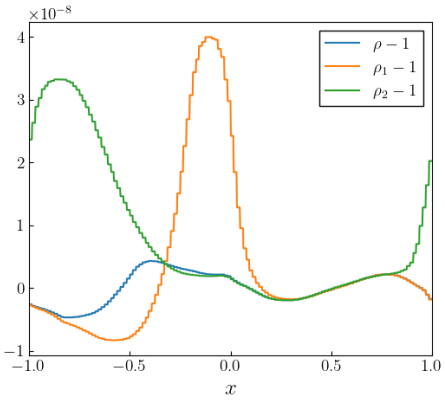

(a) Density error

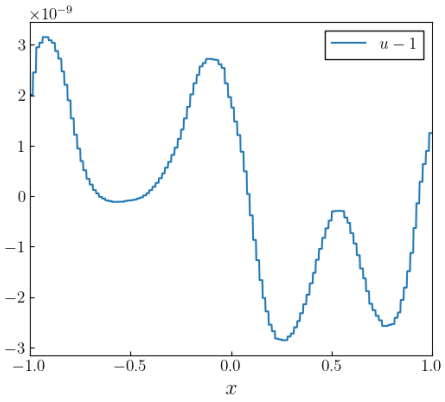

(b) Velocity error

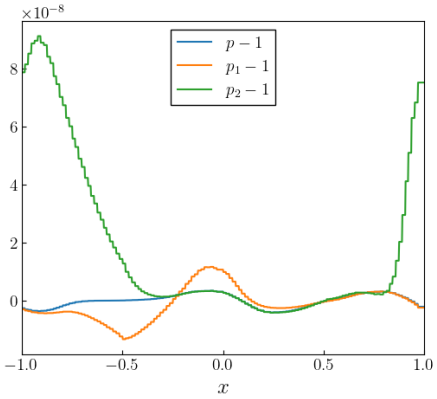

(c) Pressure error

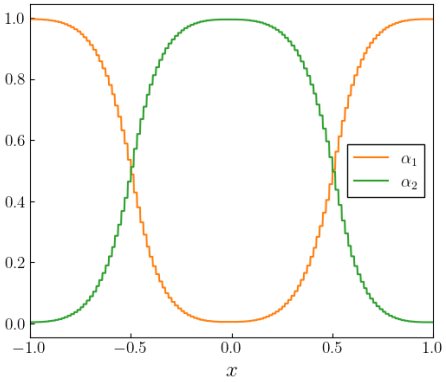

(d) Volume fraction

Figure 7-12. Primitive variable error profiles (a) - (c) and profiles (d) for the sharp 1-D single-density interface advection problem after 1 period using the Pandare discretization (Section 3.2).

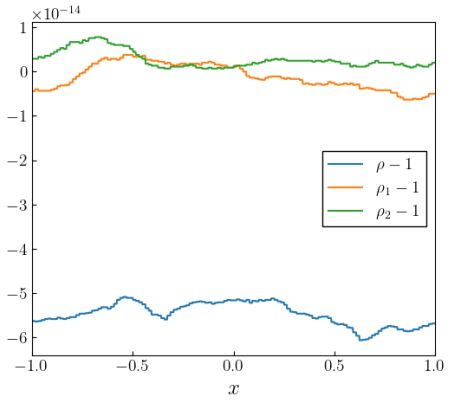

(a) Density error

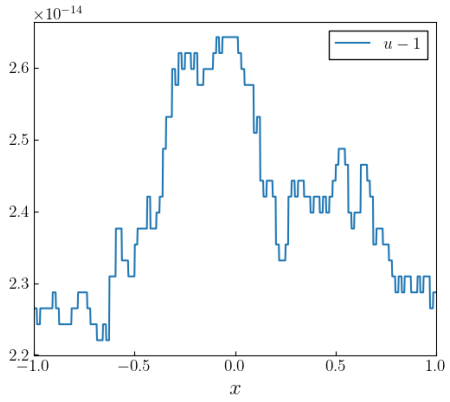

(b) Velocity error

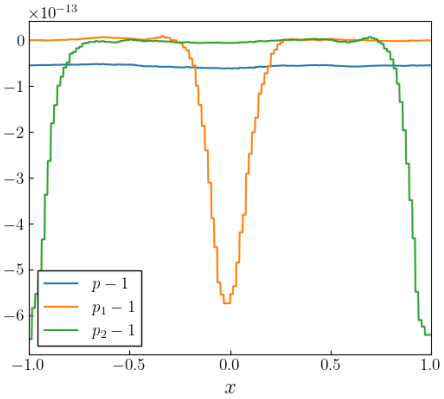

(c) Pressure error

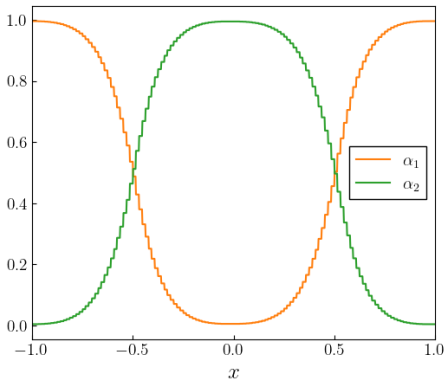

(d) Volume fraction

Figure 7-13. Primitive variable error profiles (a) - (c) and profiles (d) for the sharp 1-D single-density interface advection problem after 1 period using the path-conservative discretization (Section 3.3).

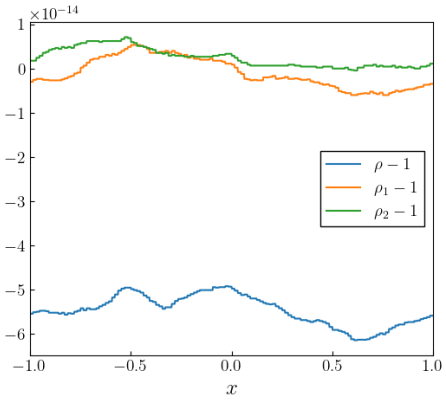

(a) Density error

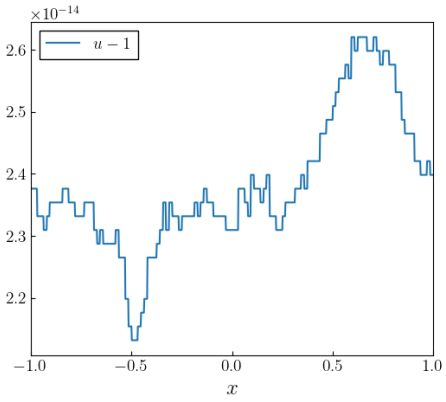

(b) Velocity error

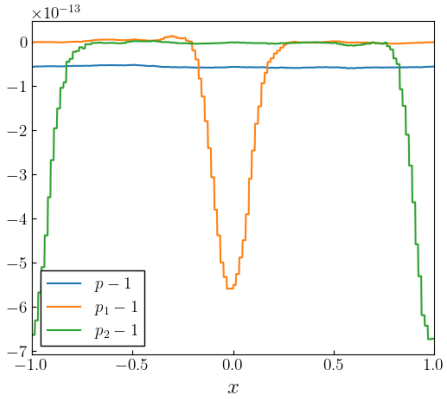

(c) Pressure error

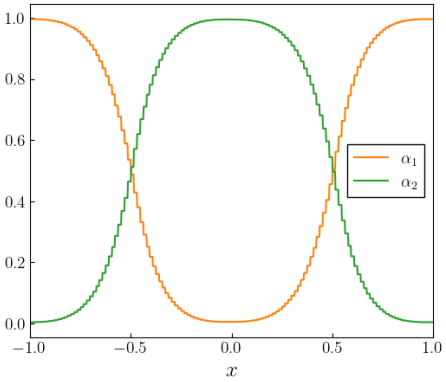

(d) Volume fraction

Figure 7-14. Primitive variable error profiles (a) - (c) and profiles (d) for the sharp 1-D single-density interface advection problem after 1 period using the spatial-averaging discretization (Section 3.4).

7.5. Advection of Sharp 1-D Interface - Configuration 1

We simulated the advection of a sharp, 1-D, two-material interface on $x \in [-1, 1]$ with $N_e = 64$ elements and with periodic boundaries, upon which we impose the initial condition:

$$\begin{bmatrix} \rho_k \\ u \\ p_k \\ \alpha_1 \\ \alpha_2 \end{bmatrix} = \begin{bmatrix} 1.0 \\ 1.0 \\ 1.0 \\ 1.0 - \alpha_{\text{trace}} \\ \alpha_{\text{trace}} \end{bmatrix}, \quad \text{for } |x| > 0.5, \qquad \begin{bmatrix} \rho_k \\ u \\ p_k \\ \alpha_1 \\ \alpha_2 \end{bmatrix} = \begin{bmatrix} 0.1 \\ 1.0 \\ 1.0 \\ \alpha_{\text{trace}} \\ 1.0 - \alpha_{\text{trace}} \end{bmatrix}, \quad \text{for } |x| < 0.5. \tag{7.7}$$

For this problem, both material equations of state are described analytically by the ideal gas law, with $\gamma_1 = 1.4$ and $\gamma_2 = 2.0$. This problem was run for a simulated time of $t = 2.0$, corresponding to one period of advection. For this problem, as in Section 7.4, we use the solution limiting procedure described in Chapter 4, as well as the volume fraction bounds preservation routine described in Section 5.1. In this configuration of the 1-D sharp interface, both material densities ρ_k are initialized as discontinuous.

Profiles using the Pandare discretization of Section 3.2 are depicted in Fig. 7-15. The pressure errors are of order $O(10^{-5})$, and the velocity errors are of order $O(10^{-6})$. These results demonstrate that, consistent with the results of prior sections, the Pandare discretization is not well-balanced.

For the path-conservative discretization of Section 3.3, profiles are depicted in Fig. 7-16. The pressure errors are of order $O(10^{-5})$, and the velocity errors are of order $O(10^{-6})$. Profiles using the spatial-averaging discretization of Section 3.4 are depicted in Fig. 7-17. The pressure errors are of order $O(10^{-5})$, and the velocity errors are of order $O(10^{-6})$.

These results are surprising in that the pressure and velocity errors for the path-conservative and spatial-averaging discretizations are no lower than those for the Pandare discretization shown in Fig. 7-15, while the results of Section 7.4 showed much lower errors in these quantities for the path-conservative and spatial-averaging discretizations. As will be seen in the following section, this is due to the density initialization and not the discretizations themselves.

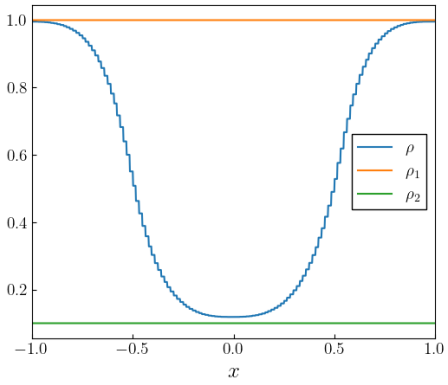

(a) Density

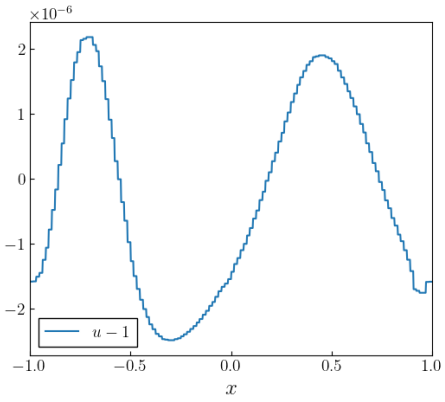

(b) Velocity error

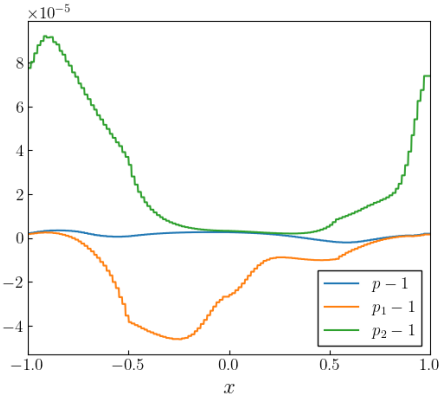

(c) Pressure error

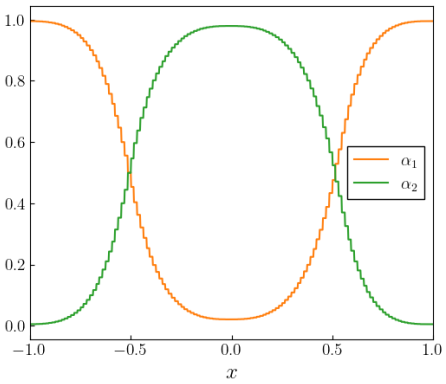

(d) Volume fraction

Figure 7-15. Primitive variable error profiles (b) and (c) and profiles (a) and (d) for the sharp 1-D interface advection problem (Config. 1) after 1 period using the Pandare discretization (Section 3.2).

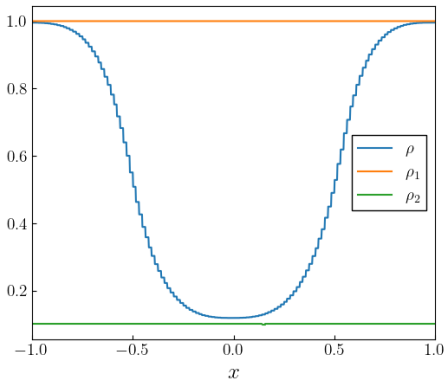

(a) Density

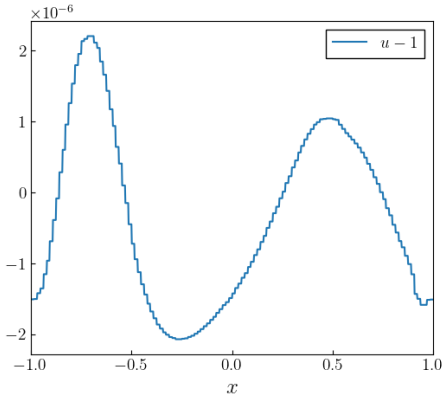

(b) Velocity error

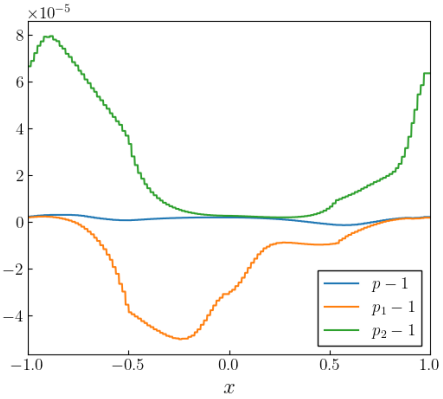

(c) Pressure error

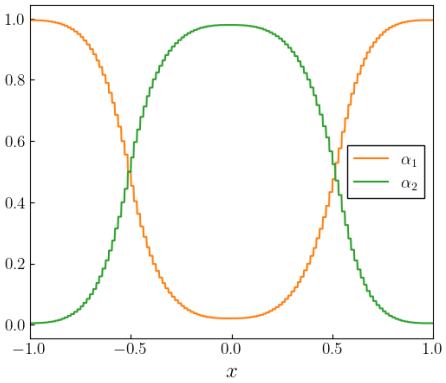

(d) Volume fraction

Figure 7-16. Primitive variable error profiles (b) and (c) and profiles (a) and (d) for the sharp 1-D interface advection problem (Config. 1) after 1 period using the path-conservative discretization (Section 3.3).

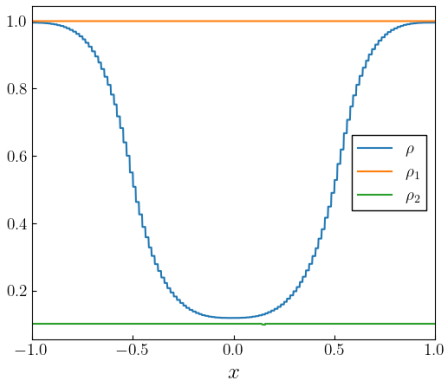

(a) Density

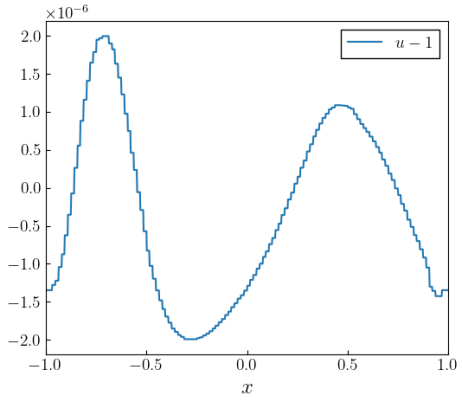

(b) Velocity error

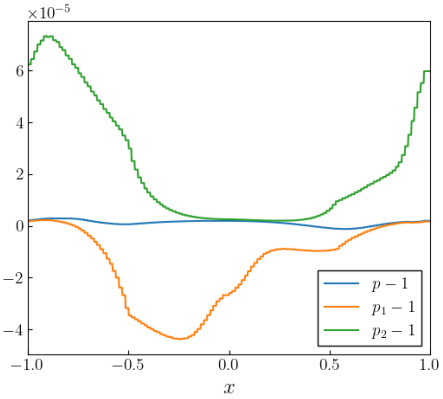

(c) Pressure error

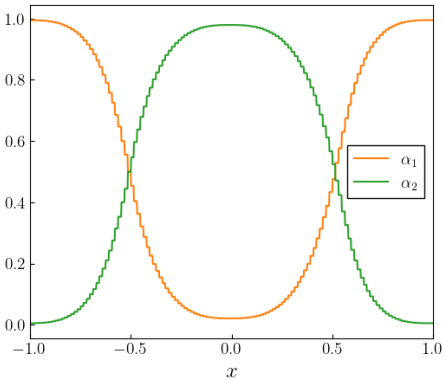

(d) Volume fraction

Figure 7-17. Primitive variable error profiles (b) and (c) and profiles (a) and (d) for the sharp 1-D interface advection problem (Config. 1) after 1 period using the spatial-averaging discretization (Section 3.4).

7.6. Advection of Sharp 1-D Interface - Configuration 2

We simulated the advection of a sharp, 1-D, two-material interface on $x \in [-1, 1]$ with $N_e = 64$ elements and periodic boundaries, upon which we impose the initial condition:

$$\begin{bmatrix} \rho_1 \\ \rho_2 \\ u \\ p_k \\ \alpha_1 \\ \alpha_2 \end{bmatrix} = \begin{bmatrix} 1.0 \\ 0.1 \\ 1.0 \\ 1.0 \\ 1.0 - \alpha_{\text{trace}} \\ \alpha_{\text{trace}} \end{bmatrix}, \quad \text{for } |x| > 0.5, \qquad \begin{bmatrix} \rho_1 \\ \rho_2 \\ u \\ p_k \\ \alpha_1 \\ \alpha_2 \end{bmatrix} = \begin{bmatrix} 1.0 \\ 0.1 \\ 1.0 \\ 1.0 \\ \alpha_{\text{trace}} \\ 1.0 - \alpha_{\text{trace}} \end{bmatrix}, \quad \text{for } |x| < 0.5. \tag{7.8}$$

For this problem, both material equations of state are described analytically by the ideal gas law, with $\gamma_1 = 1.4$ and $\gamma_2 = 2.0$. This problem was run for a simulated time of $t = 2.0$, corresponding to one period of advection. For this problem, as in Sections 7.4, and 7.5, we use the solution limiting procedure described in Chapter 4. In this configuration of the 1-D sharp interface, both material densities ρ_k are initialized as uniform, and the discontinuity in the bulk density is represented only by the discontinuity in volume fraction.

For the Pandare discretization of Section 3.2, profiles are depicted in Fig. 7-18. The pressure errors are significantly smaller than in Section 7.5, with Config. 1, on the order of $O(10^{-10})$. The velocity errors are on the order of $O(10^{-11})$. For the path-conservative discretization of Section 3.3, profiles are depicted in Fig. 7-19. Here too, pressure errors are significantly smaller than in Section 7.5, with Config. 1, on the order of $O(10^{-13})$. The velocity errors are on the order of $O(10^{-15})$. These errors are also considerably smaller than with the Pandare discretization. For the spatial-averaging discretization of Section 3.4, profiles are depicted in Fig. 7-20. Here too, pressure errors are significantly smaller than in Section 7.5, with Config. 1, on the order of $O(10^{-13})$. The velocity errors are on the order of $O(10^{-15})$. These errors are also considerably smaller than with the Pandare discretization.

The results of this section compared to Section 7.5 show that when initializing an interface or other discontinuity, it is best to carry the non-uniformity in the volume fraction field α_k and to initialize the primitive material-indexed quantities (e.g., ρ_k, p_k) uniformly if possible. In the case of an isolated interface, this approach significantly reduces the amount of error in quantities that should be error-free. Furthermore, this prevents the initialization of "trace" materials with states that are not sensible for that material.

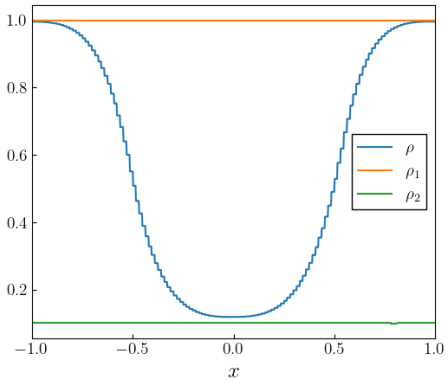

(a) Density

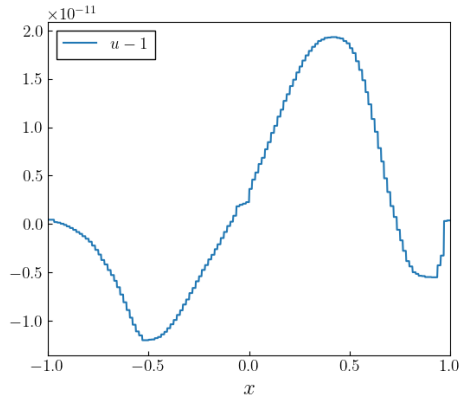

(b) Velocity error

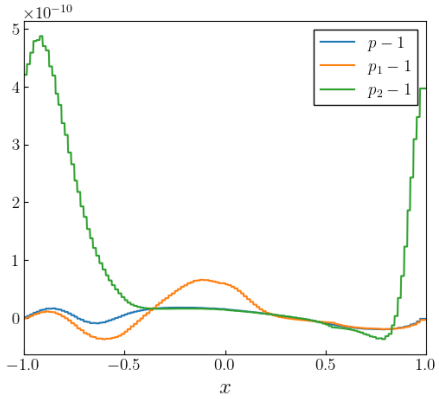

(c) Pressure error

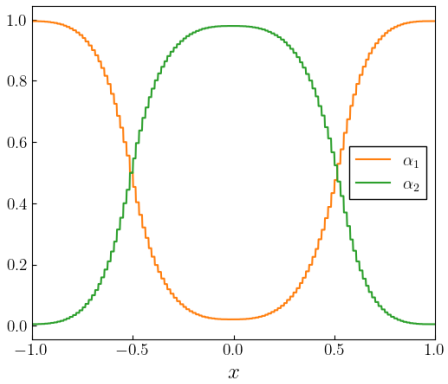

(d) Volume fraction

Figure 7-18. Primitive variable error profiles (b) and (c) and profiles (a) and (d) for the sharp 1-D interface advection problem (Config. 2) after 1 period using the Pandare discretization (Section 3.2).

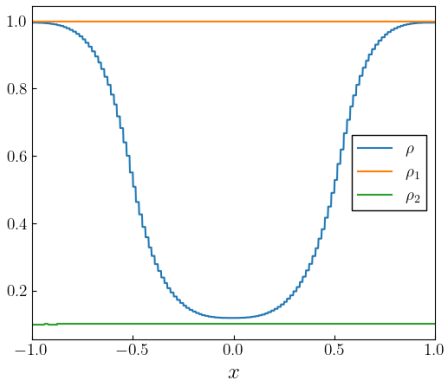

(a) Density

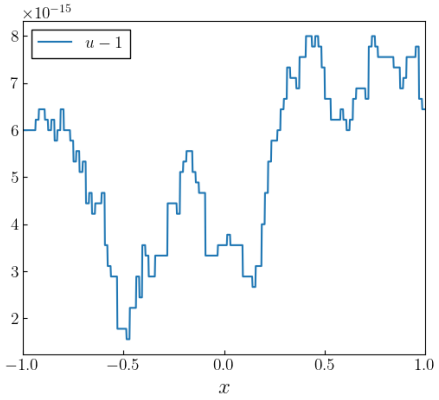

(b) Velocity error

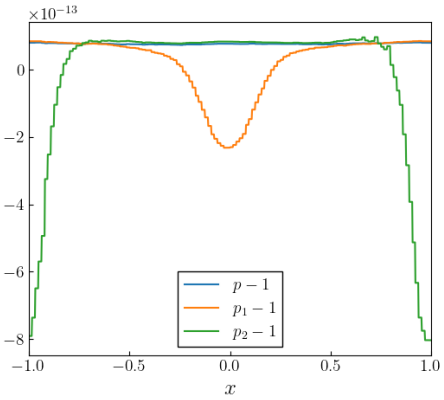

(c) Pressure error

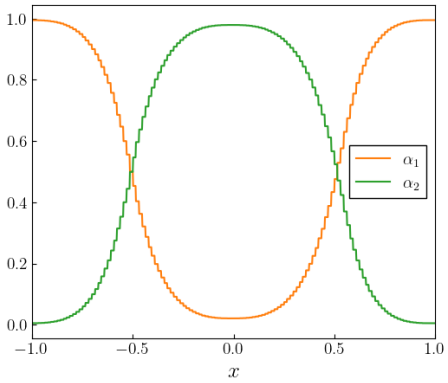

(d) Volume fraction

Figure 7-19. Primitive variable error profiles (b) and (c) and profiles (a) and (d) for the sharp 1-D interface advection problem (Config. 2) after 1 period using the path-conservative discretization (Section 3.3).

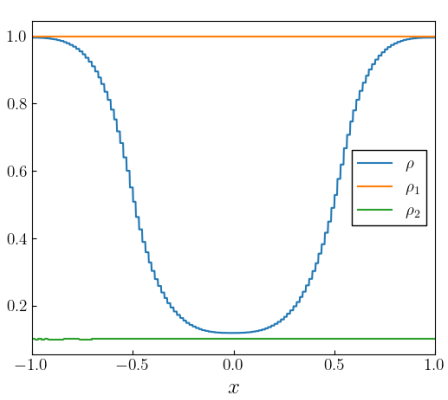

(a) Density

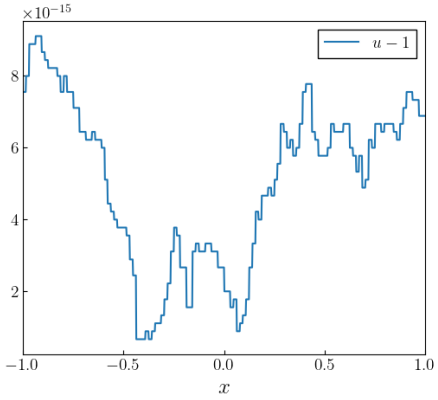

(b) Velocity error

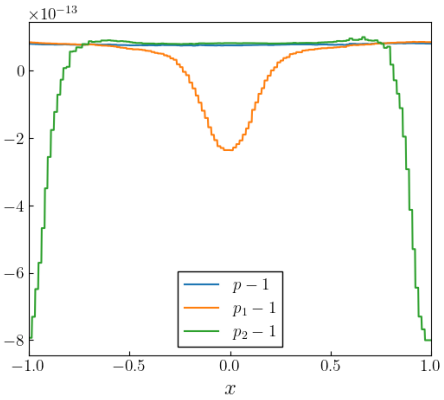

(c) Pressure error

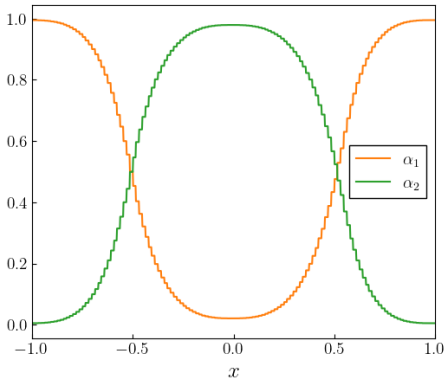

(d) Volume fraction

Figure 7-20. Primitive variable error profiles (b) and (c) and profiles (a) and (d) for the sharp 1-D interface advection problem (Config. 2) after 1 period using the spatial-averaging discretization (Section 3.4).

7.7. Advection of Sharp 2-D Interface

We simulated the advection of a sharp, 2-D, two-material interface on $(x, y) \in [-1, 1] \times [-1, 1]$ with $N_e = 64 \times 64$ elements and periodic boundaries, upon which we impose the initial condition:

$$\begin{bmatrix} \rho_1 \\ \rho_2 \\ \vec{u} \\ p_k \\ \alpha_1 \\ \alpha_2 \end{bmatrix} = \begin{bmatrix} 1.0 \\ 0.1 \\ [1.0, 1.0] \\ 1.0 \\ 1.0 - \alpha_{\text{trace}} \\ \alpha_{\text{trace}} \end{bmatrix}, \quad \text{for } r > 0.5, \qquad \begin{bmatrix} \rho_1 \\ \rho_2 \\ \vec{u} \\ p_k \\ \alpha_1 \\ \alpha_2 \end{bmatrix} = \begin{bmatrix} 1.0 \\ 0.1 \\ [1.0, 1.0] \\ 1.0 \\ \alpha_{\text{trace}} \\ 1.0 - \alpha_{\text{trace}} \end{bmatrix}, \quad \text{for } r < 0.5. \tag{7.9}$$

For this problem, both material equations of state are described analytically by the ideal gas law, with $\gamma_1 = 1.4$ and $\gamma_2 = 2.0$. This problem was run for a simulated time of $t = 2.0$, corresponding to one period of advection. For this problem, we use the solution limiting procedure described in Chapter 4. It was observed that volume fraction bounds preservation routine described in Section 5.1 is necessary to run this problem without crashes, with $\alpha_{\text{floor}} = 10^{-12}$. This problem is initialized in the manner of Section 7.6.

For the Pandare discretization of Section 3.2, profiles are depicted in Fig. 7-21. The pressure errors are on the order of $O(10^{-5})$. The velocity errors are on the order of $O(10^{-7})$. For the path-conservative discretization of Section 3.3, profiles are depicted in Fig. 7-22. The material pressure errors are on the order of $O(10^{-13})$. The velocity errors are on the order of $O(10^{-15})$. These errors are considerably smaller than with the Pandare discretization. For the spatial-averaging discretization of Section 3.4, profiles are depicted in Fig. 7-23. Here too, pressure errors are on the order of $O(10^{-13})$. The velocity errors are on the order of $O(10^{-14})$. These errors are also considerably smaller than with the Pandare discretization. The results of this section are similar to the results to the 1-D problem of Section 7.6, indicating that the path-conservative and spatial-averaging discretizations are well balanced for multi-dimensional problems. Furthermore, these results indicate that the solution limiting procedure described in Chapter 4 applies readily to multi-dimensional problems. As volume fraction bounds preservation is required for this problem, these results also demonstrate that the volume fraction bounds preservation scheme in Section 5.1 does not affect equilibria of the primitive variables in the case of an isolated interface.

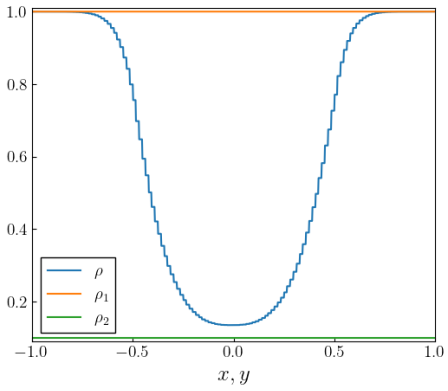

(a) Density

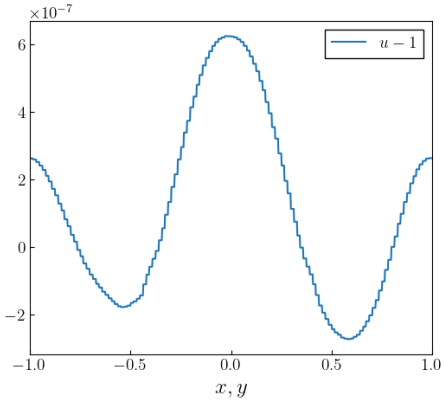

(b) Velocity error

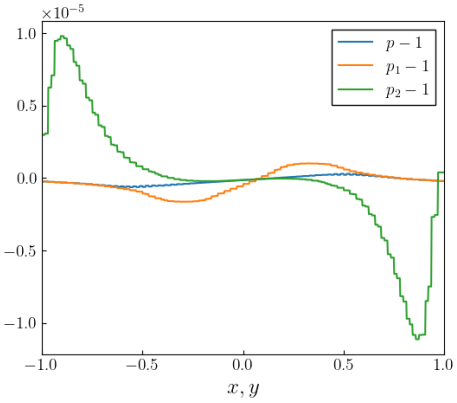

(c) Pressure error

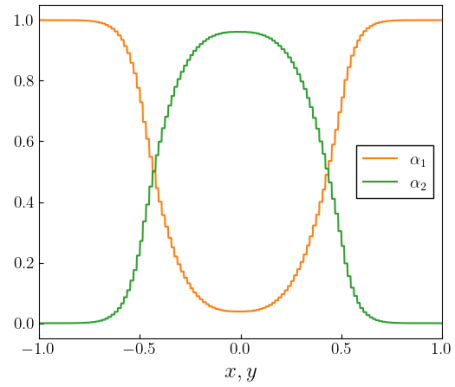

(d) Volume fraction

Figure 7-21. Primitive variable error profiles (b) and (c) and profiles (a) and (d) along the diagonal $x = y$ for the sharp 2-D interface advection problem after 1 period using the Pandare discretization (Section 3.2).

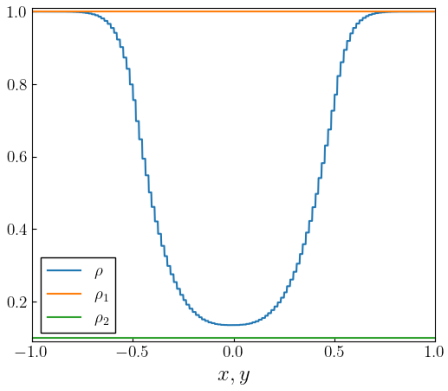

(a) Density

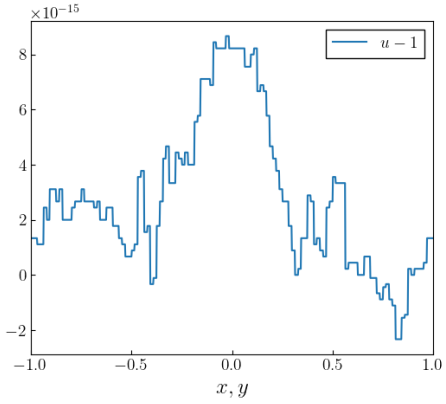

(b) Velocity error

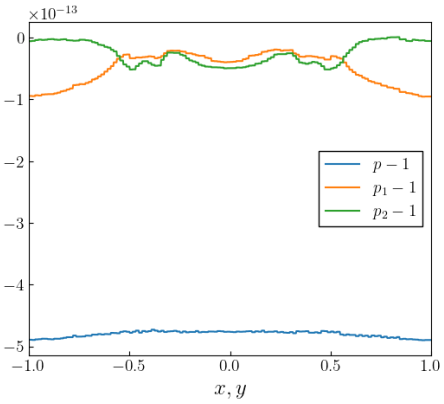

(c) Pressure error

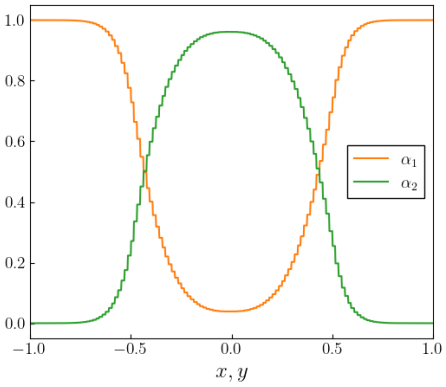

(d) Volume fraction

Figure 7-22. Primitive variable error profiles (b) and (c) and profiles (a) and (d) along the diagonal $x = y$ for the sharp 2-D interface advection problem after 1 period using the path-conservative discretization (Section 3.3).

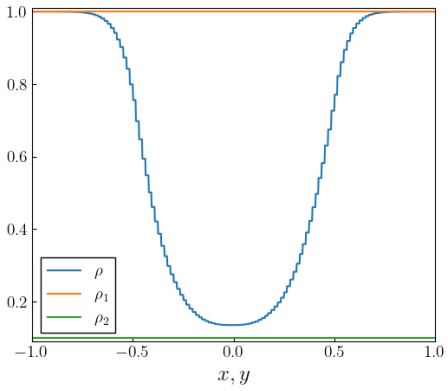

(a) Density

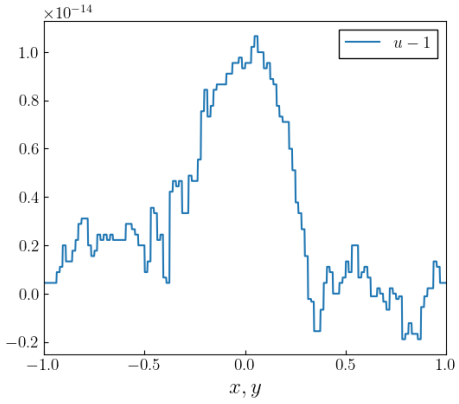

(b) Velocity error

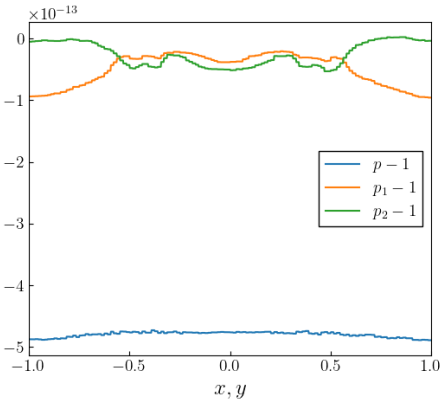

(c) Pressure error

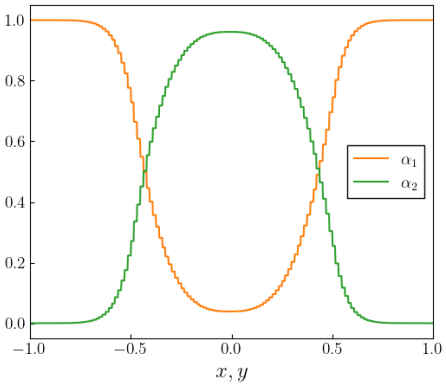

(d) Volume fraction

Figure 7-23. Primitive variable error profiles (b) and (c) and profiles (a) and (d) along the diagonal $x = y$ for the sharp 2-D interface advection problem after 1 period using the spatial-averaging discretization (Section 3.3).

7.8. 1-D Shock-Interface Interaction

We simulated the interaction of a strong (Mach 8.96) shockwave with a material interface [18] on $x \in [-1, 1]$ with $N_e = 256$ elements, upon which we impose the initial condition:

$$
\begin{aligned}
\begin{bmatrix} \rho_1 \\ \rho_2 \\ u \\ p_1 \\ p_2 \\ \alpha_1 \\ \alpha_2 \end{bmatrix} &= \begin{bmatrix} \rho_0 \frac{(\gamma_1+1)M_s^2}{(\gamma_1-1)M_s^2+2} \\ 1.0 \\ \frac{c_0}{M_s}\frac{2(M_s^2-1)}{\gamma_1+1} + u_c \\ r p_0 \\ p_0 \\ 1.0 - \alpha_{\text{trace}} \\ \alpha_{\text{trace}} \end{bmatrix}, \quad \text{for} \quad -1 < x < -0.8, \\
\begin{bmatrix} \rho_1 \\ \rho_2 \\ u \\ p_1 \\ p_2 \\ \alpha_1 \\ \alpha_2 \end{bmatrix} &= \begin{bmatrix} 0.1 \\ 1.0 \\ u_c \\ p_0 \\ p_0 \\ 1.0 - \alpha_{\text{trace}} \\ \alpha_{\text{trace}} \end{bmatrix}, \quad \text{for} \quad -0.8 < x < -0.2, \\
\begin{bmatrix} \rho_1 \\ \rho_2 \\ u \\ p_1 \\ p_2 \\ \alpha_1 \\ \alpha_2 \end{bmatrix} &= \begin{bmatrix} 0.1 \\ 1.0 \\ u_c \\ p_0 \\ p_0 \\ \alpha_{\text{trace}} \\ 1.0 - \alpha_{\text{trace}} \end{bmatrix}, \quad \text{for} \quad -0.2 < x < 1,
\end{aligned}
\tag{7.10}
$$

where $M_s = 8.96$, the 0 subscript denotes pre-shock quantities with $p_0 = 1.0$, the background velocity is $u_c = -2$, and $r = 100$. Both material equations of state are described analytically by the ideal gas law, with $\gamma_1 = 5/3$ and $\gamma_2 = 1.4$. This problem was run for a simulated time of $t = 0.04$. For this problem, we use the solution limiting procedure described in Chapter 4. We do not use bounds preservation. We show results for the different pressure equilibration/relaxation approaches of Chapter 6. For comparison, we use a reference solution generated with 2000 elements.

Figures 7-24 - 7-26 depict the 1-D shock-interface problem at an early time, before the shock has impacted the interface. The pressures immediately behind the shock front are out of equilibrium, appearing nearly identical for all of our discretizations. Specifically, the pressure of the material that is present in trace quantities, p_2, is far from the bulk pressure p. In general, this is the case with the six-equation model in Eqns. (2.1): the bulk quantities are well-behaved and accurate, while the trace quantities may not be, even when the discretization used is well balanced. Additionally, for the Pandare discretization, there are pressure errors due to the interface near $x = -0.2$. For the well-balanced discretizations, as expected, these pressure errors are not present.

Figures 7-27 - 7-29 show the 1-D shock-interface problem after the interaction. These figures show how extreme the unphysical material pressure p_k can become when the pressure relaxation

terms in Eqns. (2.1) are untreated. This effect is particularly pronounced in problems where waves interact with interfaces, and where waves and interfaces are born from the same discontinuity (i.e., Riemann problems). This highlights the importance of the pressure equilibration/relaxation approaches described in Chapter 6. Figure 7-30 shows the 1-D shock-interface problem after the interaction using the total equilibration algorithm of Section 6.1. The pressures are equilibrated throughout the domain. Figure 7-30 shows the 1-D shock-interface problem after the interaction using the partial equilibration algorithm of Section 6.1 together with the instantaneous pressure algorithm of Section 6.2. The pressures are equilibrated throughout the domain. Note that this problem crashes with the instantaneous pressure relaxation algorithm alone: the partial equilibration algorithm provides an improved initial state for the instantaneous pressure relaxation algorithm and improves its robustness.

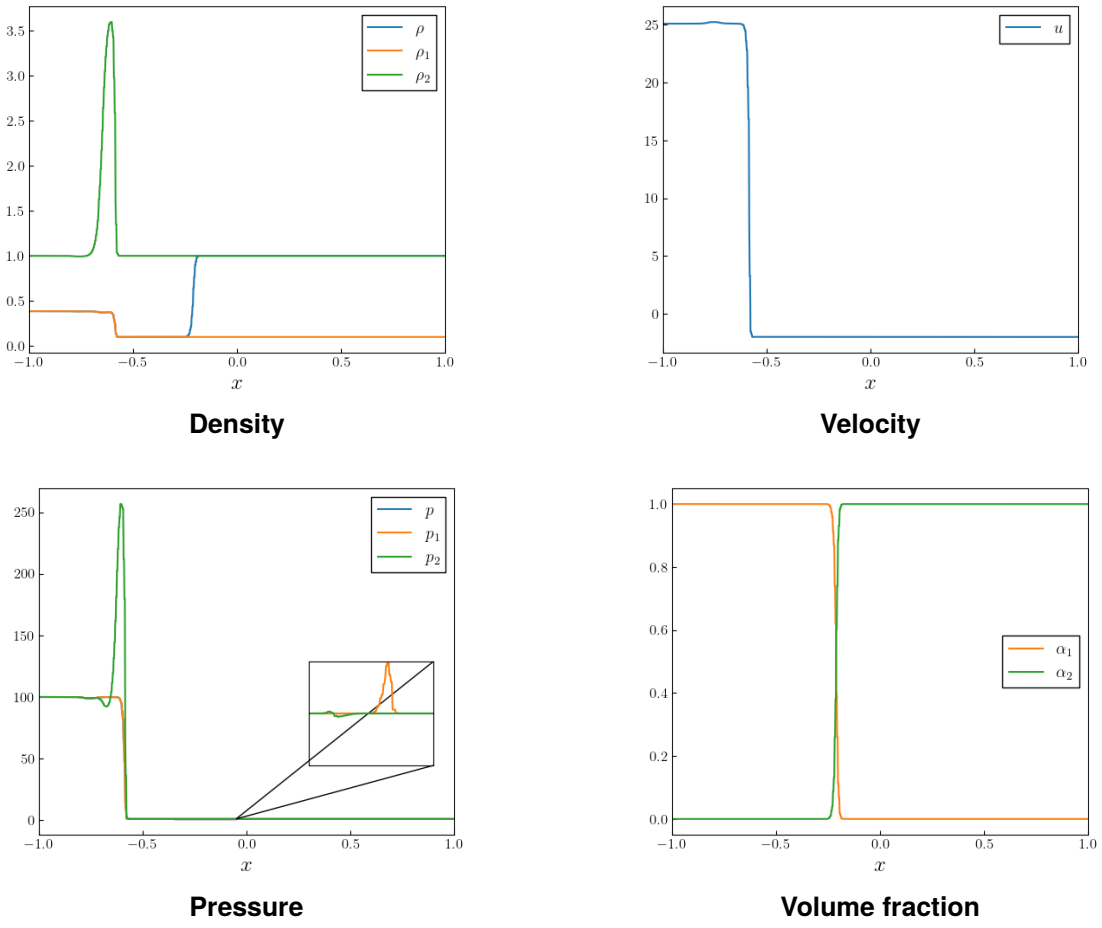

Figure 7-24. Primitive variable profiles for the 1-D shock-interface problem at $t = 0.01$ using the Pandare discretization (Section 3.2). No pressure equilibration/relaxation.

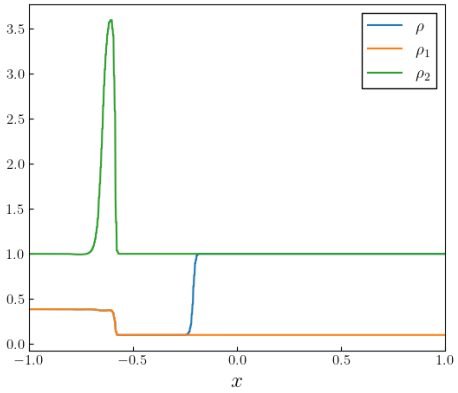

Density

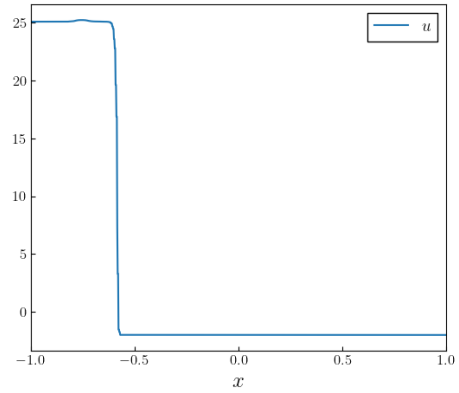

Velocity

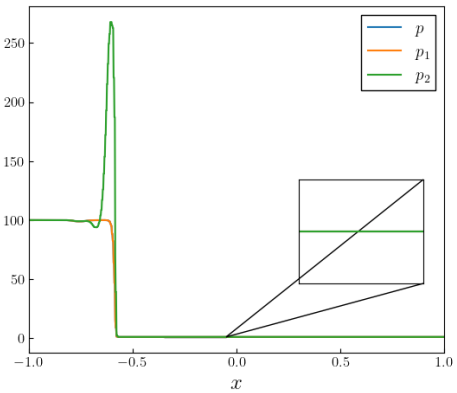

Pressure

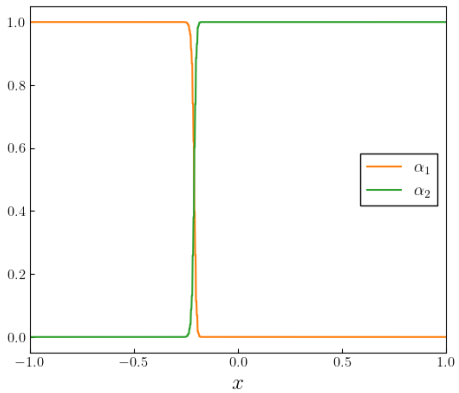

Volume fraction

Figure 7-25. Primitive variable profiles for the 1-D shock-interface problem at $t = 0.01$ using the path-conservative discretization (Section 3.3). No pressure equilibration/relaxation.

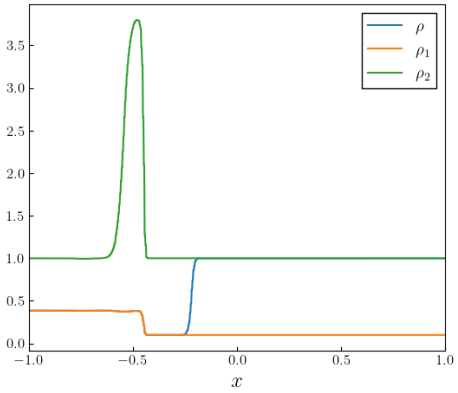

Density

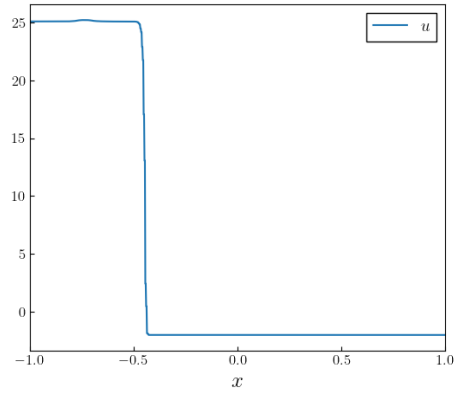

Velocity

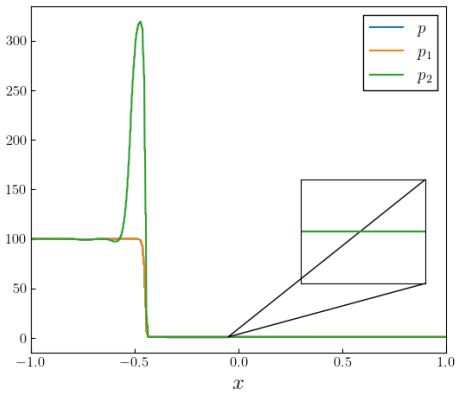

Pressure

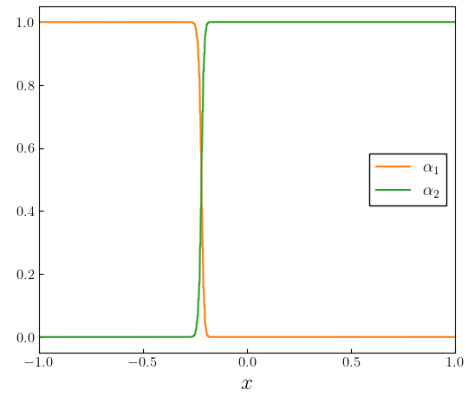

Volume fraction

Figure 7-26. Primitive variable profiles for the 1-D shock-interface problem at $t = 0.01$ using the spatial-averaging discretization (Section 3.3). No pressure equilibration/relaxation.

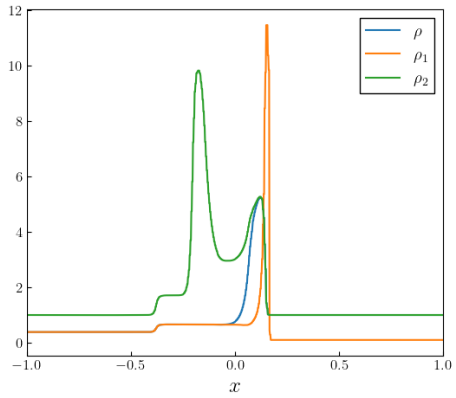

Density

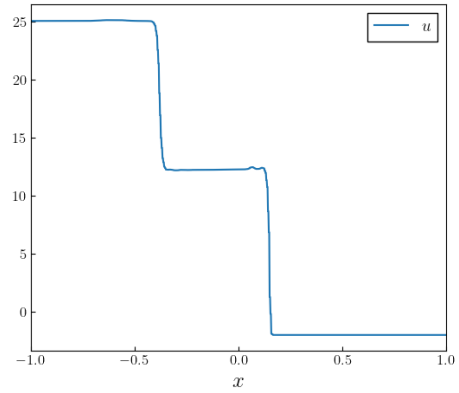

Velocity

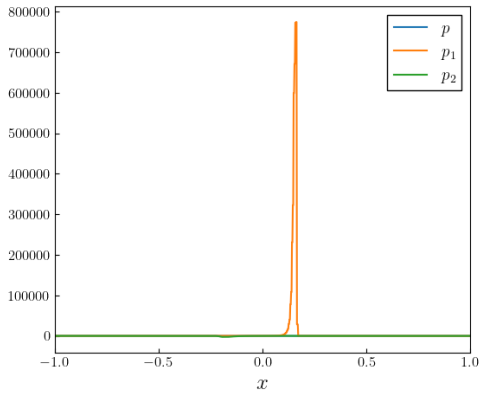

Pressure

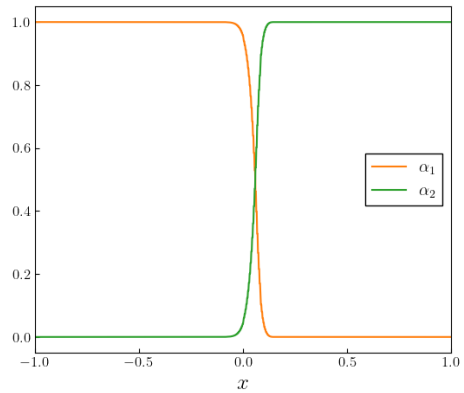

Volume fraction

Figure 7-27. Primitive variable profiles for the 1-D shock-interface problem at $t = 0.04$ using the Pandare discretization (Section 3.2). No pressure equilibration/relaxation.

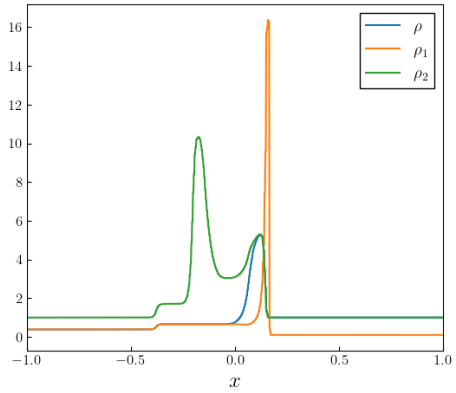

Density

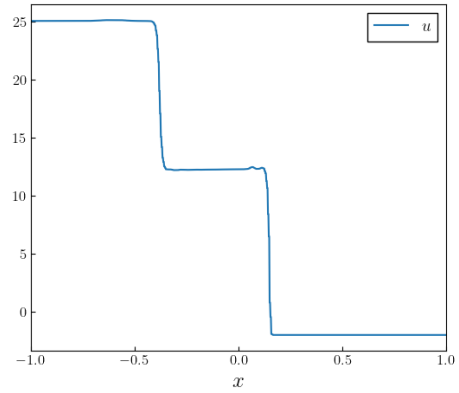

Velocity

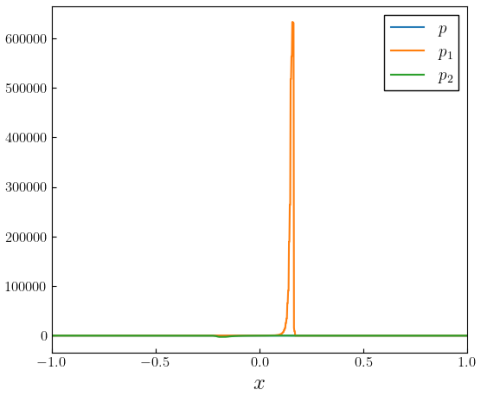

Pressure

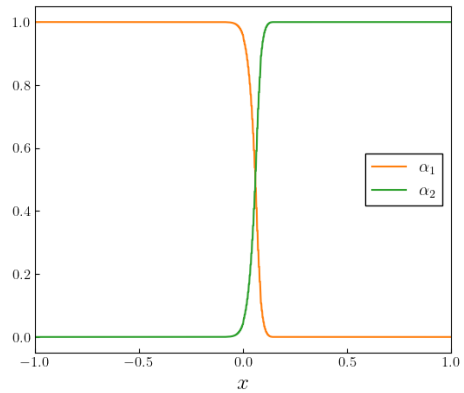

Volume fraction

Figure 7-28. Primitive variable profiles for the 1-D shock-interface problem at $t = 0.04$ using the path-conservative discretization (Section 3.3). No pressure equilibration/relaxation.

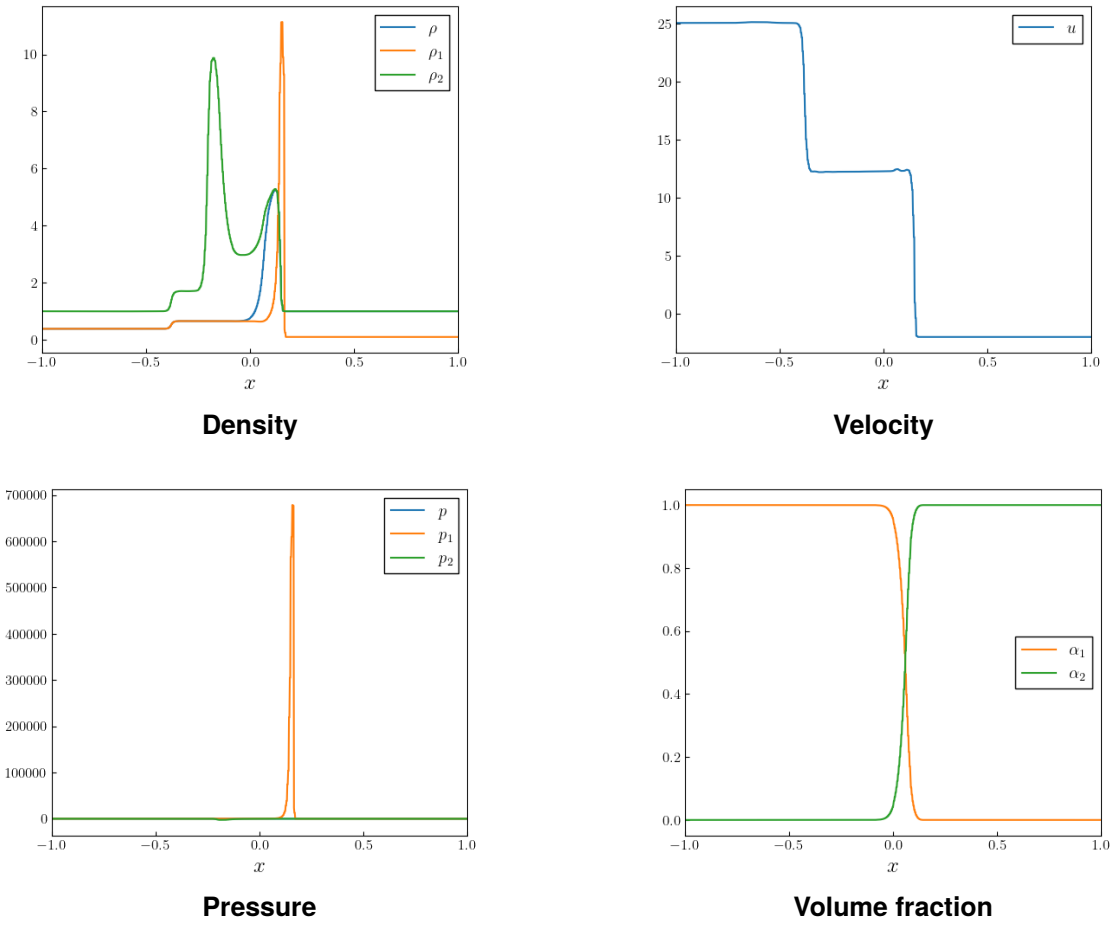

Figure 7-29. Primitive variable profiles for the 1-D shock-interface problem at $t = 0.04$ using the spatial-averaging discretization (Section 3.3). No pressure equilibration/relaxation.

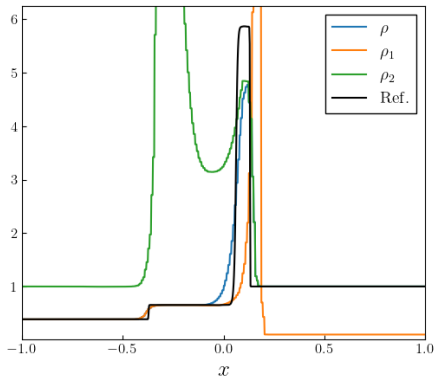

Density

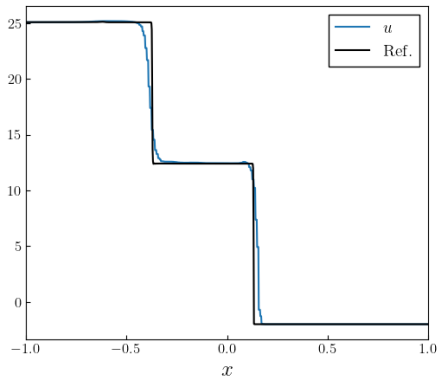

Velocity

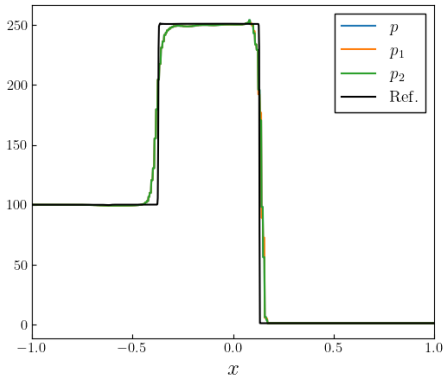

Pressure

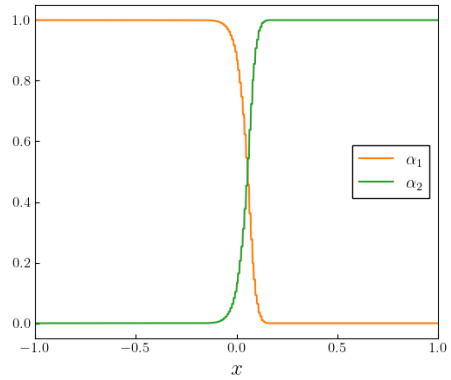

Volume fraction

Figure 7-30. Primitive variable profiles for the 1-D shock-interface problem at $t = 0.04$ using the spatial-averaging discretization (Section 3.3). Pressures are controlled with the total equilibration algorithm (Section 6.1).

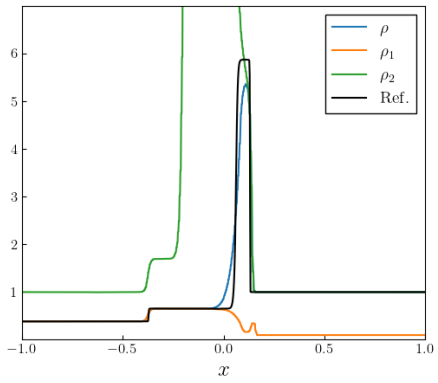

Density

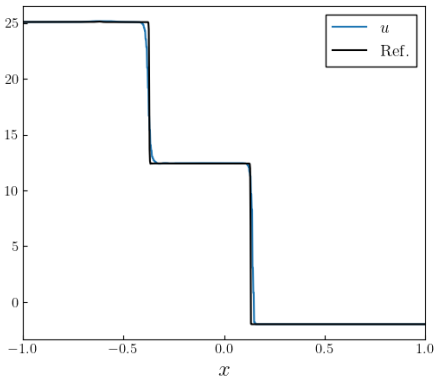

Velocity

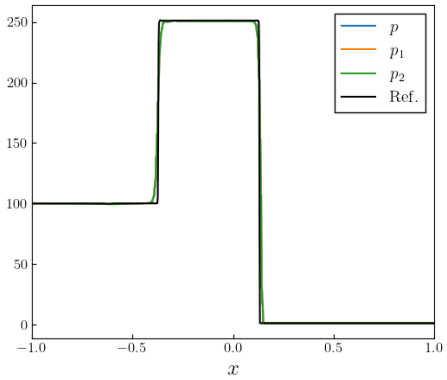

Pressure

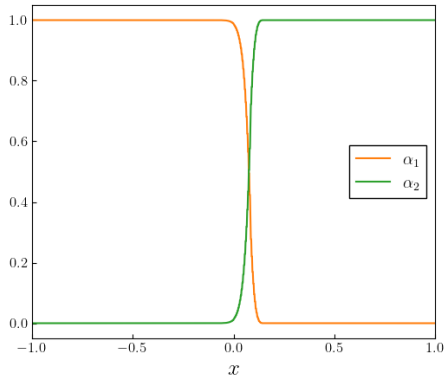

Volume fraction

Figure 7-31. Primitive variable profiles for the 1-D shock-interface problem at $t = 0.04$ using the spatial-averaging discretization (Section 3.3). Pressures are controlled with the partial equilibration (Section 6.1) and instantaneous pressure relaxation (Section 6.2) algorithms.

7.9. 1-D Multimaterial Sod

We simulated the 1-D multimaterial Sod problem on $x \in [0, 1]$ with $N_e = 256$ elements, upon which we impose the initial condition:

$$\begin{bmatrix} \rho_1 \\ \rho_2 \\ u \\ p_k \\ \alpha_1 \\ \alpha_2 \end{bmatrix} = \begin{bmatrix} 1.0 \\ 0.1 \\ 1.0 \\ 1.0 \\ 1.0 - \alpha_{\text{trace}} \\ \alpha_{\text{trace}} \end{bmatrix}, \quad \text{for } x > 0.5, \qquad \begin{bmatrix} \rho_1 \\ \rho_2 \\ u \\ p_k \\ \alpha_1 \\ \alpha_2 \end{bmatrix} = \begin{bmatrix} 1.0 \\ 0.1 \\ 1.0 \\ 1.0 \\ \alpha_{\text{trace}} \\ 1.0 - \alpha_{\text{trace}} \end{bmatrix}, \quad \text{for } x < 0.5. \tag{7.11}$$

Both material equations of state are described analytically by the ideal gas law, with $\gamma_1 = 2.0$ and $\gamma_2 = 1.4$. This problem was run for a simulated time of $t = 0.2$. For this problem, we use the solution limiting procedure described in Chapter 4. We use the volume fraction bounds preservation scheme described in Section 5.1 with $\alpha_{\text{floor}} = 10^{-12}$. For comparison, we use a reference solution generated with 2000 elements.

Figures 7-32 - 7-34 show the 1-D Sod problem after the wave structure has evolved. These figures show how extreme the unphysical material pressures p_k can become when the pressure relaxation terms in Eqns. (2.1) are untreated, highlighting the importance of the pressure equilibration/relaxation approaches described in Chapter 6. Figure 7-35 shows the 1-D Sod problem using the total equilibration algorithm of Section 6.1. The pressures are equilibrated throughout the domain. Figure 7-36 shows the 1-D Sod problem after the interaction using the partial equilibration algorithm of Section 6.1 together with the instantaneous pressure algorithm of Section 6.2. The pressures are equilibrated throughout the domain.

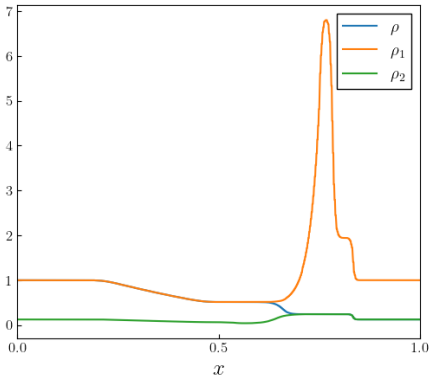

Density

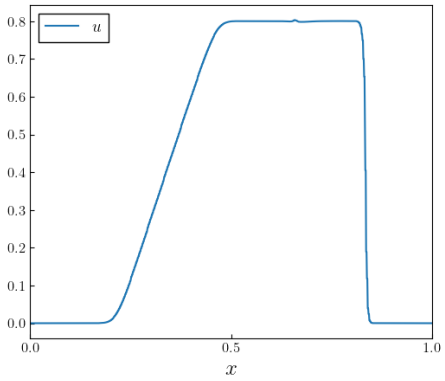

Velocity

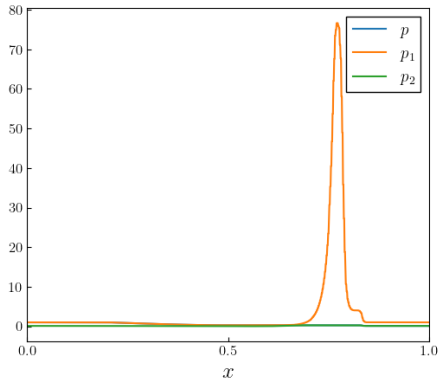

Pressure

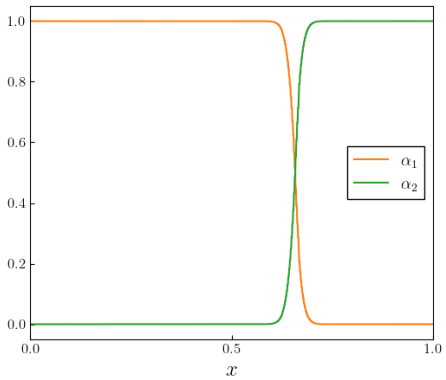

Volume fraction

Figure 7-32. Primitive variable profiles for the 1-D multimaterial Sod problem at $t = 0.2$ using the Pandare discretization (Section 3.2). No pressure equilibration/relaxation.

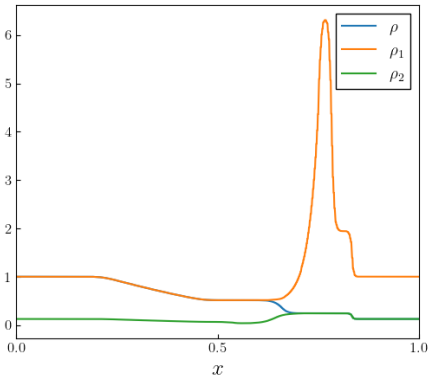

Density

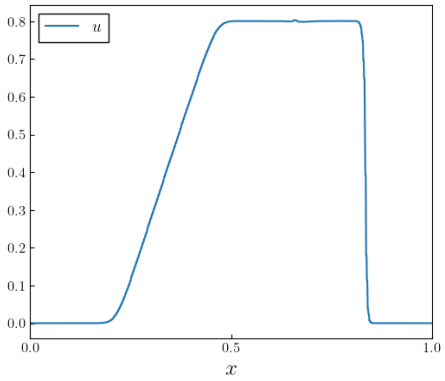

Velocity

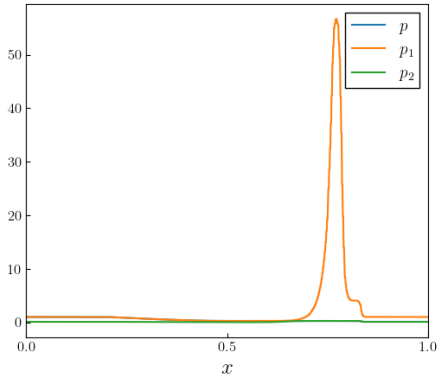

Pressure

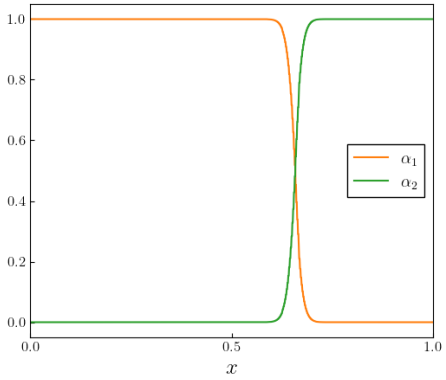

Volume fraction

Figure 7-33. Primitive variable profiles for the 1-D multimaterial Sod problem at $t = 0.2$ using the path-conservative discretization (Section 3.3). No pressure equilibration/relaxation.

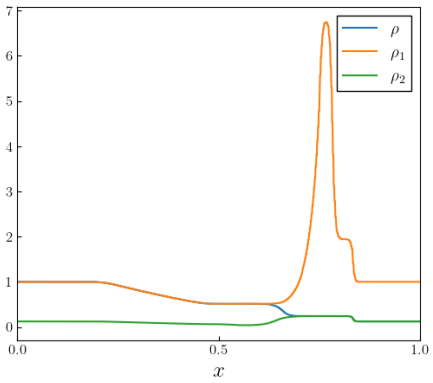

Density

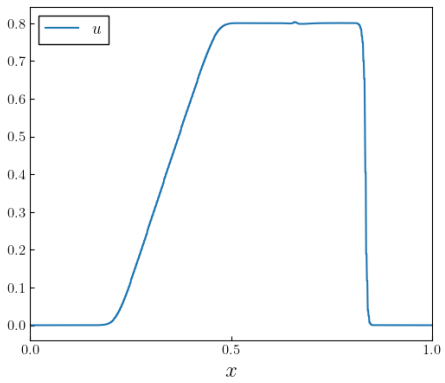

Velocity

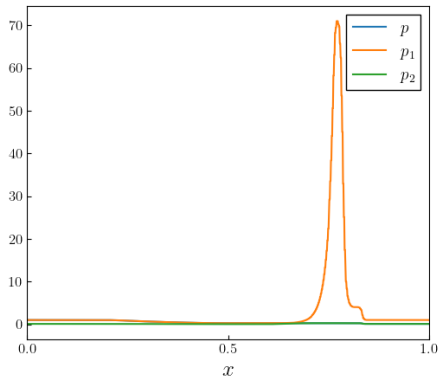

Pressure

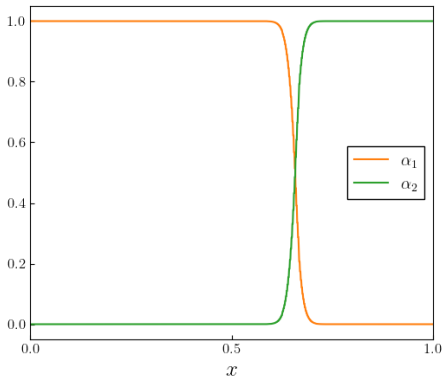

Volume fraction

Figure 7-34. Primitive variable profiles for the 1-D multimaterial Sod problem at $t = 0.2$ using the spatial-averaging discretization (Section 3.4). No pressure equilibration/relaxation.

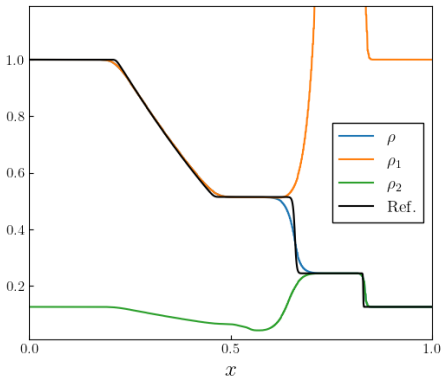

Density

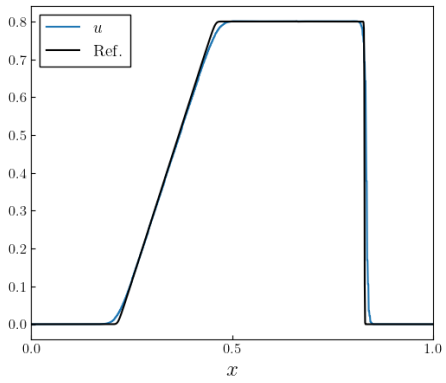

Velocity

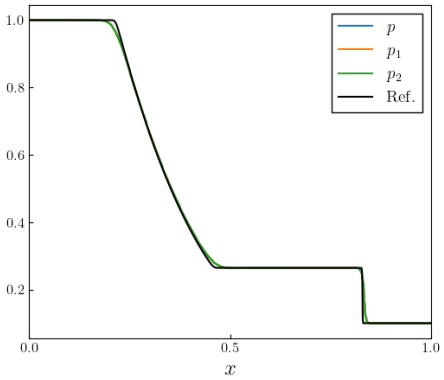

Pressure

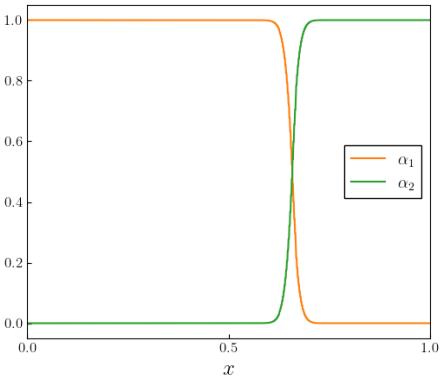

Volume fraction

Figure 7-35. Primitive variable profiles for the 1-D multimaterial Sod problem at $t = 0.2$ using the spatial-averaging discretization (Section 3.4). Pressures are controlled with the total equilibration algorithm (Section 6.1).

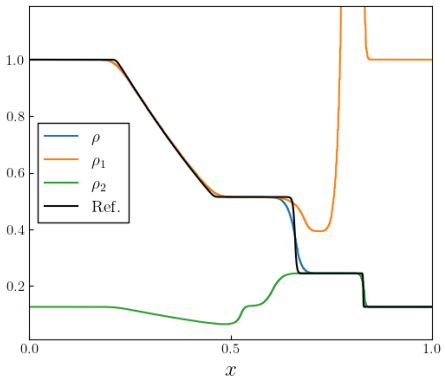

Density

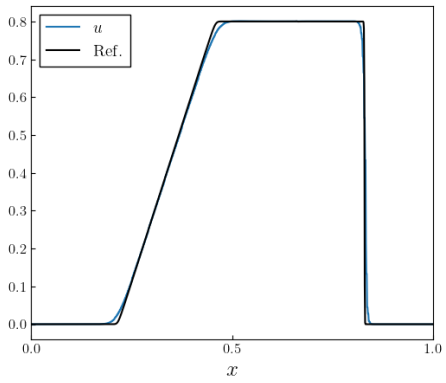

Velocity

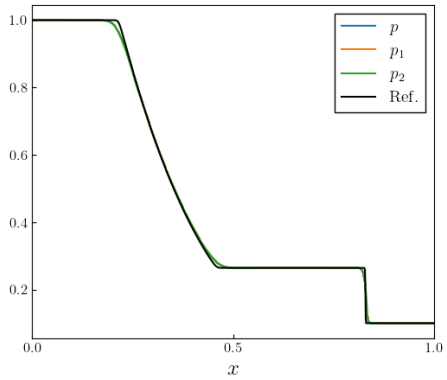

Pressure

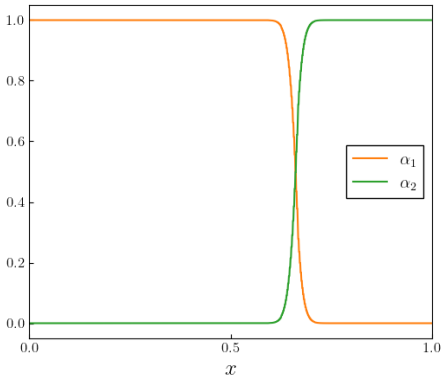

Volume fraction

Figure 7-36. Primitive variable profiles for the 1-D multimaterial Sod problem at $t = 0.2$ using the spatial-averaging discretization (Section 3.4). Pressures are controlled with the partial equilibration (Section 6.1) and instantaneous pressure relaxation (Section 6.2) algorithms.

7.10. 2-D Multimaterial Sod

We simulated the 2-D multimaterial Sod problem on $(x, y) \in [-1, 1] \times [-1, 1]$ with $N_e = 128 \times 128$ elements, upon which we impose the initial condition:

$$\begin{bmatrix} \rho_1 \\ \rho_2 \\ \vec{u} \\ p_k \\ \alpha_1 \\ \alpha_2 \end{bmatrix} = \begin{bmatrix} 1.0 \\ 0.1 \\ [1.0, 1.0] \\ 1.0 \\ 1.0 - \alpha_{\text{trace}} \\ \alpha_{\text{trace}} \end{bmatrix}, \quad \text{for } |\vec{x}| > 0.5, \qquad \begin{bmatrix} \rho_1 \\ \rho_2 \\ \vec{u} \\ p_k \\ \alpha_1 \\ \alpha_2 \end{bmatrix} = \begin{bmatrix} 1.0 \\ 0.1 \\ [1.0, 1.0] \\ 1.0 \\ \alpha_{\text{trace}} \\ 1.0 - \alpha_{\text{trace}} \end{bmatrix}, \quad \text{for } |\vec{x}| < 0.5, \tag{7.12}$$

where $|\vec{x}| = \sqrt{\vec{x} \cdot \vec{x}}$. Both material equations of state are described analytically by the ideal gas law, with $\gamma_1 = 2.0$ and $\gamma_2 = 1.4$. This problem was run for a simulated time of $t = 0.2$. For this problem, we use the solution limiting procedure described in Chapter 4. We use the volume fraction bounds preservation scheme described in Section 5.1 with $\alpha_{\text{floor}} = 10^{-12}$.

Figures 7-37 - 7-38 show the 2-D Sod problem after the wave structure has evolved. These figures show how extreme the unphysical material pressures p_k can become when the pressure relaxation terms in Eqns. (2.1) are untreated, highlighting the importance of the pressure equilibration/relaxation approaches described in Chapter 6. Note that the Pandare discretization crashes for this problem using these settings. Figure 7-39 shows the 2-D Sod problem using the total equilibration algorithm of Section 6.1. The pressures are equilibrated throughout the domain. Figure 7-40 shows the 2-D Sod problem after the interaction using the partial equilibration algorithm of Section 6.1 together with the instantaneous pressure algorithm of Section 6.2. The pressures are equilibrated throughout the domain.

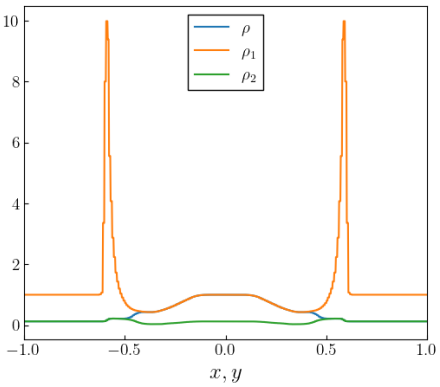

Density

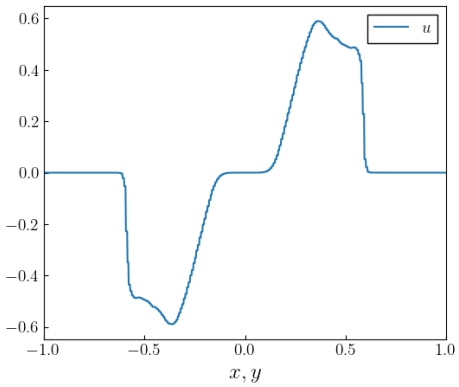

Velocity

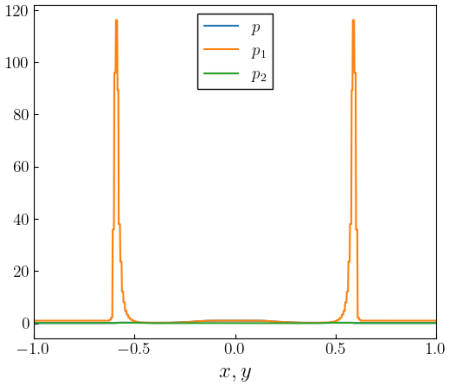

Pressure

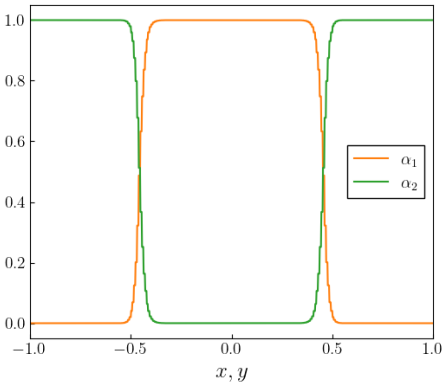

Volume fraction

Figure 7-37. Primitive variable profiles along the diagonal $x = y$ for the 2-D multimaterial Sod problem at $t = 0.2$ using the path-conservative discretization (Section 3.3). No pressure equilibration/relaxation.

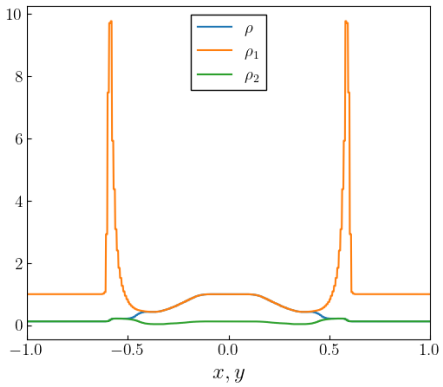

Density

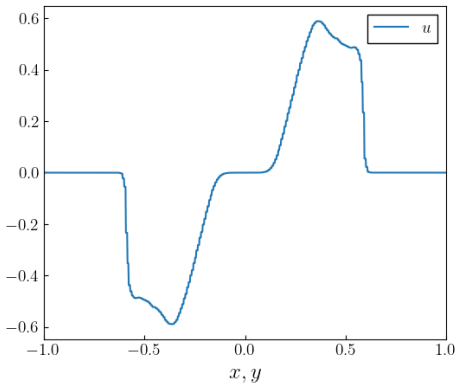

Velocity

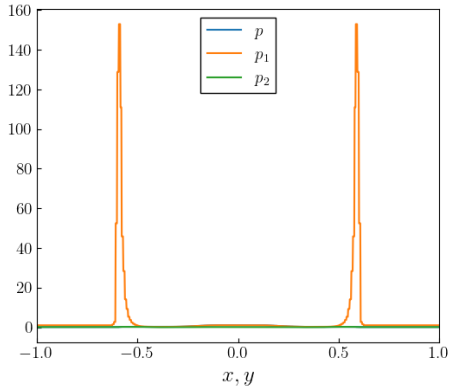

Pressure

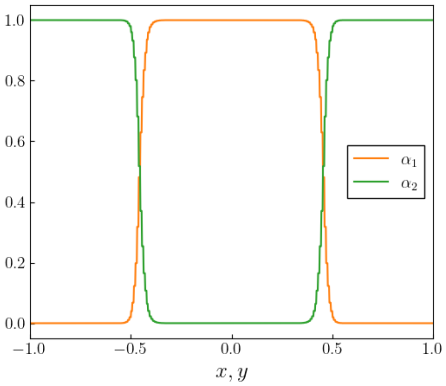

Volume fraction

Figure 7-38. Primitive variable profiles along the diagonal $x = y$ for the 2-D multimaterial Sod problem at $t = 0.2$ using the spatial-averaging discretization (Section 3.4). No pressure equilibration/relaxation.

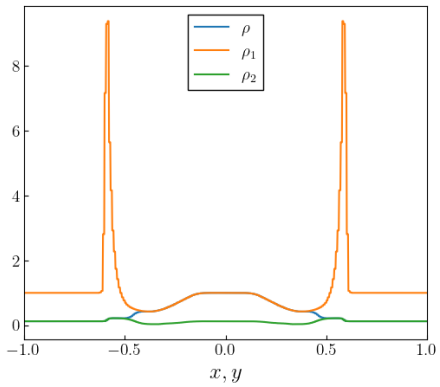

Density

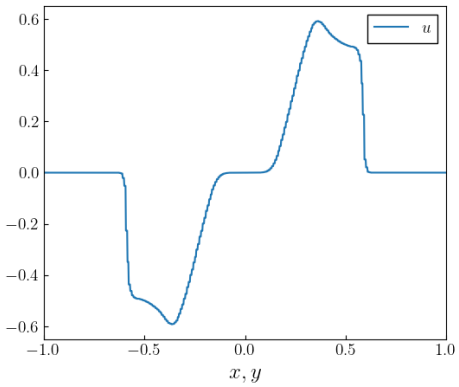

Velocity

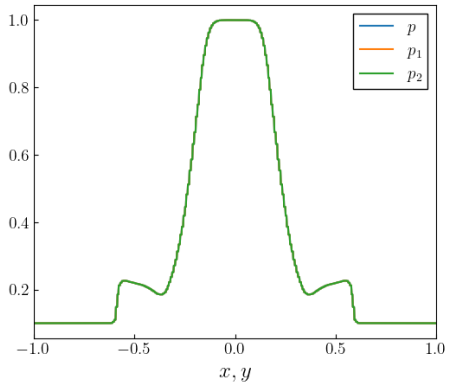

Pressure

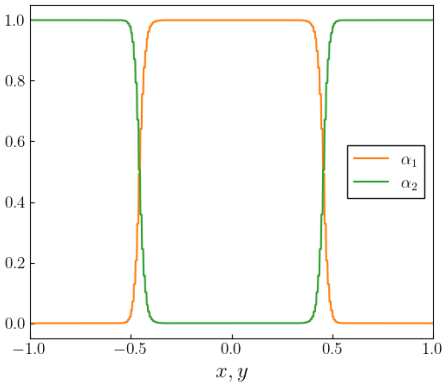

Volume fraction

Figure 7-39. Primitive variable profiles along the diagonal $x = y$ for the 2-D multimaterial Sod problem at $t = 0.2$ using the spatial-averaging discretization (Section 3.4). Pressures are controlled with the total equilibration algorithm (Section 6.1).

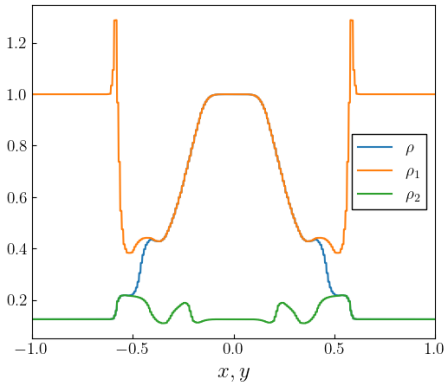

Density

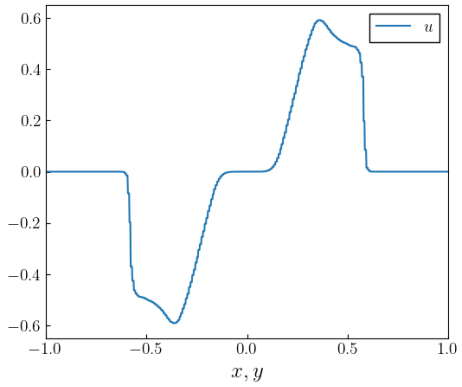

Velocity

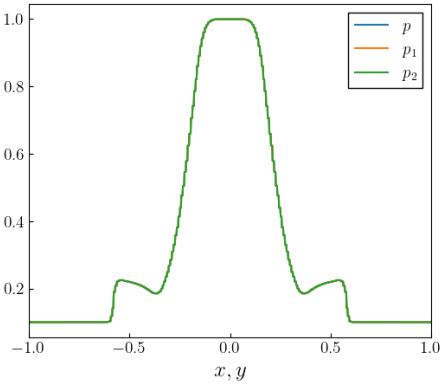

Pressure

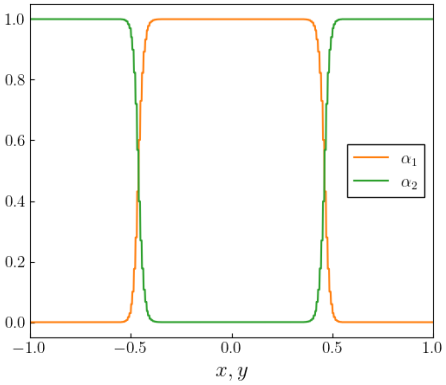

Volume fraction

Figure 7-40. Primitive variable profiles along the diagonal $x = y$ for the 2-D multimaterial Sod problem at $t = 0.2$ using the spatial-averaging discretization (Section 3.4). Pressures are controlled with the partial equilibration (Section 6.1) and instantaneous pressure relaxation (Section 6.2) algorithms.

7.11. 1-D Aluminum-Aluminum Collison

We simulated a 1-D collision of two Aluminum slabs, described by SESAME EOS tables [20], initially moving at equal and opposite velocities using a 1-D mesh on $x \in [0, 1000]$ μm with $N_e = 256$ elements, upon which we impose the initial condition:

$$\begin{aligned}
\begin{bmatrix} \rho_k \\ u \\ T_k \\ \alpha_1 \\ \alpha_2 \end{bmatrix} &= \begin{bmatrix} 2700 \text{ kg/m}^3 \\ 5000 \text{ m/s} \\ 298.15 \text{ K} \\ 1.0 - \alpha_{\text{trace}} \\ \alpha_{\text{trace}} \end{bmatrix}, \quad \text{for } x > 500 \ \mu\text{m (Aluminum)}, \\
\begin{bmatrix} \rho_k \\ u \\ T_k \\ \alpha_1 \\ \alpha_2 \end{bmatrix} &= \begin{bmatrix} 2700 \text{ kg/m}^3 \\ -5000 \text{ m/s} \\ 298.15 \text{ K} \\ \alpha_{\text{trace}} \\ 1.0 - \alpha_{\text{trace}} \end{bmatrix}, \quad \text{for } x < 500 \ \mu\text{m (Aluminum)}.
\end{aligned} \tag{7.13}$$

This problem was run for a simulated time of $t = 0.1$ s. For this problem, we use the solution limiting procedure described in Chapter 4. We use the volume fraction bounds preservation scheme described in Section 5.1 with with $\alpha_{\text{floor}} = 10^{-12}$, and the state variable bounds preservation scheme described in Section 5.2.

Figure 7-41 shows the 1-D Al-Al collision problem after the collision has evolved. These figures show how extreme the unphysical material pressures p_k can become when the pressure relaxation terms in Eqns. (2.1) are untreated, highlighting the importance of the pressure equilibration/relaxation approaches described in Chapter 6. Figure 7-42 shows the 1-D Al-Al collision problem using the total equilibration algorithm of Section 6.1. In this case, due to the relatively low initial temperature and pressure of the material, the equilibrated state is off the SESAME table, so the material pressures p_k are not equilibrated throughout the domain. Thus, the pressures are closer to one another than seen in Figure 7-42, but not completely equilibrated.

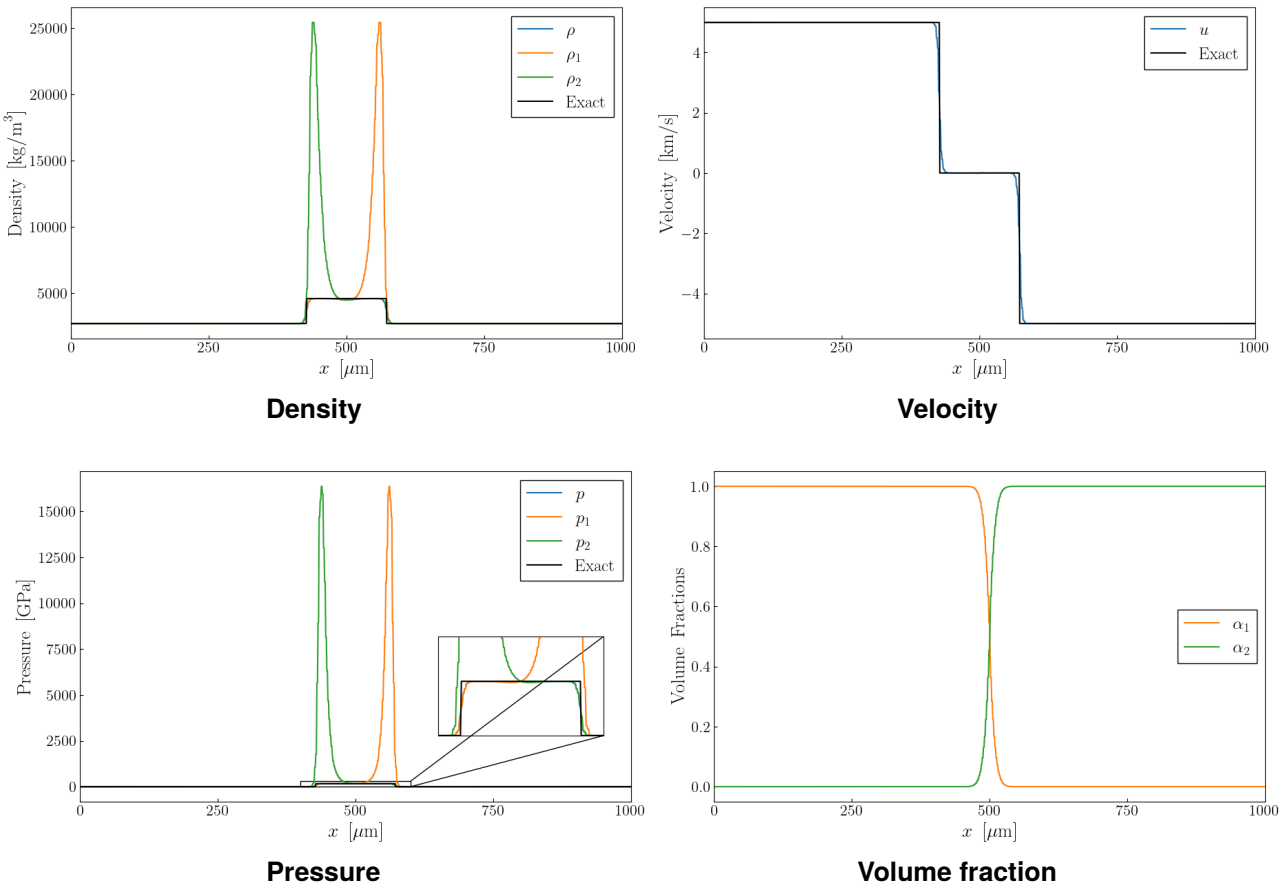

Figure 7-41. Primitive variable profiles for the 1-D Al-Al collision problem at $t = 0.1$ s using the spatial-averaging discretization (Section 3.4).

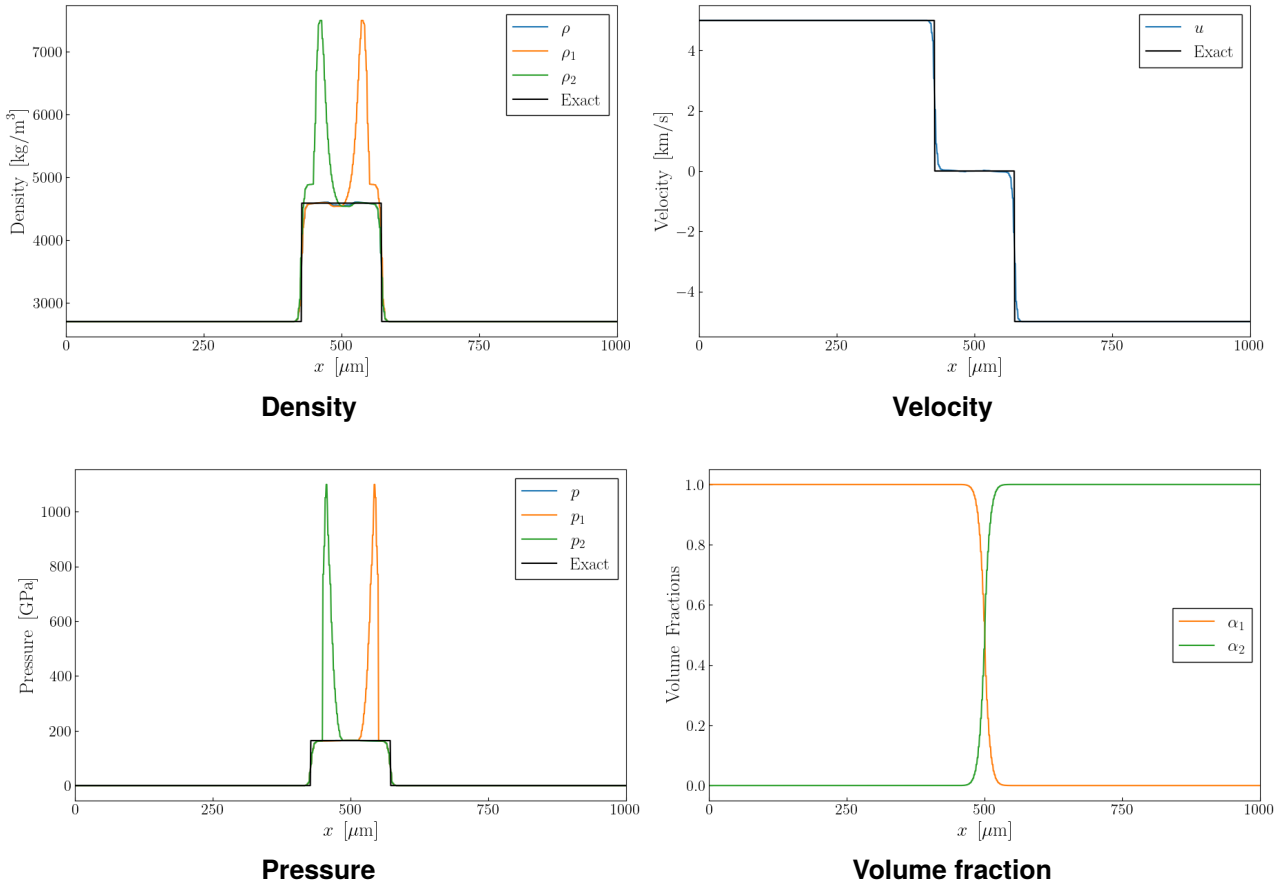

Figure 7-42. Primitive variable profiles for the 1-D Al-Al collision problem at $t = 0.1$ s using the spatial-averaging discretization (Section 3.4). Pressures are controlled with the total equilibration algorithm (Section 6.1).

7.12. 1-D Aluminum-Copper Collison

We simulated a 1-D collision of an Aluminum and a Copper slab, both described by SESAME EOS tables [20], initially moving at equal and opposite velocities using a 1-D mesh on $x \in [0, 1000]$ μm with $N_e = 256$ elements, upon which we impose the initial condition:

$$\begin{aligned}
\begin{bmatrix} \rho_k \\ u \\ T_k \\ \alpha_1 \\ \alpha_2 \end{bmatrix} &= \begin{bmatrix} 2700 \text{ kg/m}^3 \\ 5000 \text{ m/s} \\ 298.15 \text{ K} \\ 1.0 - \alpha_{\text{trace}} \\ \alpha_{\text{trace}} \end{bmatrix}, \quad \text{for } x > 500 \ \mu\text{m (Aluminum)}, \\
\begin{bmatrix} \rho_k \\ u \\ T_k \\ \alpha_1 \\ \alpha_2 \end{bmatrix} &= \begin{bmatrix} 8939 \text{ kg/m}^3 \\ -5000 \text{ m/s} \\ 298.15 \text{ K} \\ \alpha_{\text{trace}} \\ 1.0 - \alpha_{\text{trace}} \end{bmatrix}, \quad \text{for } x < 500 \ \mu\text{m (Copper)}.
\end{aligned} \tag{7.14}$$

This problem was run for a simulated time of $t = 0.1$ s. For this problem, we use the solution limiting procedure described in Chapter 4. We use the volume fraction bounds preservation scheme described in Section 5.1 with with $\alpha_{\text{floor}} = 10^{-12}$, and the state variable bounds preservation scheme described in Section 5.2.

Figure 7-43 shows the 1-D Al-Cu collision problem after the collision has evolved. These figures show how extreme the unphysical material pressures p_k can become when the pressure relaxation terms in Eqns. (2.1) are untreated, highlighting the importance of the pressure equilibration/relaxation approaches described in Chapter 6. Figure 7-44 shows the 1-D Al-Cu collision problem using the total equilibration algorithm of Section 6.1. In this case, due to the relatively low initial temperatures and pressures of the materials, the equilibrated states are off the SESAME table, so the material pressures p_k are not equilibrated throughout the domain. Thus, the pressures are closer to one another than in Figure 7-44, but not completely equilibrated.

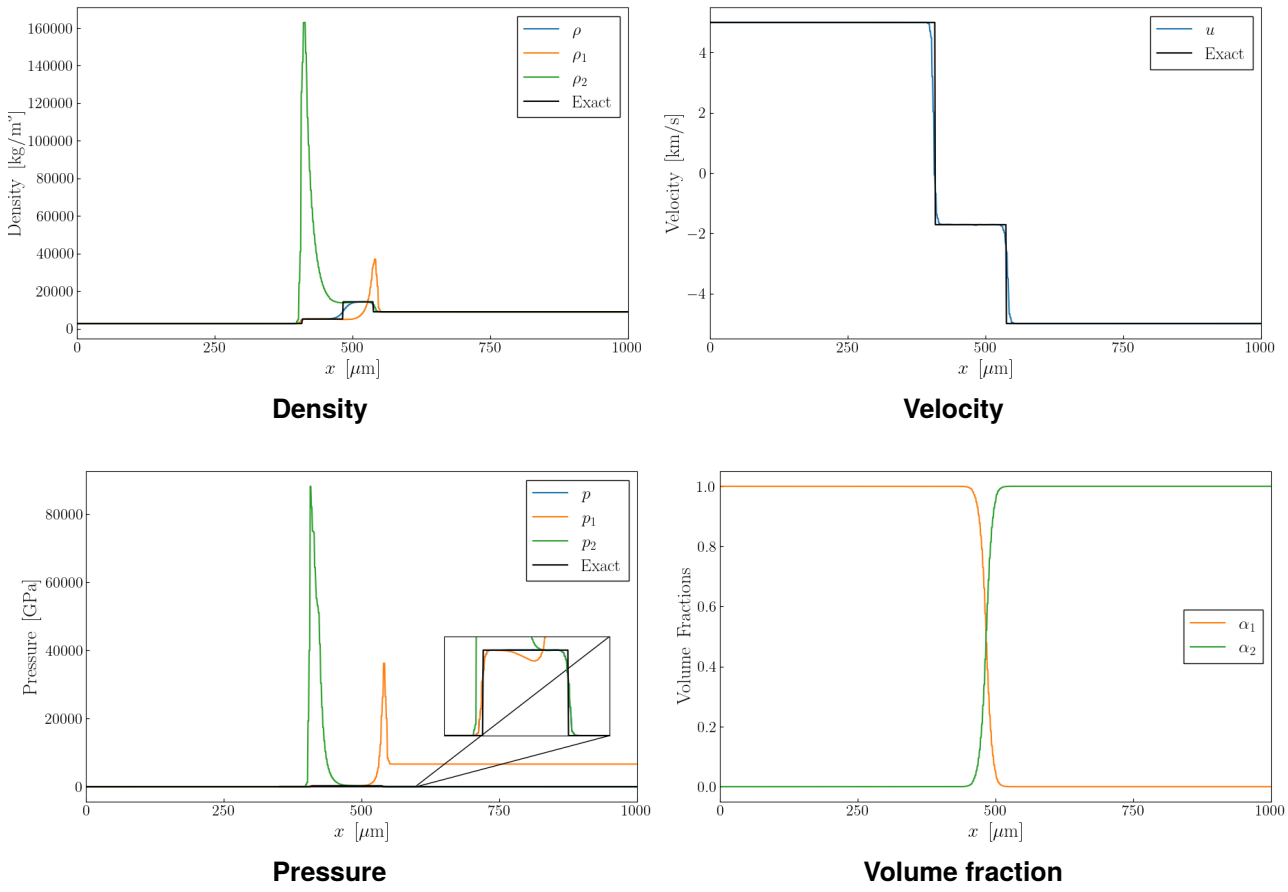

Figure 7-43. Primitive variable profiles for the 1-D Al-Cu collision problem at $t = 0.1$ s using the spatial-averaging discretization (Section 3.4).

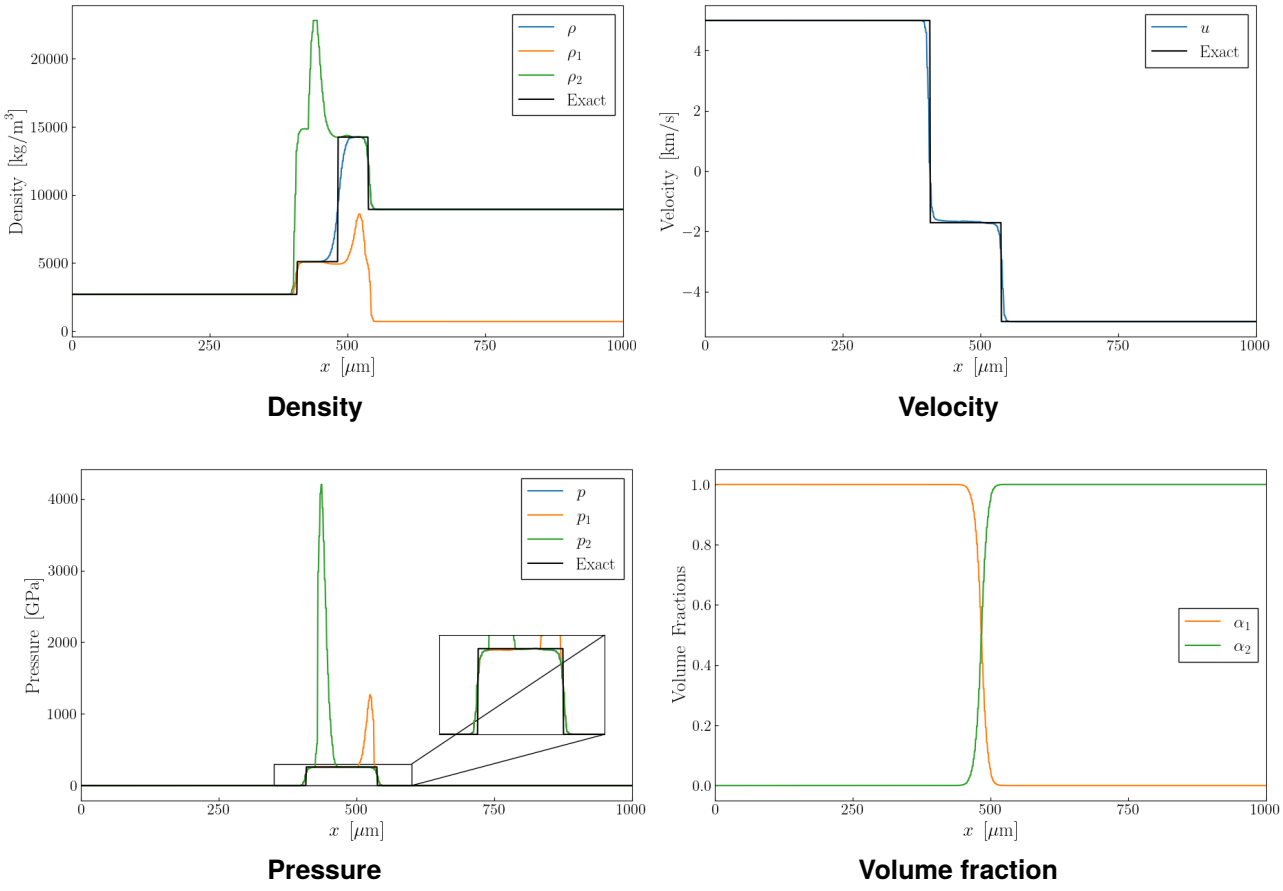

Figure 7-44. Primitive variable profiles for the 1-D Al-Cu collision problem at $t = 0.1$ s using the spatial-averaging discretization (Section 3.4). Pressures are controlled with the total equilibration algorithm (Section 6.1).

7.13. 2-D XMHD Liner Implosion

We simulated the 2-D implosion of a Beryllium liner described by a SESAME EOS table [20], driven by a magnetic field boundary condition, on $(x, y) \in [-15, 15] \times [-15, 15]$ μm with $N_e = 600 \times 600$ elements, upon which we impose the initial condition:

$$\begin{aligned}
\begin{bmatrix} \rho_k \\ \vec{u} \\ T_k \\ \alpha_1 \\ \alpha_2 \end{bmatrix} &= \begin{bmatrix} 1845 \text{ kg/m}^3 \\ [0.0, 0.0] \text{ m/s} \\ 293.15 \text{ K} \\ 1.0 - \alpha_{\text{trace}} \\ \alpha_{\text{trace}} \end{bmatrix}, \quad \text{for } 2.325\ \mu\text{m} < |\vec{x}| < 2.79\ \mu\text{m (Beryllium)}, \\
\begin{bmatrix} \rho_k \\ \vec{u} \\ T_k \\ \alpha_1 \\ \alpha_2 \end{bmatrix} &= \begin{bmatrix} 1 \times 10^{-6} \text{ kg/m}^3 \\ [0.0, 0.0] \text{ m/s} \\ 293.15 \text{ K} \\ \alpha_{\text{trace}} \\ 1.0 - \alpha_{\text{trace}} \end{bmatrix}, \quad \text{otherwise (Air)}.
\end{aligned} \tag{7.15}$$

This problem was run for a simulated time of $t = 150$ ns. For this problem, we use the solution limiting procedure described in Chapter 4. We use the volume fraction bounds preservation scheme described in Section 5.1 with with $\alpha_{\text{floor}} = 10^{-12}$, and the state variable bounds preservation scheme described in Section 5.2. This problem was run without using any of the pressure equilibration/relaxation approaches of Chapter 6. In this problem, the Beryllium table is used for both materials, as this is an initial demonstration. Furthermore, we will not detail the XMHD modeling or related numerical methods in FLEXO here. We include results for this problem solely to illustrate early success using the multimaterial approach described in this report in the context of XMHD problems. This is still an ongoing area of development within the FLEXO code.

Figure 7-45 shows the mixture density of the 2-D XMHD liner implosion problem. The collapse is very symmetric, but the subsequent expansion after maximum compression has some asymmetric features, likely due to grid imprinting. Figure 7-46 shows the primitive variable profiles of the 2-D XMHD liner implosion problem at maximum compression. The collapse also appears symmetric here, but the material pressures are very far from equilibrium and the volume fractions are diffused to an extent that the interface is no longer captured effectively at this resolution but instead is dissipated over the entire target region. These two observations serve to motivate the directions of future development of the FLEXO code itemized in Section 9.2.

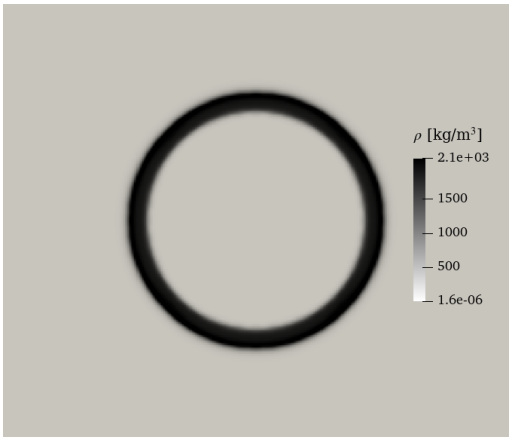

$t = 30$ **ns**

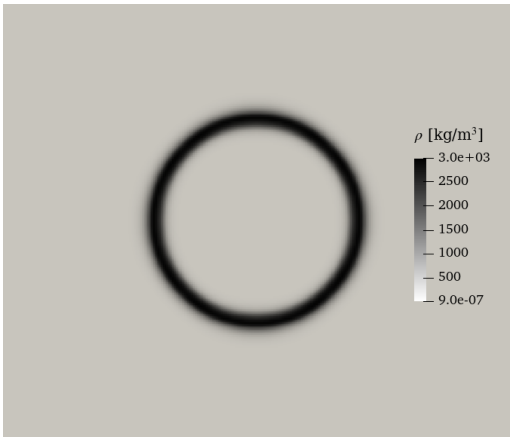

$t = 70$ **ns**

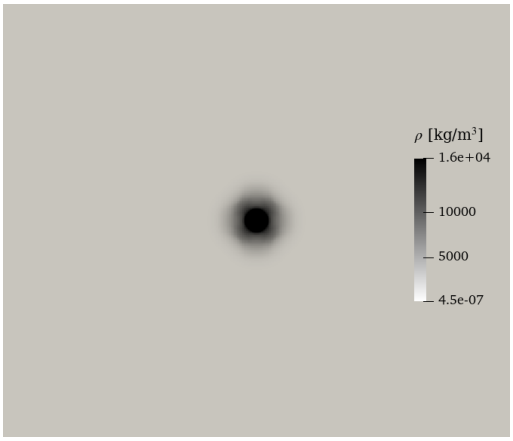

$t = 110$ **ns**

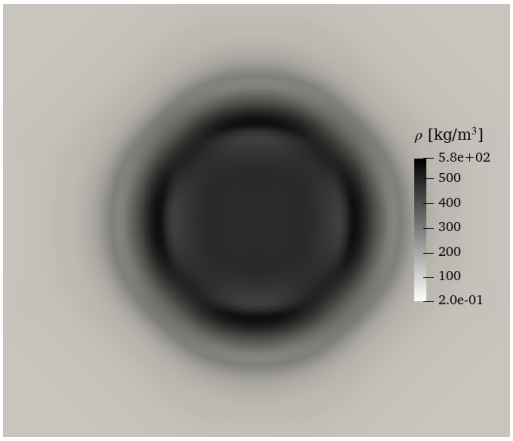

$t = 150$ **ns**

Figure 7-45. Mixture density for the 2-D XMHD liner implosion problem at various times using the spatial-averaging discretization (Section 3.4).

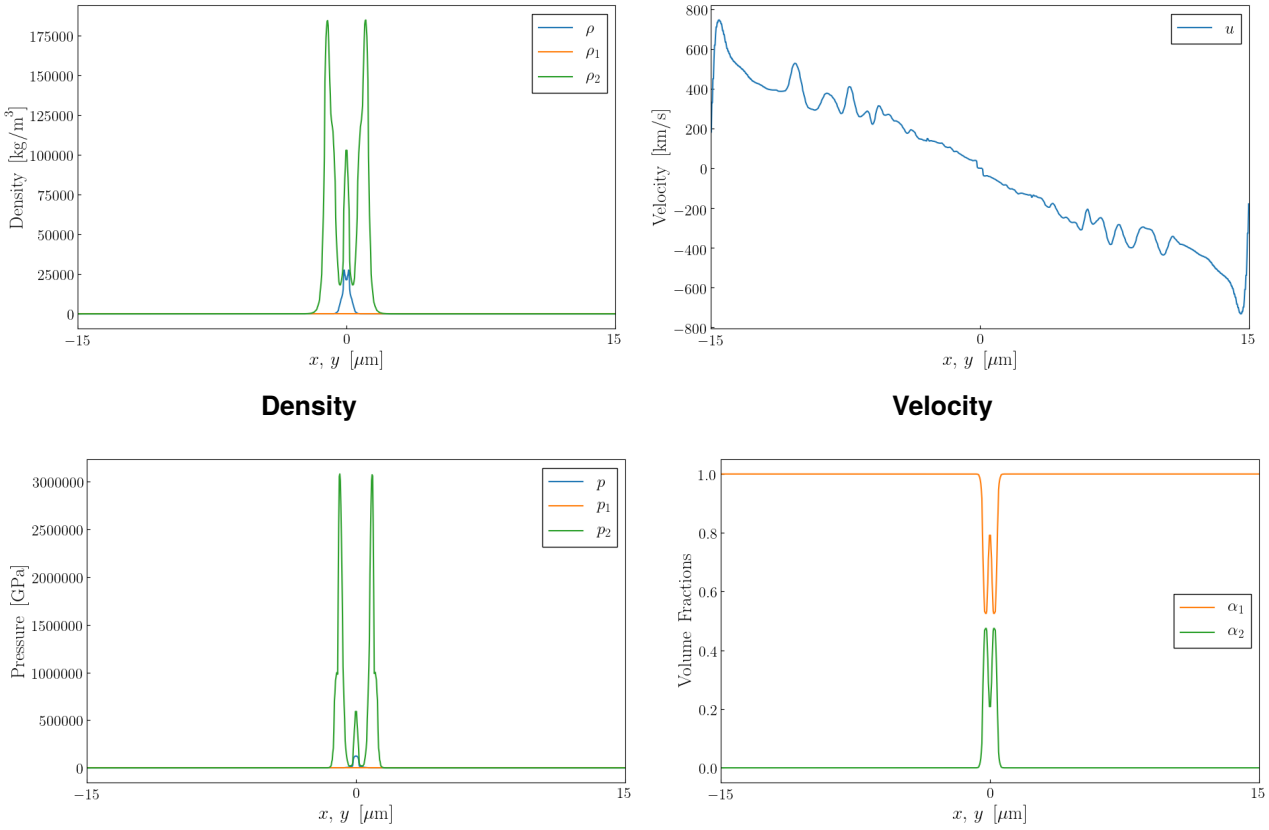

Figure 7-46. Primitive variable profiles for the 2-D XMHD liner implosion problem along $x = y$ at $t = 110$ ns using the spatial-averaging discretization (Section 3.4).

8. LARGE-SCALE SIMULATIONS

In this chapter, we include some preliminary results of large-scale, application-relevant FLEXO simulations of pulsed power systems. This will demonstrate that the multimaterial developments described in this document have enhanced the capabilities of the FLEXO code, enabling high-fidelity simulation of pulsed power systems featuring multiple materials. We will not describe these simulations in detail, nor analyze the results here. The simulations in this chapter use the spatial-averaging discretization (Section 3.3), a polynomial order of $P = 1$, and the Harten-Lax-van Leer numerical flux described in Section B.2.

8.1. Double-Shell Simulations

The double cylinder platform is a cross-lab effort between Sandia National Laboratories and Los Alamos National Laboratory. Based on the Decel platform [48], the double shell platform consists of nested beryllium liners filled with liquid deuterium. The current of the Z Pulsed Power Facility is used to drive the implosion of the outer cylinder, which in turn compresses the liquid deuterium between it and the inner cylinder. This hydrodynamically implodes the inner cylinder. By creating a scenario where the implosion of the inner beryllium liner is driven purely hydrodynamically, the ability to simulate the platform is expanded to codes that do not model magnetohydrodynamics. This makes it a valuable cross-lab and cross-code comparison and validation platform. The simulation of a 3-D double-shell implosion using the multimaterial capability established in this report is depicted in Figure 8-1.

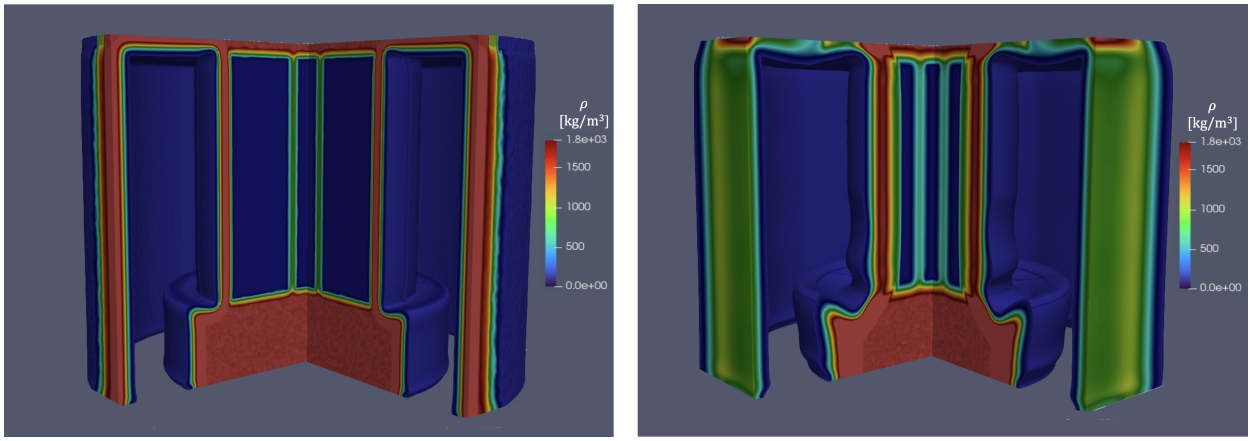

$t = 100$ **ns** $t = 200$ **ns**

Figure 8-1. Mixture density for the double-shell implosion at different times.

8.2. Ice Fiber MagLIF Simulations

MagLIF requires the fuel to be preheated in some way, which is typically done on the Z Pulsed Power Facility using the Z-Beamlet Laser. This approach adds complexity and has taken many years of work to optimize. In addition, requiring the laser for fuel pre-heat removes it as a diagnostic tool for x-ray backlight imaging. There is currently an effort to instead make use of part of the Z current pulse to preheat the fuel [16, 19]. The Z architecture lends itself to having one of the powerfeed levels being directed into the fuel instead of contributing to the flow of current through the inside of the target. When this is coupled with an extruded deuterium ice fiber, it can create a hot deuterium fuel without the need for a laser system. This type of MagLIF target has been successfully fielded on Z, but codes such as FLEXO that can perform high-fidelity 3-D simulations of this process will be necessary for optimizing and refining this technology. The simulation of a 3-D Ice Fiber MagLIF implosion using the multimaterial capability established in this report is depicted in Figure 8-2.

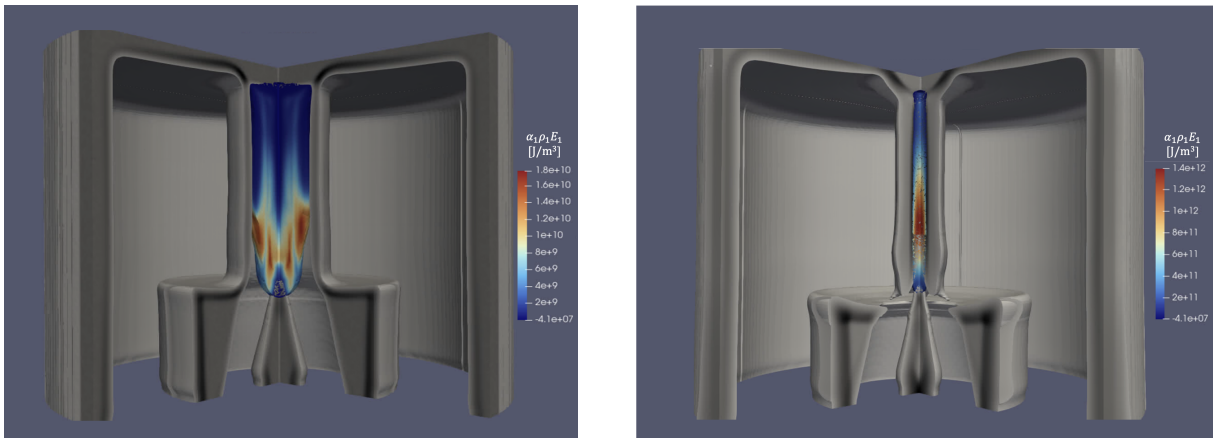

t = 115 **ns** t = 150 **ns**

Figure 8-2. Partial total energy density of the deuterium fuel for the ice fiber MagLIF implosion at different times.

9. CONCLUSIONS AND ONGOING WORK

9.1. Conclusions

In the present report we designed, implemented, and verified a discontinuous Galerkin scheme for the six-equation interface capturing model of Pelanti and Shuye in a manner allowing 3-D simulation of an arbitrary number of materials. This scheme was implemented in the FLEXO XMHD code and will serve as its base scheme for multimaterial hydrodynamics. We described and analyzed three different discretizations for the nonconservative terms in the six-equation model, showing that the two novel discretizations (our path-conservative and spatial-averaging discretizations) are well balanced in the case of an isolated material interface. Additionally, we described a bounds-preservation scheme and a solution limiting algorithm that are designed to maintain the equilibria of primitive variables. We also described approaches for pressure equilibration/relaxation that drive the materials into pressure equilibrium with one another. This serves to prevent the material pressures from attaining unphysical values, enhancing the robustness of the overall scheme. We presented results for a collection of 1-D and 2-D verification problems which demonstrated that this overall interface capturing scheme is accurate and robust for many problems of interest. Additionally, the results of these verification problems demonstrated the importance of having a robust pressure equilibration approach, as well as provided insight into how material interfaces are best initialized using this six-equation model. Then, we introduced a few large-scale FLEXO simulations of pulsed power systems that use the multimaterial capability established within this document. These results demonstrate that these new multimaterial capabilities allow FLEXO users to conduct high-fidelity simulations of multimaterial XMHD systems, allowing FLEXO to serve as a tool for experimental design as well as for exploring pulsed power physics.

9.2. Ongoing Development

The following items are ongoing areas of development in the FLEXO code:

- *Extension to higher order*: the bounds-preservation and solution limiting approaches should be extended to higher order to enable more efficient resolution of smooth features and sharper capturing of discontinuous features. The chief difficulty of this effort will be in extending discontinuity capturing approaches (e.g., solution limiting, artificial viscosity) to high-order DG solutions in a robust manner that does not disturb equilibrium in this multimaterial context, as was accomplished here in the $P = 1$ case.
- *Pressure relaxation*: in this work, we have demonstrated that unphysical values of the material pressures p_k can be attained when pressure equilibration terms in Equation (2.1) are not treated. We believe that finite pressure relaxation (where the pressure source terms

in Equations (2.1a) and (2.1d) are modeled and integrated explicitly) in the style of Tipton et al. [33] would be more physically faithful and possibly more robust than the methods of Chapter 6.

- *Interface sharpening*: For many of the applications of XMHD, a multimaterial algorithm should feature sharp interfaces. Extending the approaches described in this work to higher order with a means of selective dissipation (e.g., a physics-based sensor for selectively applying limiting) for stabilizing discontinuities would be the first means of attaining this, but it is possible that this will still be insufficient for the application demands. In this case, some interface compression approach (e.g., THINC [25, 39]) should be employed to control/limit the dissipation of material interfaces.

REFERENCES

[1] Rémi Abgrall and Smadar Karni. A comment on the computation of non-conservative products. *Journal of Computational Physics*, 229(8):2759–2763, 2010.

[2] Marissa B. Adams, Stephen D. Bond, Steven W. Bova, Griffin S. Cearley, Kyle Cochrane, Michael M. Crockatt, Thomas A. Gardiner, Brian N. Granzow, Nathaniel D. Hamlin, Matthew R. Martin, Luke N. Shulenburger, Alan K. Stagg, Thomas E. Voth, Matthew R. Weis, Jeffrey M. Woolstrum, and Nedim A. Yusef. FLEXO: A Portably Performant Code for Pulsed Power Target Physics. Technical Report SAND2024-12834, Sandia National Laboratories, 2024.

[3] Sina Arabi, Jean-Yves Trépanier, and Ricardo Camarero. A simple extension of Roe's scheme for real gases. *Journal of Computational Physics*, 329:16–28, 2017.

[4] J.C. Butcher and G. Wanner. Runge-Kutta methods: some historical notes. *Applied Numerical Mathematics*, 22(1):113–151, 1996. Special Issue Celebrating the Centenary of Runge-Kutta Methods.

[5] Waixiang Cao, Chi-Wang Shu, Yang Yang, and Zhimin Zhang. Superconvergence of Discontinuous Galerkin Method for Scalar Nonlinear Hyperbolic Equations. *SIAM Journal on Numerical Analysis*, 56(2):732–765, 2018.

[6] M.J. Castro, T. Morales de Luna, and C. Parés. Chapter 6 - Well-Balanced Schemes and Path-Conservative Numerical Methods. In Rémi Abgrall and Chi-Wang Shu, editors, *Handbook of Numerical Methods for Hyperbolic Problems*, volume 18 of *Handbook of Numerical Analysis*, pages 131–175. Elsevier, 2017.

[7] Griffin Cearley. *Analytical and Computational Techniques for Fluid Flows Interacting with Intense Radiation Fields*. PhD thesis, 2022.

[8] Bernardo Cockburn, Suchung Hou, and Chi-Wang Shu. The Runge-Kutta Local Projection Discontinuous Galerkin Finite Element Method for Conservation Laws. IV: The Multidimensional Case. *Mathematics of Computation*, 54(190):545–581, 1990.

[9] Bernardo Cockburn, George E. Karniadakis, and Chi-Wang Shu. *Discontinuous Galerkin methods: theory, computation and applications*, volume 11. Springer Science & Business Media, 2012.

[10] Bernardo Cockburn and Chi-Wang Shu. TVB Runge-Kutta local projection discontinuous Galerkin finite element method for conservation laws. II. General framework. *Mathematics of Computation*, 52(186):411–435, 1989.

[11] Bernardo Cockburn and Chi-Wang Shu. Runge–Kutta discontinuous Galerkin methods for convection-dominated problems. *Journal of Scientific Computing*, 16:173–261, 2001.

[12] G. DalMaso, P.G. LeFloch, and F. Murat. Definition and weak stability of nonconservative products. *Journal de Mathématiques Pures et Appliquées*, 74(6):483–548, 1995.

[13] S. F. Davis. Simplified Second-Order Godunov-Type Methods. *SIAM Journal on Scientific and Statistical Computing*, 9(3):445–473, 1988.

[14] M. De Lorenzo, M. Pelanti, and Ph. Lafon. HLLC-type and path-conservative schemes for a single-velocity six-equation two-phase flow model: A comparative study. *Applied Mathematics and Computation*, 333:95–117, 2018.

[15] T. Dzanic. Continuously bounds-preserving discontinuous Galerkin methods for hyperbolic conservation laws. *Journal of Computational Physics*, 508:113010, 2024.

[16] Matthew R. Gomez et al. Demonstrating dual current paths as a method to preheat and implode a magneto-inertial fusion target. In *International Conference on Inertial Fusion Sciences and Applications*, 2025.

[17] Amiram Harten, Peter D. Lax, and Bram van Leer. On Upstream Differencing and Godunov-Type Schemes for Hyperbolic Conservation Laws. *SIAM Review*, 25(1):35–61, 1983.

[18] Marc T. Henry de Frahan, Sreenivas Varadan, and Eric Johnsen. A new limiting procedure for discontinuous Galerkin methods applied to compressible multiphase flows with shocks and interfaces. *Journal of Computational Physics*, 280:489–509, 2015.

[19] Christopher A. Jennings, Matthew R. Gomez, Maren W. Hatch, Thomas J. Awe, Stephen A. Slutz, Matt R. Weis, Daniel E. Ruiz, Adam J. Harvey-Thompson, Luke Shulenburger, David J. Ampleford, et al. Pulsed power driven preheat using a cryogenic Ice fiber for MagLiF experiments on Z. In *Division of Plasma Physics 2025*. American Physical Society, 2025.

[20] J. D. Johnson. The SESAME database. Los Alamos National Lab., NM (United States), 06 1994.

[21] A. K. Kapila, R. Menikoff, J. B. Bdzil, S. F. Son, and D. S. Stewart. Two-phase modeling of deflagration-to-detonation transition in granular materials: Reduced equations. *Physics of Fluids*, 13(10):3002–3024, 10 2001.

[22] Peter D. Lax. Weak solutions of nonlinear hyperbolic equations and their numerical computation. *Communications on Pure and Applied Mathematics*, 7(1):159–193, 1954.

[23] Weizhao Li, Hong Luo, Aditya Pandare, and Jozsef Bakosi. A p-adaptive Discontinuous Galerkin Method for Compressible Flows Using Charm++. In *AIAA Scitech 2020 Forum*, page 1565, 2020.

[24] Craig Michoski, Chris Mirabito, Clint Dawson, Damrongsak Wirasaet, Ethan J. Kubatko, and Joannes J. Westerink. Adaptive hierarchic transformations for dynamically p-enriched slope-limiting over discontinuous Galerkin systems of generalized equations. *Journal of Computational Physics*, 230(22):8028–8056, 2011.

[25] Aditya Pandare, Weizhao Li, Jacob Waltz, Jozsef Bakosi, and Hong Luo. A THINC-DG Method for Multi-Material Fluid Flow. In *AIAA Scitech 2022 Forum*.

[26] Aditya K. Pandare, Jacob Waltz, and Jozsef Bakosi. A reconstructed discontinuous Galerkin method for multi-material hydrodynamics with sharp interfaces. *International Journal for Numerical Methods in Fluids*, 92(8):874–898, 2020.

[27] Aditya K. Pandare, Jacob Waltz, Weizhao Li, Hong Luo, and Jozsef Bakosi. On the design of stable, consistent, and conservative high-order methods for multi-material hydrodynamics. *Journal of Computational Physics*, 490:112313, October 2023.

[28] Marica Pelanti and Keh-Ming Shyue. A mixture-energy-consistent six-equation two-phase numerical model for fluids with interfaces, cavitation and evaporation waves. *Journal of Computational Physics*, 259:331–357, 2014.

[29] Marica Pelanti and Keh-Ming Shyue. A numerical model for multiphase liquid–vapor–gas flows with interfaces and cavitation. *International Journal of Multiphase Flow*, 113:208–230, 2019.

[30] Jianxian Qiu and Chi-Wang Shu. Hermite WENO schemes and their application as limiters for Runge–Kutta discontinuous Galerkin method: one-dimensional case. *Journal of Computational Physics*, 193(1):115–135, 2004.

[31] S. Rhebergen, O. Bokhove, and J.J.W. van der Vegt. Discontinuous Galerkin finite element methods for hyperbolic nonconservative partial differential equations. *Journal of Computational Physics*, 227(3):1887–1922, 2008.

[32] Richard Saurel, Fabien Petitpas, and Ray A. Berry. Simple and efficient relaxation methods for interfaces separating compressible fluids, cavitating flows and shocks in multiphase mixtures. *Journal of Computational Physics*, 228(5):1678–1712, 2009.

[33] W. J. Rider, E. Love, M. K. Wong, O. E. Strack, S. V. Petney, and D. A. Labreche. Adaptive methods for multi-material ALE hydrodynamics. *International Journal for Numerical Methods in Fluids*, 65(11-12):1325–1337, 2011.

[34] P. L. Roe. Approximate Riemann solvers, parameter vectors, and difference schemes. *Journal of Computational Physics*, 43(2):357–372, 1981.

[35] V. V. Rusanov. Calculation of interaction of non-steady shock waves with obstacles, 1961.

[36] C. E. Seyler and M. R. Martin. Relaxation model for extended magnetohydrodynamics: Comparison to magnetohydrodynamics for dense z-pinches. *Physics of Plasmas*, 18(1):012703, 01 2011.

[37] C. E. Seyler, M. R. Martin, and N. D. Hamlin. Helical instability in MagLIF due to axial flux compression by low-density plasma. *Physics of Plasmas*, 25(6):062711, 06 2018.

[38] M. Shashkov. Closure models for multimaterial cells in arbitrary Lagrangian–Eulerian hydrocodes. *International Journal for Numerical Methods in Fluids*, 56(8):1497–1504, 2008.

[39] Keh-Ming Shyue and Feng Xiao. An Eulerian interface sharpening algorithm for compressible two-phase flow: The algebraic THINC approach. *Journal of Computational Physics*, 268:326–354, 2014.

[40] D. B. Sinars, S. A. Slutz, M. C. Herrmann, R. D. McBride, M. E. Cuneo, K. J. Peterson, R. A. Vesey, C. Nakhleh, B. E. Blue, K. Killebrew, D. Schroen, K. Tomlinson, A. D. Edens, M. R. Lopez, I. C. Smith, J. Shores, V. Bigman, G. R. Bennett, B. W. Atherton, M. Savage, W. A. Stygar, G. T. Leifeste, and J. L. Porter. Measurements of Magneto-Rayleigh-Taylor Instability Growth during the Implosion of Initially Solid Al Tubes Driven by the 20-MA, 100-ns Z Facility. *Phys. Rev. Lett.*, 105:185001, Oct 2010.

[41] S. A. Slutz, T. J. Awe, and J. A. Crabtree. Dense hydrogen layers for high performance MagLIF. *Physics of Plasmas*, 29(2):022701, 02 2022.

[42] S. A. Slutz, W. A. Stygar, M. R. Gomez, K. J. Peterson, A. B. Sefkow, D. B. Sinars, R. A. Vesey, E. M. Campbell, and R. Betti. Scaling magnetized liner inertial fusion on Z and future pulsed-power accelerators. *Physics of Plasmas*, 23(2):022702, 02 2016.

[43] E. F. Toro, M. Spruce, and W. Speares. Restoration of the contact surface in the HLL-Riemann solver. *Shock Waves*, 4(1):25–34, 1994.

[44] Eleuterio F. Toro. *Riemann solvers and numerical methods for fluid dynamics: a practical introduction*. Springer Science & Business Media, 2013.

[45] Marcel Vinokur and Jean-Louis Montagné. Generalized flux-vector splitting and Roe average for an equilibrium real gas. *Journal of Computational Physics*, 89(2):276–300, 1990.

[46] William J. White, Ziyang Huang, and Eric Johnsen. A high-order discontinuous Galerkin method for compressible interfacial flows with consistent and conservative Phase Fields. *Journal of Computational Physics*, 527:113830, 2025.

[47] J. M. Woolstrum, D. E. Ruiz, N. D. Hamlin, K. Beckwith, and M. R. Martin. Hall interchange instability as a seed for helical magneto-Rayleigh–Taylor instabilities in magnetized liner inertial fusion Z-Pinches scaled from Z-Machine parameters to a next generation pulsed power facility. *Physics of Plasmas*, 30(7):072712, 07 2023.

[48] D. A. Yager-Elorriaga, F. W. Doss, G. A. Shipley, P. F. Knapp, D. E. Ruiz, A. J. Porwitzky, J. R. Fein, E. C. Merritt, M. R. Martin, C. E. Myers, C. A. Jennings, I. C. Smith, D. J. Marshall, C. R. Aragon, L. Shulenburger, T. R. Mattsson, and D. B. Sinars. Studying the Richtmyer–Meshkov instability in convergent geometry under high energy density conditions using the Decel platform. *Physics of Plasmas*, 29(5):052114, 05 2022.

[49] D.A. Yager-Elorriaga, M.R. Gomez, D.E. Ruiz, S.A. Slutz, A.J. Harvey-Thompson, C.A. Jennings, P.F. Knapp, P.F. Schmit, M.R. Weis, T.J. Awe, G.A. Chandler, M. Mangan, C.E. Myers, J.R. Fein, B.R. Galloway, M. Geissel, M.E. Glinsky, S.B. Hansen, E.C. Harding, D.C. Lamppa, W.E. Lewis, P.K. Rambo, G.K. Robertson, M.E. Savage, G.A. Shipley, I.C. Smith, J. Schwarz, D.J. Ampleford, K. Beckwith, K.J. Peterson, J.L. Porter, G.A. Rochau, and D.B. Sinars. An overview of magneto-inertial fusion on the Z machine at Sandia National Laboratories. *Nuclear Fusion*, 62(4):042015, feb 2022.

[50] Fan Zhang and Jian Cheng. Analysis on physical-constraint-preserving high-order discontinuous Galerkin method for solving Kapila's five-equation model. *Journal of Computational Physics*, 492:112417, 2023.

[51] Jiahui Zhang, Yinhua Xia, and Yan Xu. Well-balanced path-conservative discontinuous Galerkin methods with equilibrium preserving space for two-layer shallow water equations. *Journal of Computational Physics*, 520:113473, 2025.

This page intentionally left blank.

APPENDIX A. Equivalence of Pelanti and Saurel Systems

In this appendix, we show the equivalence of the system of Saurel et al. [32] to that of Pelanti and Shuye [28]. Inserting the definition of E_k into Eqn. (2.1d):

$$\partial_t[\alpha_k\rho_k e_k + \frac{1}{2}\alpha_k\rho_k u^2] + \nabla\cdot\left[\boldsymbol{u}(\alpha_k\rho_k e_k + \frac{1}{2}\alpha_k\rho_k u^2 + \alpha_k p_k)\right] + \mathcal{Y}_k = -\sum_{j=1}^{N} p_{I,kj}\mu_{kj}(p_k - p_j). \tag{A.1}$$

Rearranging,

$$\begin{aligned}\partial_t[\alpha_k\rho_k e_k] + \nabla\cdot[\boldsymbol{u}\alpha_k\rho_k e_k] + \alpha_k p_k\nabla\cdot\boldsymbol{u} \\ + \partial_t[\frac{1}{2}\alpha_k\rho_k u^2] + \nabla\cdot\left[\boldsymbol{u}\frac{1}{2}\alpha_k\rho_k u^2\right] + \boldsymbol{u}\cdot\nabla\alpha_k p_k + \mathcal{Y}_k \\ = -\sum_{j=1}^{N} p_{I,kj}\mu_{kj}(p_k - p_j).\end{aligned} \tag{A.2}$$

Introducing the system from Saurel et al. [32]:

$$\partial_t[\alpha_k] + \boldsymbol{u}\cdot\nabla\alpha_k = \sum_{j=1}^{N}\mu_{kj}(p_k - p_j), \tag{A.3a}$$

$$\partial_t[\alpha_k\rho_k] + \nabla\cdot[\alpha_k\rho_k\boldsymbol{u}] = 0, \tag{A.3b}$$

$$\partial_t[\rho\boldsymbol{u}] + \nabla\cdot[\rho\boldsymbol{u}\otimes\boldsymbol{u} + p\boldsymbol{I}] = \boldsymbol{0}, \tag{A.3c}$$

$$\partial_t[\alpha_k\rho_k e_k] + \nabla\cdot[\boldsymbol{u}\alpha_k\rho_k e_k] + \alpha_k p_k\nabla\cdot\boldsymbol{u} = -\sum_{j=1}^{N} p_{I,kj}\mu_{kj}(p_k - p_j), \tag{A.3d}$$

we recognize that to arrive at Eqn. (A.3d), we need to show that the middle line of Eqn. (A.2) is zero. Examining this line alone,

$$\begin{aligned}\partial_t[\frac{1}{2}\alpha_k\rho_k u^2] + \nabla\cdot\left[\boldsymbol{u}\frac{1}{2}\alpha_k\rho_k u^2\right] + \boldsymbol{u}\cdot\nabla\alpha_k p_k + \mathcal{Y}_k = \\ \frac{1}{2}u^2\partial_t[\alpha_k\rho_k] + \frac{1}{2}u^2\nabla\cdot\boldsymbol{u}\alpha_k\rho_k \\ + \alpha_k\rho_k\boldsymbol{u}\cdot\partial_t\boldsymbol{u} + \alpha_k\rho_k\boldsymbol{u}\cdot\boldsymbol{u}\cdot\nabla\boldsymbol{u} + \boldsymbol{u}\cdot\nabla\alpha_k p_k + \mathcal{Y}_k.\end{aligned} \tag{A.4}$$

We recognize that the middle line, using Eqn. (2.1b), is zero. We also recognize that Eqn. (2.1c) can be rewritten as,

$$\partial_t\boldsymbol{u} + \boldsymbol{u}\cdot\nabla\boldsymbol{u} = -\frac{\nabla p}{\rho}. \tag{A.5}$$

Inserting this into Eqn. (A.4),

$$-\boldsymbol{u} \cdot [z_k \nabla p - \nabla \alpha_k p_k] + \mathcal{Y}_k = 0, \tag{A.6}$$

by the definition of $\mathcal{Y}_k$.

APPENDIX B. Riemann Solvers

In this appendix, we describe a few examples of approximate Riemann solvers used in this document, as well as the corresponding nonconservative flux terms (indicated using the $\widehat{()}$ notation), for the spatial-averaging discretization of Section 3.4. For convenience, the volume fraction equation for the spatial-averaging discretization is reproduced below:

$$\int_{\Omega_e} \phi_i^e \frac{\partial}{\partial t}\alpha_k d\Omega + \int_{\partial\Omega_e} \phi_i^e (\widehat{\alpha_k \vec{u}} - \overline{\alpha}_k \widehat{\vec{u}}) \cdot \vec{n} ds - \int_{\Omega_e} (\alpha_k - \overline{\alpha}_k)\vec{u} \cdot \nabla \phi_i^e d\Omega = 0, \tag{B.1}$$

and the phasic energy equation is reproduced below:

$$\int_{\Omega_e} \phi_i^e \frac{\partial}{\partial t}(\alpha_k \rho_k E_k) d\Omega + \int_{\partial\Omega_e} \phi_i^e [\vec{u}(\alpha_k \widehat{\rho_k E_k + \alpha_k p_k}) + \overline{z_k \vec{u}}\widehat{p} - \overline{\vec{u}}\widehat{\alpha_k p_k}] \cdot \vec{n} ds$$
$$- \int_{\Omega_e} [\vec{u}(\alpha_k \rho_k E_k + \alpha_k p_k) + \overline{z_k \vec{u}} p - \overline{\vec{u}} \alpha_k p_k] \cdot \nabla \phi_i^e d\Omega = 0. \tag{B.2}$$

Here we describe the numerical fluxes, assessed using Riemann solvers, $\widehat{\alpha_k \vec{u}}$ and $\vec{u}(\alpha_k \widehat{\rho_k E_k + \alpha_k p_k})$, as well as the other fluxes from the conservative subsystem of the six equation model of Eqns. (2.1), and the nonconservative fluxes $\widehat{\vec{u}}$, $\widehat{p}$, and $\widehat{\alpha_k p_k}$.

B.1. Local Lax-Friedrichs (LLF) Flux

The LLF flux [35, 22], among the simplest flux functions commonly used in finite volume and discontinuous Galerkin schemes, can be expressed as:

$$\widehat{\mathbf{f}} = \frac{1}{2}(\mathbf{f}_R + \mathbf{f}_L) - \frac{S}{2}(\mathbf{q}_R - \mathbf{q}_L), \tag{B.3}$$

where S is the largest (absolute) wavespeed in the system, and the notation $()_L$ and $()_R$ denote the left and right states across the element interface.

The nonconservative flux term in Eqn. (B.1) for well-balancedness is $\widehat{\vec{u}} = \frac{1}{2}(\vec{u}_L + \vec{u}_R)$. The nonconservative flux terms in Eqn. (B.2) are $\widehat{\alpha_k p_k} = \frac{1}{2}[(\alpha_k p_k)_L + (\alpha_k p_k)_R]$, and $\widehat{p} = \frac{1}{2}[p_L + p_R]$.

All of the results of Chapter 7 use the LLF flux.

B.2. Harten-Lax-van Leer (HLL) Flux

The HLL flux [17] models the fastest left and right-running waves in the system. This can be expressed as:

$$\widehat{\mathbf{f}} = \begin{cases} \mathbf{f}_L & \text{if } 0 \leq S_L \\ \frac{S_R \mathbf{f}_L - S_L \mathbf{f}_R + S_L S_R (\mathbf{q}_R - \mathbf{q}_L)}{S_R - S_L} & \text{if } S_L \leq 0 \leq S_R \\ \mathbf{f}_R & \text{if } S_R \leq 0 \end{cases}, \tag{B.4}$$

where S_L and S_R are the maximum left and right-running wavespeeds in the system, estimated using the formulae of Davis [13], $S_L = \min(u_L - c_L, u_R - c_R)$, $S_R = \max(u_L + c_L, u_R + c_R)$.

The nonconservative flux term in Eqn. (B.1) for well-balancedness is,

$$\widehat{\vec{u}} = \begin{cases} \vec{u}_L & \text{if } 0 \leq S_L \\ \frac{S_R \vec{u}_L - S_L \vec{u}_R}{S_R - S_L} & \text{if } S_L \leq 0 \leq S_R \\ \vec{u}_R & \text{if } S_R \leq 0 \end{cases}. \tag{B.5}$$

The nonconservative flux terms in Eqn. (B.2) are,

$$\widehat{\alpha_k p_k} = \begin{cases} (\alpha_k \rho_k)_L & \text{if } 0 \leq S_L \\ \frac{S_R (\alpha_k \rho_k)_L - S_L (\alpha_k \rho_k)_R}{S_R - S_L} & \text{if } S_L \leq 0 \leq S_R \\ (\alpha_k \rho_k)_R & \text{if } S_R \leq 0 \end{cases}, \tag{B.6}$$

and

$$\widehat{p} = \begin{cases} p_L & \text{if } 0 \leq S_L \\ \frac{S_R p_L - S_L p_R}{S_R - S_L} & \text{if } S_L \leq 0 \leq S_R \\ p_R & \text{if } S_R \leq 0 \end{cases}. \tag{B.7}$$

Results using the HLL flux for the sharp interface advection problem of Section 7.6 are shown in Figure B-1. These results demonstrate that the HLL flux is well-balanced. Additionally, we show results for the problems of Sections 7.11, 7.12, and 7.13 in Figures B-2, B-3, and B-4.

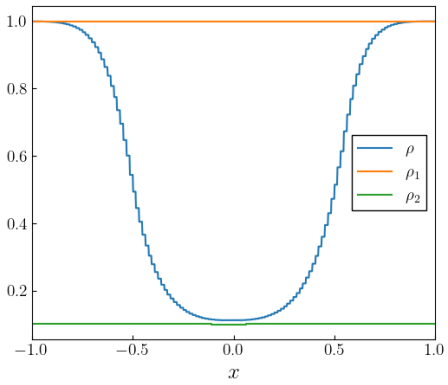

Density

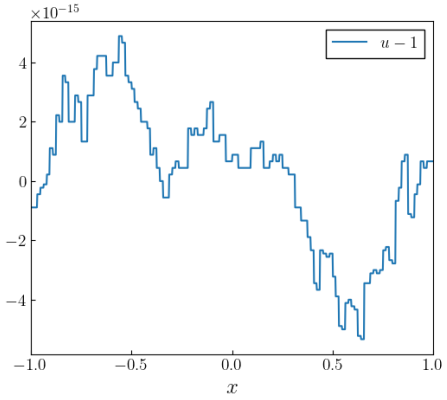

Velocity error

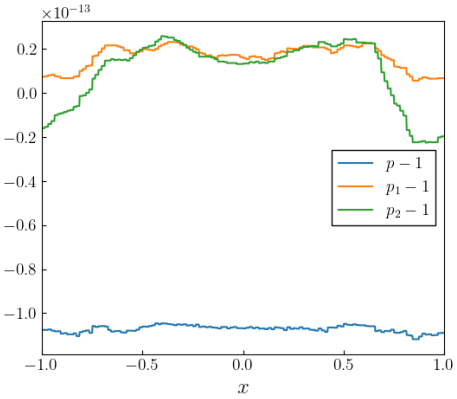

Pressure error

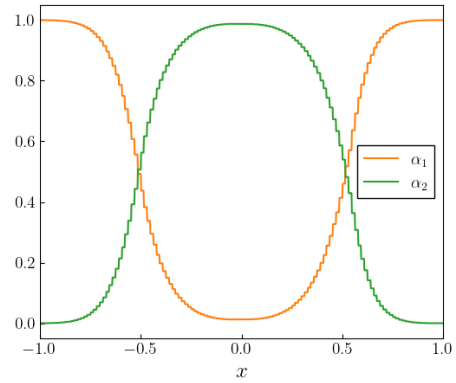

Volume fraction

Figure B-1. Primitive variable error profiles (b) and (c) and profiles (a) and (d) for the sharp 1-D interface advection problem (Config. 2) after 1 period using the spatial-averaging discretization (Section 3.4) with the HLL numerical flux.

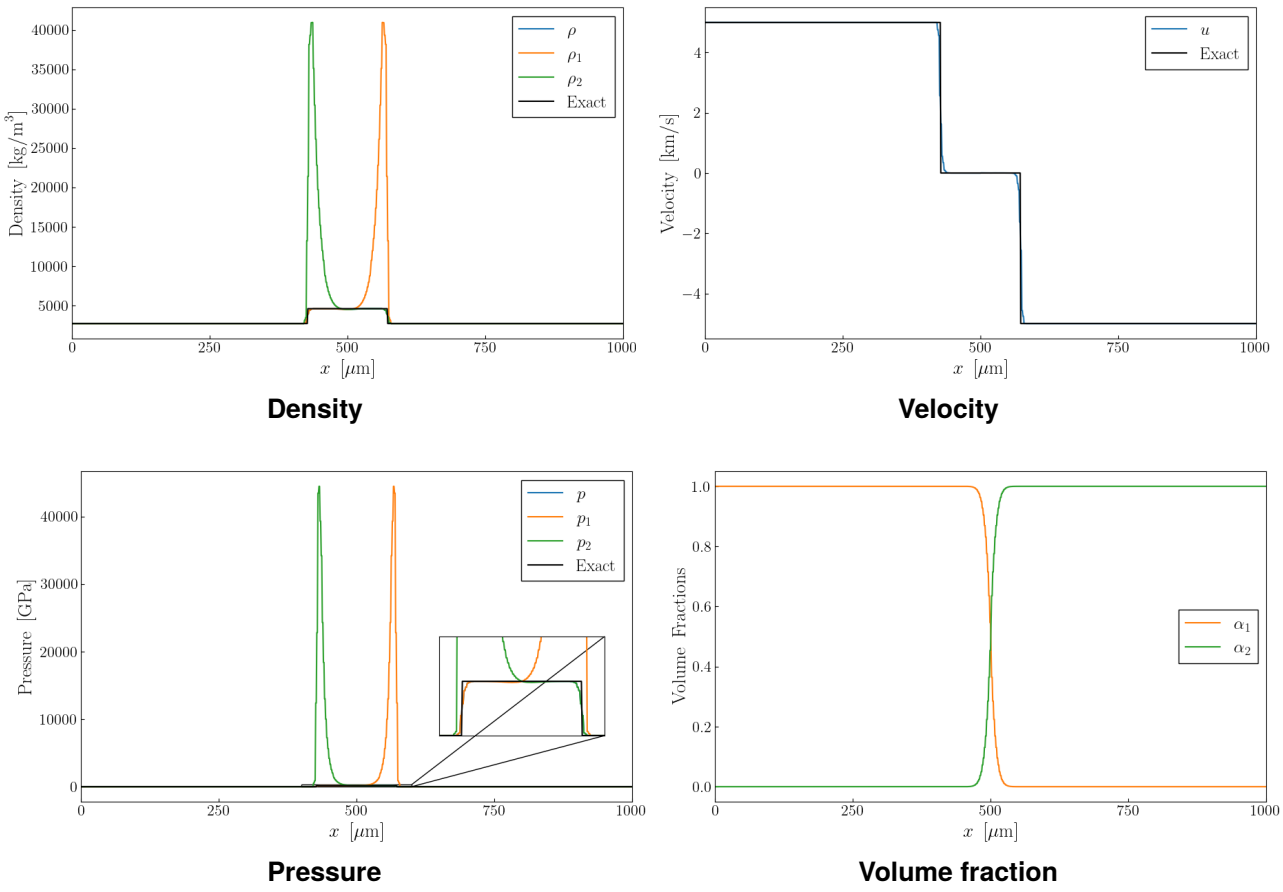

Figure B-2. Primitive variable profiles for the 1-D Al-Al collision problem at $t = 0.1$ s using the spatial-averaging discretization (Section 3.4) with the HLL numerical flux.

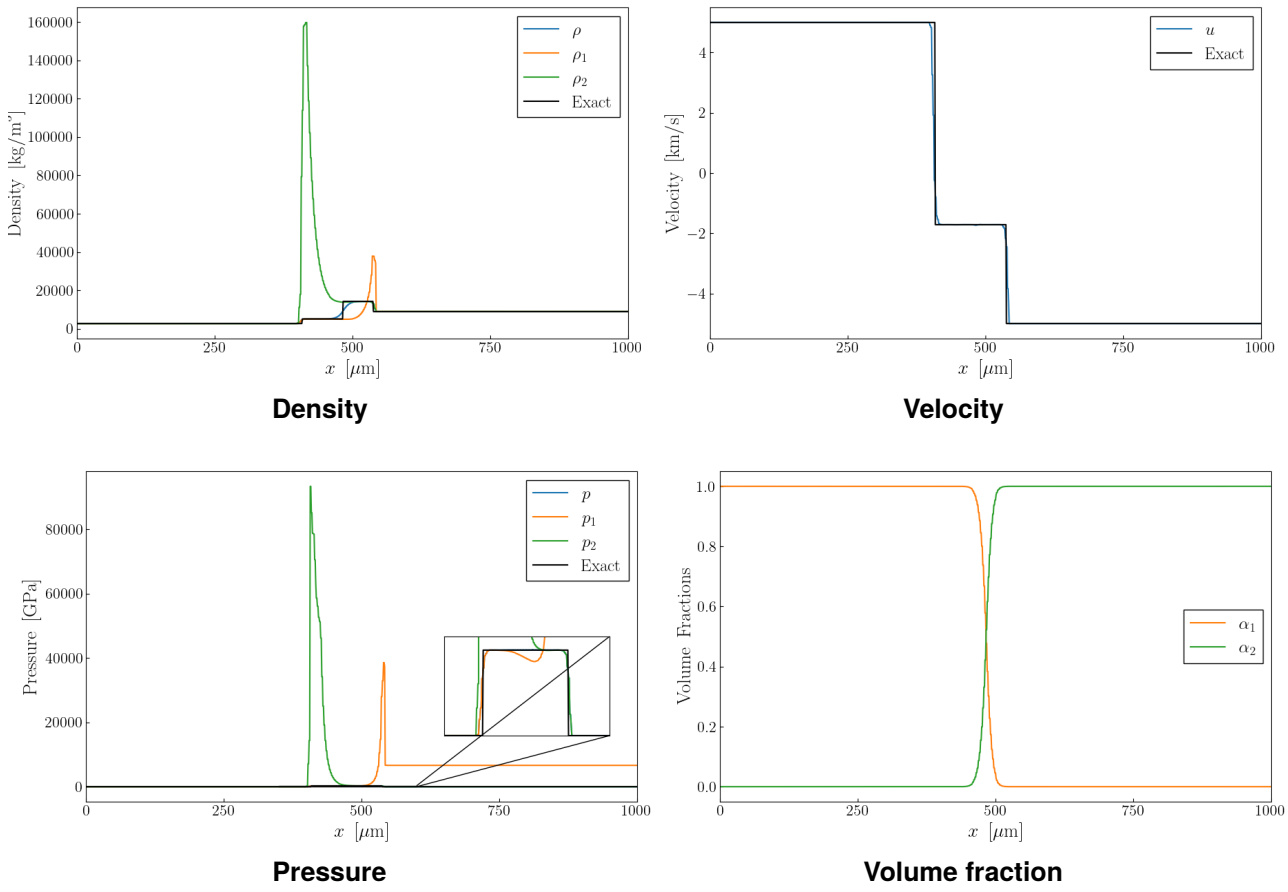

Figure B-3. Primitive variable profiles for the 1-D Al-Cu collision problem at $t = 0.1$ s using the spatial-averaging discretization (Section 3.4) with the HLL numerical flux.

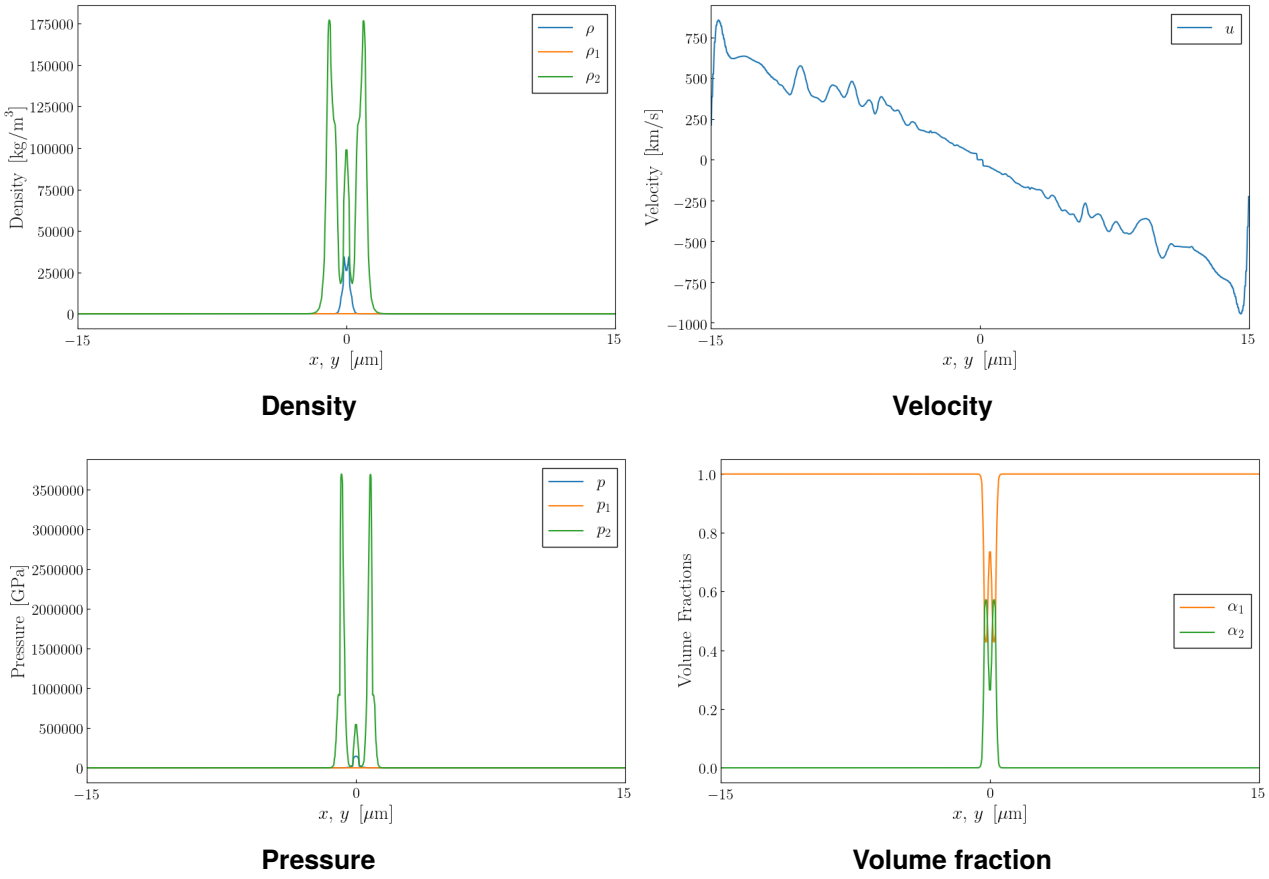

Figure B-4. Primitive variable profiles for the 2-D XMHD liner implosion problem along $x = y$ at $t = 110$ ns using the spatial-averaging discretization (Section 3.4) with the HLL numerical flux.

B.3. Harten-Lax-van Leer-Contact (HLLC) Flux

The HLLC flux function [43] adds the contact wave to the system of the HLL solver of Section B.2. This can be expressed as:

$$\widehat{\mathbf{f}} = \begin{cases} \mathbf{f}_L & \text{if } 0 \le S_L \\ \mathbf{f}_L^* & \text{if } S_L \le 0 \le S^* \\ \mathbf{f}_R^* & \text{if } S^* \le 0 \le S_R \\ \mathbf{f}_R & \text{if } S_R \le 0 \end{cases}, \tag{B.8}$$

where the $()^*$ region flux is given, in 1-D, for the state variables of System (2.1), by Pelanti and Shuye [28] as

$$\mathbf{f}_\ell^* = \begin{bmatrix} (\alpha_k)_\ell \\ (\alpha_k\rho_k)_\ell \frac{S_\ell - u_\ell}{S_\ell - S^*} \\ \rho_\ell \frac{S_\ell - u_\ell}{S_\ell - S^*} S^* \\ \frac{S_\ell - u_\ell}{S_\ell - S^*} \left[(\alpha_k\rho_k E_k)_\ell + (S^* - u_\ell)(S^* + \frac{(\alpha_k p_k)_\ell}{S_\ell - u_\ell}) \right] \end{bmatrix} \tag{B.9}$$

with $\ell = L, R$, where the contact speed is

$$S^* = \frac{p_R - p_L + \rho_L u_L (S_L - u_L) - \rho_R u_R (S_R - u_R)}{\rho_L (S_L - u_L) - \rho_R (S_R - u_R)}. \tag{B.10}$$

In multi-dimensional simulations, u should be replaced with the normally directed velocity and the star-region flux of the transverse momentum components are $(\rho v)_\ell \frac{S_\ell - u_\ell}{S_\ell - S^*}$.

The nonconservative flux term in Eqn. (B.1) for well-balancedness is,

$$\widehat{\vec{u}} = \begin{cases} \vec{u}_L & \text{if } 0 \le S_L \\ \vec{u}_L & \text{if } S_L \le 0 \le S^* \\ \vec{u}_R & \text{if } S^* \le 0 \le S_R \\ \vec{u}_R & \text{if } S_R \le 0 \end{cases}. \tag{B.11}$$

The nonconservative flux terms in Eqn. (B.2) are,

$$\widehat{\alpha_k p_k} = \begin{cases} (\alpha_k p_k)_L & \text{if } 0 \le S_L \\ (\alpha_k p_k)_L & \text{if } S_L \le 0 \le S^* \\ (\alpha_k p_k)_R & \text{if } S^* \le 0 \le S_R \\ (\alpha_k p_k)_R & \text{if } S_R \le 0 \end{cases}, \tag{B.12}$$

and

$$\widehat{p} = \begin{cases} p_L & \text{if } 0 \le S_L \\ p_L & \text{if } S_L \le 0 \le S^* \\ p_R & \text{if } S^* \le 0 \le S_R \\ p_R & \text{if } S_R \le 0 \end{cases}. \tag{B.13}$$

Results using the HLLC flux for the sharp interface advection problem of Section 7.6 are shown in Figure B-5. These results demonstrate that the HLLC flux is well-balanced. Additionally, we show results for the problems of Sections 7.11, 7.12, and 7.13 in Figures B-6, B-8, and B-9.

The results for the symmetric Al-Al collision problem in Figure B-6 and the symmetric 2-D liner implosion problem in Figure B-9 reveal a fundamental issue of the HLLC solver. Namely, the inequality logic of the HLLC solver in choosing wave regions does not make a decisive choice for the case $S^* = 0$, which is the case in the center of the domain for the symmetric Al-Al collision problem. This can be fixed by employing a small threshold ϵ, here we choose $\epsilon = 1 \times 10^{-11}$, below which S^* is set exactly to zero. Then, the inequalities involving S^* can be made exclusive, and an additional criterion specified. For the flux,

$$\widehat{\mathbf{f}} = \frac{1}{2}(\mathbf{f}_L^* + \mathbf{f}_R^*) \text{ if } S^* = 0, \tag{B.14}$$

and for the nonconservative flux term in Eqn. (B.1),

$$\widehat{\vec{u}} = \frac{1}{2}(\vec{u}_L + \vec{u}_R) \text{ if } S^* = 0. \tag{B.15}$$

For the nonconservative flux terms in Eqn. (B.2),

$$\widehat{\alpha_k p_k} = \frac{1}{2}\left[(\alpha_k p_k)_L + (\alpha_k p_k)_R\right] \text{ if } S^* = 0, \tag{B.16}$$

and,

$$\widehat{p_k} = \frac{1}{2}\left[p_L + p_R\right] \text{ if } S^* = 0. \tag{B.17}$$

This approach is also guaranteed mathematically to be well-balanced. The results for the Al-Al collision problem using this approach are depicted in Figure B-7. They are obviously symmetric.

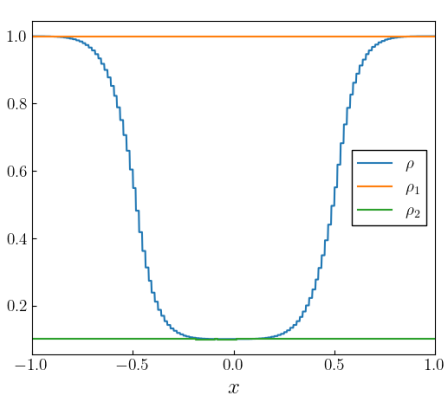

Density

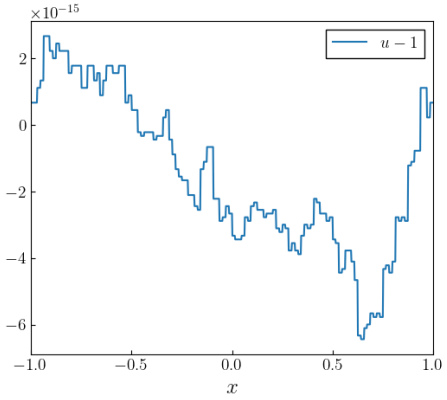

Velocity error

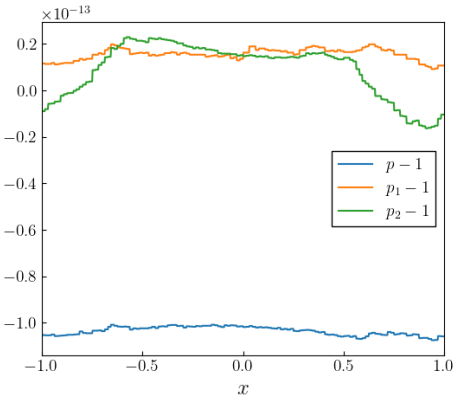

Pressure error

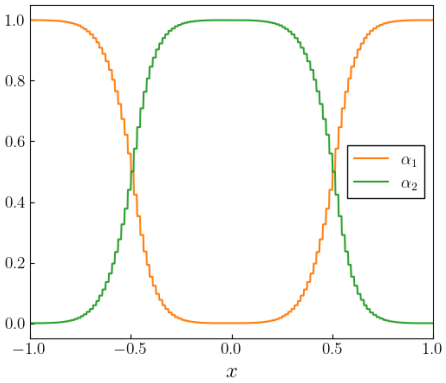

Volume fraction

Figure B-5. Primitive variable error profiles (b) and (c) and profiles (a) and (d) for the sharp 1-D interface advection problem (Config. 2) after 1 period using the spatial-averaging discretization (Section 3.4) with the HLLC numerical flux.

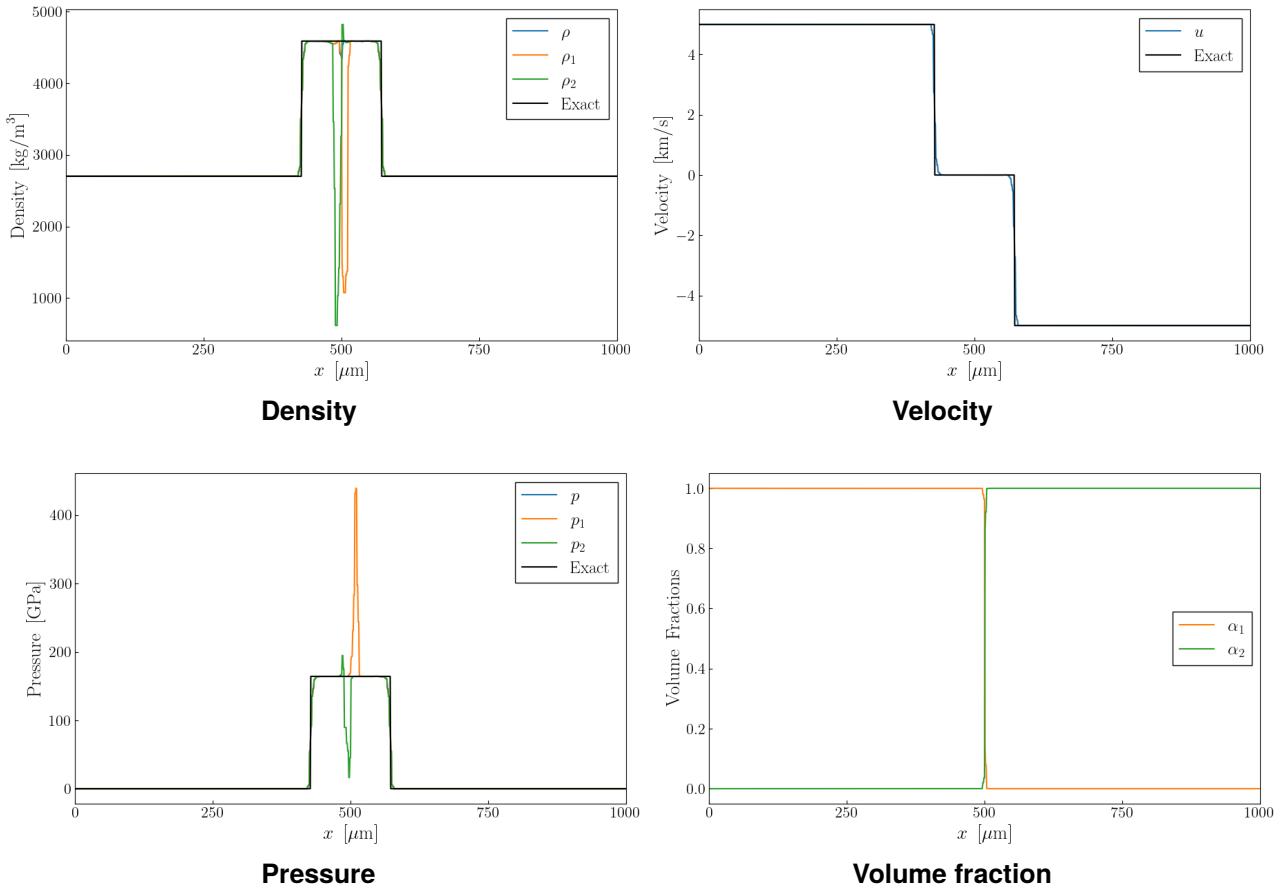

Figure B-6. Primitive variable profiles for the 1-D Al-Al collision problem at $t = 0.1$ s using the spatial-averaging discretization (Section 3.4) with the HLLC numerical flux.

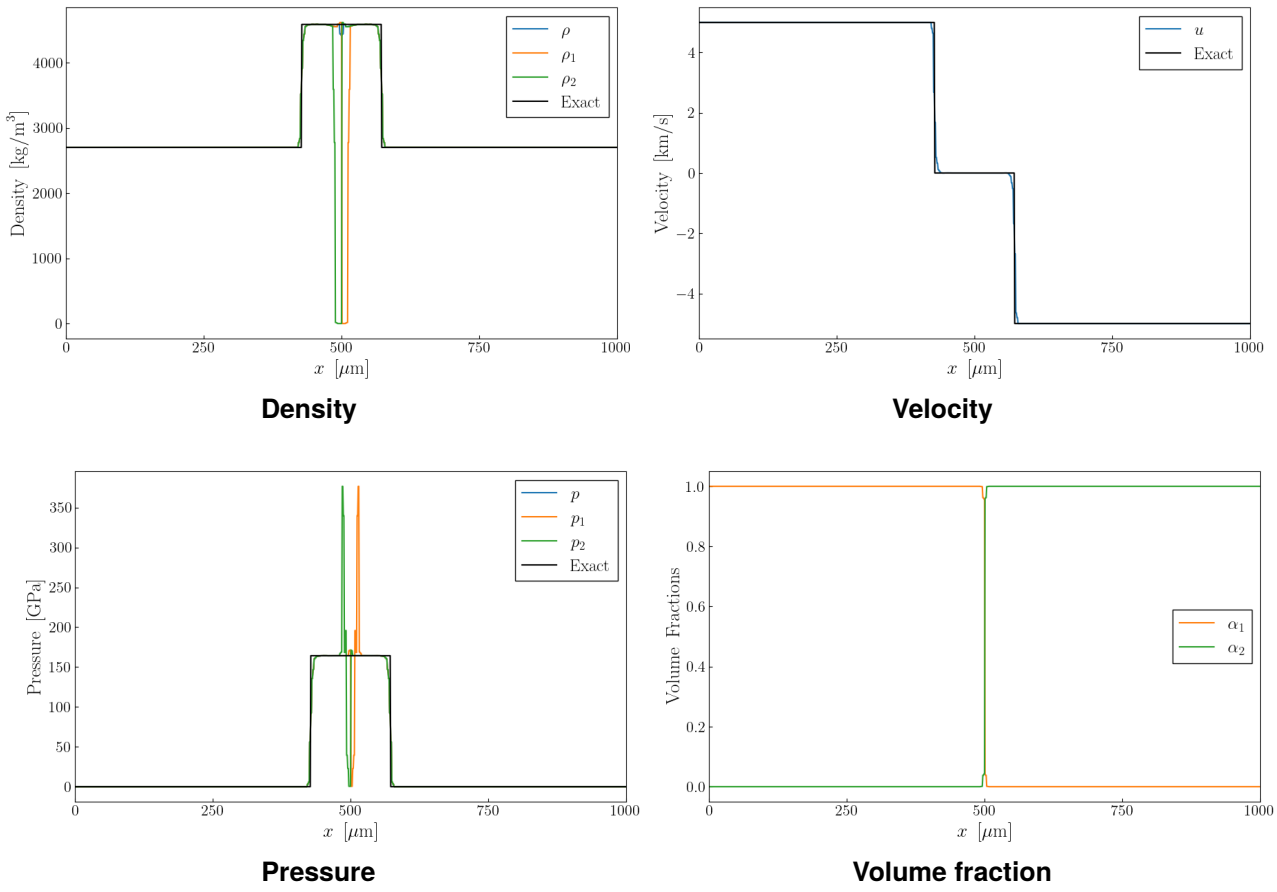

Figure B-7. Primitive variable profiles for the 1-D Al-Al collision problem at $t = 0.1$ s using the spatial-averaging discretization (Section 3.4) with the symmetric HLLC numerical flux.

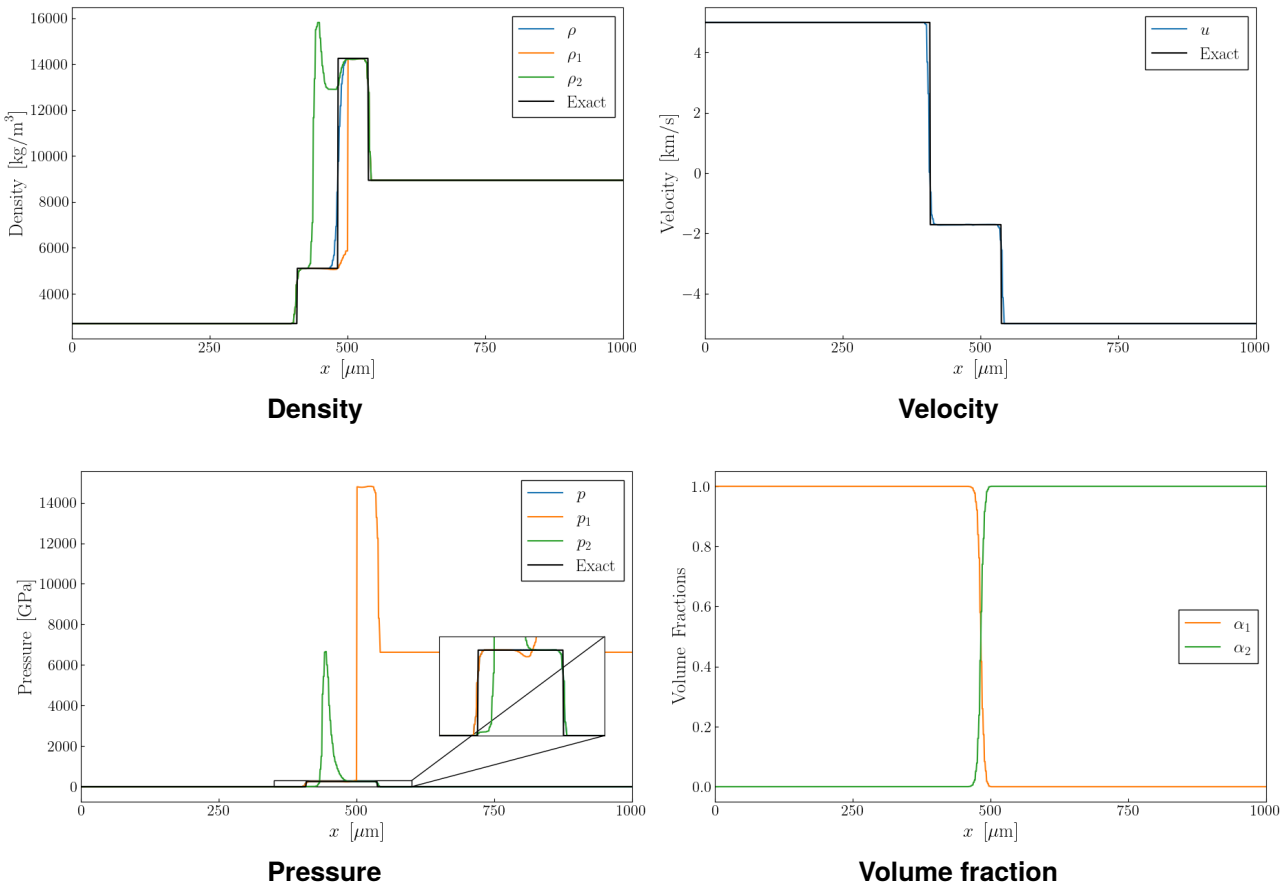

Figure B-8. Primitive variable profiles for the 1-D Al-Cu collision problem at $t = 0.1$ s using the spatial-averaging discretization (Section 3.4) with the HLLC numerical flux.

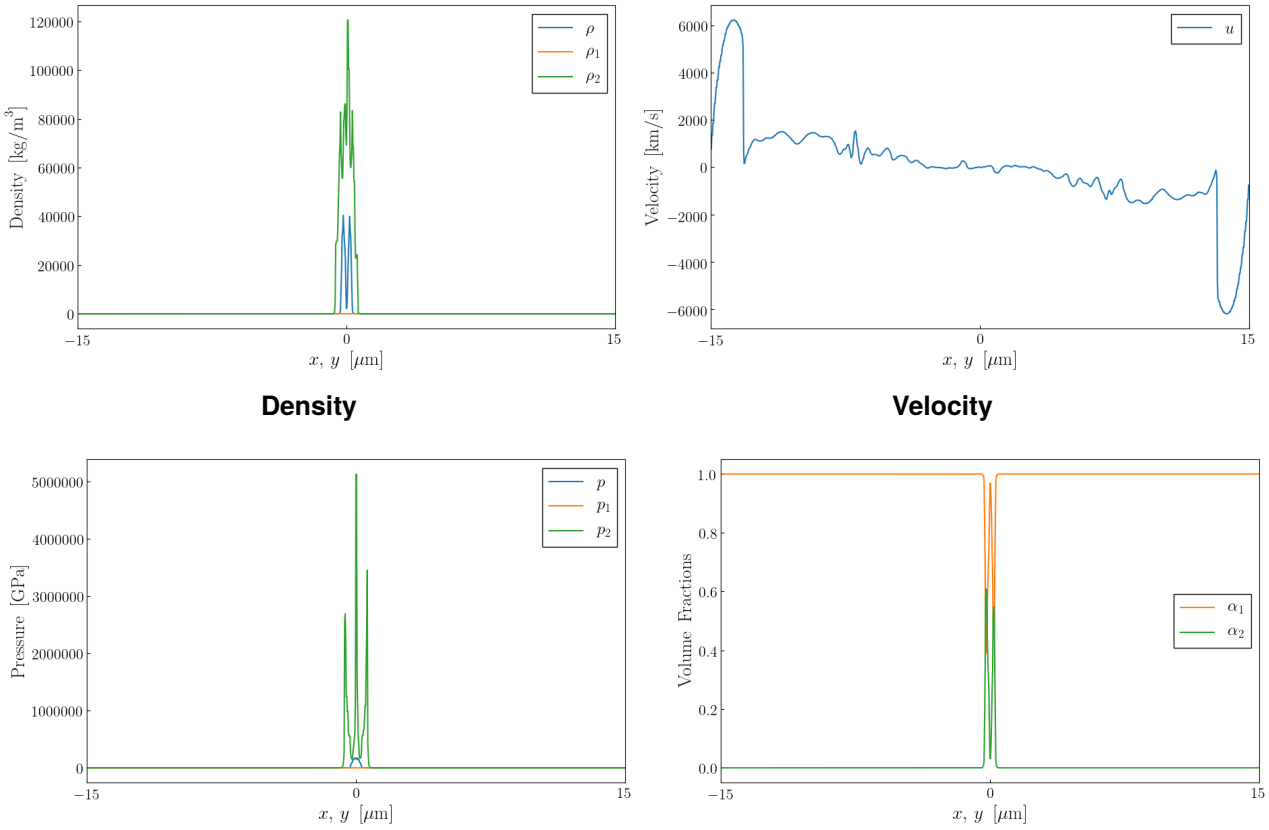

Figure B-9. Primitive variable profiles for the 2-D XMHD liner implosion problem along $x = y$ at $t = 110$ ns using the spatial-averaging discretization (Section 3.4) with the HLLC numerical flux.

B.4. Roe Flux

The Roe flux [34] linearizes the flux Jacobian matrix of the hyperbolic system and advects wave-by-wave the appropriate quantities about each linearized state. The Roe flux can be generally expressed as,

$$\widehat{\mathbf{f}} = \frac{1}{2}(\mathbf{f}_L + \mathbf{f}_R) - \frac{1}{2}\sum_{n=1}^{N_w} |\hat{\lambda}_n| \hat{W}_n \hat{\mathbf{r}}_n \tag{B.18}$$

where N_w is the number of distinct waves in the system, with each of which is associated an eigenvalue λ_n and a right eigenvector $\mathbf{r}_n$ of the flux Jacobian matrix, as well as a wave strength W_n. The $\hat{()}$ notation denotes that these quantities are evaluated at the Roe-averaged state.

Pelanti and Shuye [28] provide the flux Jacobian, the Roe-averaged state, and the diagonalization quantities for the state variables of System (2.1) in 1-D, with only two materials described by the stiffened gas EOS. In 1-D, the system can be written as,

$$\frac{\partial}{\partial t}\mathbf{q} + \frac{\partial}{\partial x}\mathbf{f}(\mathbf{q}) + \mathbf{d}(\mathbf{q}, \frac{\partial}{\partial x}\mathbf{q}) = 0, \tag{B.19}$$

with

$$\mathbf{q} = \begin{bmatrix} \alpha_1\rho_1 \\ \alpha_2\rho_2 \\ \rho u \\ \alpha_1 E_1 \\ \alpha_2 E_2 \\ \alpha_1 \end{bmatrix}, \quad \mathbf{f} = \begin{bmatrix} \alpha_1\rho_1 u \\ \alpha_2\rho_2 u \\ \rho u^2 + p \\ u[\alpha_1 E_1 + \alpha_1 p_1] \\ u[\alpha_2 E_2 + \alpha_2 p_2] \\ 0 \end{bmatrix}, \quad \mathbf{d} = \begin{bmatrix} 0 \\ 0 \\ 0 \\ u[z_1 \frac{\partial}{\partial x} p - \frac{\partial}{\partial x}(\alpha_1 p_1)] \\ u[z_2 \frac{\partial}{\partial x} p - \frac{\partial}{\partial x}(\alpha_2 p_2)] \\ u\frac{\partial}{\partial x}\alpha_1 \end{bmatrix}, \tag{B.20}$$

where the second volume fraction need not be explicitly advected, as it can be calculated by $\alpha_2 = 1 - \alpha_1$. This system can be re-written as,

$$\frac{\partial}{\partial t}\mathbf{q} + \mathbf{A}\frac{\partial}{\partial x}\mathbf{q} = 0, \tag{B.21}$$

where the flux Jacobian matrix $\mathbf{A}$ includes contributions from the conservative and non-conservative terms, $\mathbf{A} = \frac{\partial \mathbf{f}}{\partial \mathbf{q}} + D$. The right eigenvectors of the Roe matrix (i.e., Roe-averaged Jacobian matrix) $\hat{\mathbf{A}} = \mathbf{A}(\hat{\mathbf{q}})$ are,

$$\hat{\mathbf{R}} = [\hat{\mathbf{r}}_1, \hat{\mathbf{r}}_2, ..., \hat{\mathbf{r}}_6] = \begin{bmatrix} \hat{z}_1 & \hat{z}_1 & 0 & 0 & 1 & 0 \\ \hat{z}_2 & \hat{z}_2 & 0 & 1 & 0 & 0 \\ \hat{u} - \hat{c} & \hat{u} + \hat{c} & 0 & \hat{u} & \hat{u} & 0 \\ \widehat{z_1 H_1} - \widetilde{uz_1}\hat{c} & \widehat{z_1 H_1} + \widetilde{uz_1}\hat{c} & -\frac{\kappa_2}{\kappa_1} & -\frac{\chi_2}{\kappa_1} + \frac{\kappa_2}{\kappa_1}\frac{\hat{u}^2}{2} & -\frac{\chi_1}{\kappa_1} + \frac{\hat{u}^2}{2} & \frac{\pi_1 - \pi_2}{\kappa_1} \\ \widehat{z_2 H_2} - \widetilde{uz_2}\hat{c} & \widehat{z_2 H_2} + \widetilde{uz_2}\hat{c} & 1 & 0 & 0 & 0 \\ 0 & 0 & 0 & 0 & 0 & 1 \end{bmatrix}. \tag{B.22}$$

Here $\kappa_k = \frac{\partial p_k(\mathcal{E}_k, \rho_k)}{\partial \mathcal{E}_k}$, and $\chi_k = \frac{\partial p_k(\mathcal{E}_k, \rho_k)}{\partial \rho_k}$, which are constants in the stiffened gas case presented in the reference, and $H_k = \frac{E_k + p_k}{\rho_k}$. The presence of the π_k terms is due to the constant in the stiffened

gas equation of state, which introduces additional terms in products of $\alpha_k p_k$ that depend directly on α_k. The Roe-averaged eigenvalues are given by,

$$\hat{\lambda}_1 = \hat{u} - \hat{c}, \hat{\lambda}_2 = \hat{u} + \hat{c}, \quad \hat{\lambda}_3 = \hat{\lambda}_4 = \hat{\lambda}_5 = \hat{\lambda}_6 = \hat{u}. \tag{B.23}$$

The Roe-averaged wave-strengths are defined as,

$$\begin{aligned}
\hat{W}_1 &= \frac{\Delta(\alpha_1 p_1 + \alpha_2 p_2) - \hat{c}\sqrt{\rho_L \rho_R}\Delta u}{2\hat{c}^2}, \quad \hat{W}_2 = \frac{\Delta(\alpha_1 p_1 + \alpha_2 p_2) + \hat{c}\sqrt{\rho_L \rho_R}\Delta u}{2\hat{c}^2}, \\
\hat{W}_3 &= -\frac{\Delta(\alpha_1 p_1 + \alpha_2 p_2)}{\hat{c}^2}\widehat{z_2 H_2} + \frac{\hat{u}^2}{2}\Delta(\alpha_2\rho_2) + \Delta(\alpha_2\rho_2 e_2), \\
\hat{W}_4 &= \Delta(\alpha_2\rho_2) - \hat{z}_2\frac{\Delta(\alpha_1 p_1 + \alpha_2 p_2)}{\hat{c}^2}, \quad \hat{W}_5 = \Delta(\alpha_1\rho_1) - \hat{z}_1\frac{\Delta(\alpha_1 p_1 + \alpha_2 p_2)}{\hat{c}^2}, \\
\hat{W}_6 &= \Delta\alpha_1.
\end{aligned} \tag{B.24}$$

The Roe-averaged variables are defined as,

$$\begin{aligned}
\hat{u} &= \frac{u_L\sqrt{\rho_L} + u_R\sqrt{\rho_R}}{\sqrt{\rho_L} + \sqrt{\rho_R}}, \quad \hat{z}_k = \frac{z_{kL}\sqrt{\rho_L} + z_{kR}\sqrt{\rho_R}}{\sqrt{\rho_L} + \sqrt{\rho_R}}, \quad \widehat{uz_k} = \frac{(uz_k)_L\sqrt{\rho_L} + (uz_k)_R\sqrt{\rho_R}}{\sqrt{\rho_L} + \sqrt{\rho_R}}, \\
\widehat{uz_k} &= \frac{1}{2}(\hat{u}\hat{z}_k + \widehat{uz_k}), \quad \widehat{z_k H_k} = \frac{(z_k H_k)_L\sqrt{\rho_L} + (z_k H_k)_R\sqrt{\rho_R}}{\sqrt{\rho_L} + \sqrt{\rho_R}}, \quad \hat{c} = \sqrt{\widetilde{z_1 c_1^2} + \widetilde{z_2 c_2^2}}, \\
\widetilde{z_k c_k^2} &= \kappa_k(\widehat{z_k H_k} - \frac{\hat{u}}{2}\hat{z}_k) + \chi_k\hat{z}_k.
\end{aligned} \tag{B.25}$$

However, to be useful in the FLEXO code, we require a 3-D Roe solver for an arbitrary number of materials described by an arbitrary (i.e., tabular) equation of state. Thus, we extend this Roe solver to match the requirements of the FLEXO code.

As the quantity entering the DG weak form is actually the normally directed flux (via the dot product with the outward-facing normal vector), we change the coordinates from the Cartesian coordinates $\vec{x}$ to $\vec{x}_n$,

$$\vec{x} = [x, y, z], \quad \vec{x}_n = [x_n, x_{t_1}, x_{t_2}], \tag{B.26}$$

where n denotes the normal direction, t_1 a tangential direction, and t_2 a second, orthogonal tangential direction chosen such that this tuple comprises a right-handed coordinate system. In this coordinate frame, we write the velocity vector as $\vec{u}_n$, the flux as $\vec{\mathbf{f}}_n$, and the del operator as $\vec{\nabla}_n$,

$$\vec{u}_n = [u_n, u_{t_1}, u_{t_2}], \quad \vec{\mathbf{f}}_n = [\mathbf{f}_n, \mathbf{f}_{t_1}, \mathbf{f}_{t_2}], \quad \vec{\nabla}_n() = \hat{x}_n\frac{\partial}{\partial x_n}() + \hat{x}_{t_1}\frac{\partial}{\partial x_{t_1}}() + \hat{x}_{t_2}\frac{\partial}{\partial x_{t_2}}(). \tag{B.27}$$

As FLEXO uses structured meshes, the normal and tangential directions always align with some permutation of the Cartesian coordinates. Our system, then, can be written,

$$\frac{\partial}{\partial t}\mathbf{q} + \nabla_n \cdot \mathbf{f}(\mathbf{q}) + \mathbf{d}(\mathbf{q}, \nabla_n\mathbf{q}) = 0, \tag{B.28}$$

where, for an arbitrary N_m number of materials, the state vector is given as,

$$\mathbf{q} = \begin{bmatrix} \alpha_1\rho_1 \\ \alpha_2\rho_2 \\ \vdots \\ \alpha_{N_m}\rho_{N_m} \\ \rho u_n \\ \rho u_{t_1} \\ \rho u_{t_2} \\ \alpha_1 E_1 \\ \alpha_2 E_2 \\ \vdots \\ \alpha_{N_m} E_{N_m} \\ \alpha_1 \\ \alpha_2 \\ \vdots \\ \alpha_{N_m} \end{bmatrix}, \tag{B.29}$$

the flux vectors are given as,

$$\mathbf{f}_n = \begin{bmatrix} \alpha_1\rho_1 u_n \\ \alpha_2\rho_2 u_n \\ \vdots \\ \alpha_{N_m}\rho_{N_m} u_n \\ \rho u_n^2 + p \\ \rho u_n u_{t_1} \\ \rho u_n u_{t_2} \\ u_n[\alpha_1 E_1 + \alpha_1 p_1] \\ u_n[\alpha_2 E_2 + \alpha_2 p_2] \\ \vdots \\ u_n[\alpha_{N_m} E_{N_m} + \alpha_{N_m} p_{N_m}] \\ 0 \\ 0 \\ \vdots \\ 0 \end{bmatrix}, \quad \mathbf{f}_{t_1} = \begin{bmatrix} \alpha_1\rho_1 u_{t_1} \\ \alpha_2\rho_2 u_{t_1} \\ \vdots \\ \alpha_{N_m}\rho_{N_m} u_{t_1} \\ \rho u_{t_1} u_n \\ \rho u_{t_1}^2 + p \\ \rho u_{t_1} u_{t_2} \\ u_{t_1}[\alpha_1 E_1 + \alpha_1 p_1] \\ u_{t_1}[\alpha_2 E_2 + \alpha_2 p_2] \\ \vdots \\ u_{t_1}[\alpha_{N_m} E_{N_m} + \alpha_{N_m} p_{N_m}] \\ 0 \\ 0 \\ \vdots \\ 0 \end{bmatrix}, \quad \mathbf{f}_{t_2} = \begin{bmatrix} \alpha_1\rho_1 u_{t_2} \\ \alpha_2\rho_2 u_{t_2} \\ \vdots \\ \alpha_{N_m}\rho_{N_m} u_{t_2} \\ \rho u_{t_2} u_n \\ \rho u_{t_2} u_{t_1} \\ \rho u_{t_2}^2 + p \\ u_{t_2}[\alpha_1 E_1 + \alpha_1 p_1] \\ u_{t_2}[\alpha_2 E_2 + \alpha_2 p_2] \\ \vdots \\ u_{t_2}[\alpha_{N_m} E_{N_m} + \alpha_{N_m} p_{N_m}] \\ 0 \\ 0 \\ \vdots \\ 0 \end{bmatrix}, \tag{B.30}$$

and the nonconservative vector is given as,

$$\mathbf{d} = \begin{bmatrix} 0 \\ 0 \\ \vdots \\ 0 \\ 0 \\ 0 \\ 0 \\ \vec{u}_n \cdot [z_1 \vec{\nabla}_n p - \vec{\nabla}_n (\alpha_1 p_1)] \\ \vec{u}_n \cdot [z_2 \vec{\nabla}_n p - \vec{\nabla}_n (\alpha_2 p_2)] \\ \vdots \\ \vec{u}_n \cdot [z_{N_m} \vec{\nabla}_n p - \vec{\nabla}_n (\alpha_{N_m} p_{N_m})] \\ \vec{u}_n \cdot \vec{\nabla}_n \alpha_1 \\ \vec{u}_n \cdot \vec{\nabla}_n \alpha_2 \\ \vdots \\ \vec{u}_n \cdot \vec{\nabla}_n \alpha_{N_m} \end{bmatrix}. \tag{B.31}$$

The quasi-linear form of this system can be written as,

$$\frac{\partial}{\partial t}\mathbf{q} + \mathbf{A}_n \frac{\partial}{\partial x_n}\mathbf{q} + \mathbf{A}_{t_1} \frac{\partial}{\partial x_{t_1}}\mathbf{q} + + \mathbf{A}_{t_2} \frac{\partial}{\partial x_{t_2}}\mathbf{q} = 0. \tag{B.32}$$

Because the normal-directed component of the flux, $\hat{n} \cdot \vec{\mathbf{f}}_n = \mathbf{f}_n$ is all that enters the DG weak form, we only consider the eigensystem of the normal-directed flux Jacobian, $\mathbf{A}_n$. The Roe-averaged eigenvectors of this Jacobian are, for the left and right-running acoustic waves,

$$\hat{\mathbf{r}}_1 = \begin{bmatrix} \hat{z}_1 \\ \hat{z}_2 \\ \vdots \\ \hat{z}_{N_m} \\ \hat{u}_n - \hat{c} \\ \hat{u}_{t_1} \\ \hat{u}_{t_2} \\ \widehat{z_1 H_1} - \widetilde{u_n z_1}\hat{c} \\ \widehat{z_2 H_2} - \widetilde{u_n z_2}\hat{c} \\ \vdots \\ \widehat{z_{N_m} H_{N_m}} - \widetilde{u_n z_{N_m}}\hat{c} \\ 0 \\ 0 \\ \vdots \\ 0 \end{bmatrix}, \quad \hat{\mathbf{r}}_2 = \begin{bmatrix} \hat{z}_1 \\ \hat{z}_2 \\ \vdots \\ \hat{z}_{N_m} \\ \hat{u}_n + \hat{c} \\ \hat{u}_{t_1} \\ \hat{u}_{t_2} \\ \widehat{z_1 H_1} + \widetilde{u_n z_1}\hat{c} \\ \widehat{z_2 H_2} + \widetilde{u_n z_2}\hat{c} \\ \vdots \\ \widehat{z_{N_m} H_{N_m}} + \widetilde{u_n z_{N_m}}\hat{c} \\ 0 \\ 0 \\ \vdots \\ 0 \end{bmatrix}, \tag{B.33}$$

for the N_m number of contact waves,

$$\hat{\mathbf{r}}_3 = \begin{bmatrix} 1 \\ 0 \\ \vdots \\ 0 \\ \hat{u}_n \\ 0 \\ 0 \\ -\frac{\chi_1}{\kappa_1} + \hat{K} - \hat{u}_{t_1}\frac{\hat{V}_{t_1}}{\kappa_1} - \hat{u}_{t_2}\frac{\hat{V}_{t_2}}{\kappa_1} \\ 0 \\ \vdots \\ 0 \\ 0 \\ 0 \\ \vdots \\ 0 \end{bmatrix}, \tag{B.34}$$

as well as,

$$\hat{\mathbf{r}}_4 = \begin{bmatrix} 0 \\ 1 \\ \vdots \\ 0 \\ \hat{u} \\ 0 \\ 0 \\ -\frac{\chi_2}{\kappa_1} + \frac{\kappa_2}{\kappa_1}\hat{K} - \hat{u}_{t_1}\frac{\hat{V}_{t_1}}{\kappa_1} - \hat{u}_{t_2}\frac{\hat{V}_{t_2}}{\kappa_1} \\ 0 \\ \vdots \\ 0 \\ 0 \\ 0 \\ \vdots \\ 0 \end{bmatrix}, \quad \ldots, \quad \hat{\mathbf{r}}_{2+N_m} = \begin{bmatrix} 0 \\ 0 \\ \vdots \\ 1 \\ \hat{u} \\ 0 \\ 0 \\ -\frac{\chi_{N_m}}{\kappa_1} + \frac{\kappa_{N_m}}{\kappa_1}\hat{K} - \hat{u}_{t_1}\frac{\hat{V}_{t_1}}{\kappa_1} - \hat{u}_{t_2}\frac{\hat{V}_{t_2}}{\kappa_1} \\ 0 \\ \vdots \\ 0 \\ 0 \\ 0 \\ \vdots \\ 0 \end{bmatrix}, \tag{B.35}$$

and for the $N_m - 1$ number of energy-coupling waves,

$$\hat{\mathbf{r}}_{3+N_m} = \begin{bmatrix} 0 \\ 0 \\ \vdots \\ 0 \\ 0 \\ 0 \\ 0 \\ -\frac{\kappa_2}{\kappa_1} \\ 1 \\ \vdots \\ 0 \\ 0 \\ 0 \\ \vdots \\ 0 \end{bmatrix}, \quad \ldots, \quad \hat{\mathbf{r}}_{1+2N_m} = \begin{bmatrix} 0 \\ 0 \\ \vdots \\ 0 \\ 0 \\ 0 \\ 0 \\ -\frac{\kappa_{N_m}}{\kappa_1} \\ 0 \\ \vdots \\ 1 \\ 0 \\ 0 \\ \vdots \\ 0 \end{bmatrix}, \tag{B.36}$$

and for the N_m number of volume fraction waves,

$$\hat{\mathbf{r}}_{2+2N_m} = \begin{bmatrix} 0 \\ 0 \\ \vdots \\ 0 \\ 0 \\ 0 \\ 0 \\ 0 \\ 0 \\ \vdots \\ 0 \\ 1 \\ 0 \\ \vdots \\ 0 \end{bmatrix}, \quad \hat{\mathbf{r}}_{3+2N_m} = \begin{bmatrix} 0 \\ 0 \\ \vdots \\ 0 \\ 0 \\ 0 \\ 0 \\ 0 \\ 0 \\ \vdots \\ 0 \\ 0 \\ 1 \\ \vdots \\ 0 \end{bmatrix}, \quad \ldots, \quad \hat{\mathbf{r}}_{1+3N_m} = \begin{bmatrix} 0 \\ 0 \\ \vdots \\ 0 \\ 0 \\ 0 \\ 0 \\ 0 \\ 0 \\ \vdots \\ 0 \\ 0 \\ 0 \\ \vdots \\ 1 \end{bmatrix}. \tag{B.37}$$

and the two transverse waves,

$$\hat{\mathbf{r}}_{2+3N_m} = \begin{bmatrix} 0 \\ 0 \\ \vdots \\ 0 \\ 0 \\ 1 \\ 0 \\ \frac{\hat{V}_{t_1}}{\kappa_1} \\ 0 \\ \vdots \\ 0 \\ 0 \\ 0 \\ \vdots \\ 0 \end{bmatrix}, \quad \hat{\mathbf{r}}_{3+3N_m} = \begin{bmatrix} 0 \\ 0 \\ \vdots \\ 0 \\ 0 \\ 0 \\ 1 \\ \frac{\hat{V}_{t_2}}{\kappa_1} \\ 0 \\ \vdots \\ 0 \\ 0 \\ 0 \\ \vdots \\ 0 \end{bmatrix}. \tag{B.38}$$

The corresponding Roe-averaged eigenvalues are,

$$\hat{\lambda}_{1,2} = \hat{u}_n \mp \hat{c}, \hat{\lambda}_3 = \hat{\lambda}_4 = ... = \hat{\lambda}_{3+3N_m} = \hat{u}_n, \tag{B.39}$$

and the corresponding Roe-averaged wave-strengths are,

$$\begin{aligned}
&\hat{W}_{1,2} = \frac{\Delta p \mp \hat{c}\sqrt{\rho_L \rho_R}\Delta u_n}{2\hat{c}^2}. \\
&\hat{W}_3 = \Delta(\alpha_1\rho_1) - \hat{z}_1\frac{\Delta p}{\hat{c}^2}, \quad \hat{W}_4 = \Delta(\alpha_2\rho_2) - \hat{z}_2\frac{\Delta p}{\hat{c}^2}, \quad ..., \quad \hat{W}_{2+N_m} = \Delta(\alpha_{N_m}\rho_{N_m}) - \hat{z}_{N_m}\frac{\Delta p}{\hat{c}^2}. \\
&\hat{W}_{3+N_m} = -\frac{\Delta p}{\hat{c}^2}\widehat{z_2 H_2} + \hat{K}\Delta(\alpha_2\rho_2) + \Delta(\alpha_2\rho_2 e_2), \\
&..., \quad \hat{W}_{1+2N_m} = -\frac{\Delta p}{\hat{c}^2}\widehat{z_{N_m} H_{N_m}} + \hat{K}\Delta(\alpha_{N_m}\rho_{N_m}) + \Delta(\alpha_{N_m}\rho_{N_m} e_{N_m}), \\
&\hat{W}_{2+2N_m} = \Delta\alpha_1, \quad \hat{W}_{3+2N_m} = \Delta\alpha_2, \quad ..., \quad \hat{W}_{1+3N_m} = \Delta\alpha_{N_m}, \\
&\hat{W}_{2+3N_m} = \sqrt{\rho_R\rho_L}\Delta u_{t_1}, \quad \hat{W}_{3+3N_m} = \sqrt{\rho_R\rho_L}\Delta u_{t_2}.
\end{aligned} \tag{B.40}$$

And lastly, the Roe-averaged values are,

$$
\begin{aligned}
&\hat{u}_n = \frac{(u_n)_L\sqrt{\rho_L} + (u_n)_R\sqrt{\rho_R}}{\sqrt{\rho_L}+\sqrt{\rho_R}}, \quad \hat{u}_{t_1} = \frac{(u_{t_1})_L\sqrt{\rho_L} + (u_{t_1})_R\sqrt{\rho_R}}{\sqrt{\rho_L}+\sqrt{\rho_R}}, \quad \hat{u}_{t_2} = \frac{(u_{t_2})_L\sqrt{\rho_L} + (u_{t_2})_R\sqrt{\rho_R}}{\sqrt{\rho_L}+\sqrt{\rho_R}},\\
&\hat{z}_k = \frac{z_{kL}\sqrt{\rho_L} + z_{kR}\sqrt{\rho_R}}{\sqrt{\rho_L}+\sqrt{\rho_R}}, \quad \widehat{z_k H_k} = \frac{(z_k H_k)_L\sqrt{\rho_L} + (z_k H_k)_R\sqrt{\rho_R}}{\sqrt{\rho_L}+\sqrt{\rho_R}},\\
&\widehat{u_n z_k} = \frac{(u_n z_k)_L\sqrt{\rho_L} + (u_n z_k)_R\sqrt{\rho_R}}{\sqrt{\rho_L}+\sqrt{\rho_R}}, \quad \widetilde{u_n z_k} = \frac{1}{2}(\hat{u_n}\hat{z}_k + \widehat{u_n z_k}),\\
&\widehat{u_{t_1} z_k} = \frac{(u_{t_1} z_k)_L\sqrt{\rho_L} + (u_{t_1} z_k)_R\sqrt{\rho_R}}{\sqrt{\rho_L}+\sqrt{\rho_R}}, \quad \widetilde{u_{t_1} z_k} = \frac{1}{2}(\hat{u_{t_1}}\hat{z}_k + \widehat{u_{t_1} z_k}),\\
&\widehat{u_{t_2} z_k} = \frac{(u_{t_2} z_k)_L\sqrt{\rho_L} + (u_{t_2} z_k)_R\sqrt{\rho_R}}{\sqrt{\rho_L}+\sqrt{\rho_R}}, \quad \widetilde{u_{t_2} z_k} = \frac{1}{2}(\hat{u_{t_2}}\hat{z}_k + \widehat{u_{t_2} z_k}),\\
&\hat{K} = \frac{\hat{u}_n^2 + \hat{u}_{t_1}^2 + \hat{u}_{t_2}^2}{2}, \quad \hat{V}_{t_1} = \sum_k \kappa_k \widetilde{u_{t_1} z_k}, \quad \hat{V}_{t_2} = \sum_k \kappa_k \widetilde{u_{t_2} z_k},\\
&\hat{c}^2 = \sum_k \widetilde{z_k c_k^2}, \quad \widetilde{z_k c_k^2} = \kappa_k(\widehat{z_k H_k} - \hat{K}\hat{z}_k) + \chi_k \hat{z}_k,
\end{aligned}
\tag{B.41}
$$

which we use to evaluate the normal-directed flux Jacobian, $\widehat{\mathbf{A}}_n = \mathbf{A}_n(\widehat{\mathbf{q}})$. We did not include in the eigenvectors the terms including π_k present in Eqn. (B.22), as they will not be used when we have a tabular EOS, as will be seen. In general, we assume an arbitrary relation for the pressure of the form $p_k = p_k(\rho_k, T_k)$, $\varepsilon_k = \varepsilon_k(\rho_k, T_k)$. In deriving the Jacobian matrix and corresponding eigenstructure, each material has been assumed to obey the differential expression,

$$dp_k = \chi_k d\rho_k + \kappa_k d\mathcal{E}_k. \tag{B.42}$$

Thus, the eigensystem has been written in terms of the thermodynamic derivatives χ_k, κ_k. For an ideal or stiffened gas, these thermodynamic derivatives are constants that may be chosen using fits to experimental data for each material. In general, however, these quantities are not constant, (i.e., $\chi_k = \chi_k(\rho_k, \mathcal{E}_k)$, $\kappa_k = \kappa_k(\rho_k, \mathcal{E}_k)$) and Roe-averaging these thermodynamic derivatives in Eqn. (B.41) is not straightforward. Arabi et al. [3] provide a very robust method for evaluating the speed of sound and evaluating the Roe flux without directly evaluating the Roe-averaged values $\hat{\chi}_k$ and $\hat{\kappa}_k$. This approach avoids entirely the complexity of other approaches, e.g., that of Vinkour and Montagné [45]. This approach relies on the observation that the concept of conservation,

$$\Delta\mathbf{f} = \hat{\mathbf{A}}\Delta\mathbf{q} = \sum_{j=1}^{n_w} \hat{\mathbf{r}}_j \hat{\lambda}_j \hat{W}_j, \tag{B.43}$$

can be used to replace the portions of the eigenstructure containing thermodynamic derivatives. Despite the presence of non-conservative terms that make the concept of conservation apply to the total energy rather than the specific components in the case of the six-equation model, we apply this relation to the phasic energy equations individually. This is a reasonable approach, as the non-conservative terms are only active in mixture regions of flow, outside of which conservation applies to each phasic energy equation. In doing this, we introduce the constraints on the energy

equations,

$$\Delta u(\alpha_k E_k + \alpha_k p_k) = (\widehat{z_k H_k} - \widehat{u z_k}\hat{c})(\hat{u} - \hat{c}) \left[\frac{\Delta(\alpha_1 p_1 + \alpha_2 p_2) - \hat{c}\sqrt{\rho_L \rho_R}\Delta u}{2\hat{c}^2} \right] + (\widehat{z_k H_k} + \widehat{u z_k}\hat{c})(\hat{u} + \hat{c}) \left[\frac{\Delta(\alpha_1 p_1 + \alpha_2 p_2) + \hat{c}\sqrt{\rho_L \rho_R}\Delta u}{2\hat{c}^2} \right] + X_k, \quad \text{(B.44)}$$

where X_k is a sum of eigen-expansion quantities that include the unknown quantities $\hat{\kappa_k}$, $\hat{\chi_k}$. To calculate the Roe flux for these equations, in the case of a tabular EOS, we calculate these terms as a whole as,

$$X_k = \Delta u(\alpha_k E_k + \alpha_k p_k) - (\widehat{z_k H_k} - \widehat{u z_k}\hat{c})(\hat{u} - \hat{c}) \left[\frac{\Delta(\alpha_1 p_1 + \alpha_2 p_2) - \hat{c}\sqrt{\rho_L \rho_R}\Delta u}{2\hat{c}^2} \right] - (\widehat{z_k H_k} + \widehat{u z_k}\hat{c})(\hat{u} + \hat{c}) \left[\frac{\Delta(\alpha_1 p_1 + \alpha_2 p_2) + \hat{c}\sqrt{\rho_L \rho_R}\Delta u}{2\hat{c}^2} \right], \quad \text{(B.45)}$$

where $\hat{c}$ has been calculated using a simple Roe-average for the quantities,

$$\widehat{\chi_k} = \frac{\chi_{kL}\sqrt{\rho_L} + \chi_{kR}\sqrt{\rho_R}}{\sqrt{\rho_L} + \sqrt{\rho_R}}, \qquad \widehat{\kappa_k} = \frac{\kappa_{kL}\sqrt{\rho_L} + \kappa_{kR}\sqrt{\rho_R}}{\sqrt{\rho_L} + \sqrt{\rho_R}}. \quad \text{(B.46)}$$

Then, we apply these terms to the Roe flux for the k-th energy equation as,

$$f^*_{E_k} = \frac{1}{2}[f_{E_k}(\mathbf{q}_L) + f_{E_k}(\mathbf{q}_R)] - \frac{1}{2}\left\{ \sum_{n=1}^{2} \left[|\hat{\lambda}_n| \hat{W}_n \hat{\mathbf{r}}_n \right]_{E_k} + \text{sign}(\hat{u}) X_k \right\}. \quad \text{(B.47)}$$

The nonconservative flux terms for the Roe flux are the same as for the LLF flux: for Eqn. (B.1), $\widehat{\vec{u}} = \frac{1}{2}(\vec{u}_L + \vec{u}_R)$, and for Eqn. (B.2), $\widehat{\alpha_k p_k} = \frac{1}{2}\left[(\alpha_k p_k)_L + (\alpha_k p_k)_R\right]$, and $\widehat{p} = \frac{1}{2}\left[p_L + p_R\right]$.

Results using the Roe flux for the sharp interface advection problem of Section 7.6 are shown in Figure B-10. These results demonstrate that the Roe flux is well-balanced. Additionally, we show results for the problems of Sections 7.11 and 7.12 in Figures B-11 and B-12. We encountered robustness issues running the problem of Section 7.13 with the Roe flux.

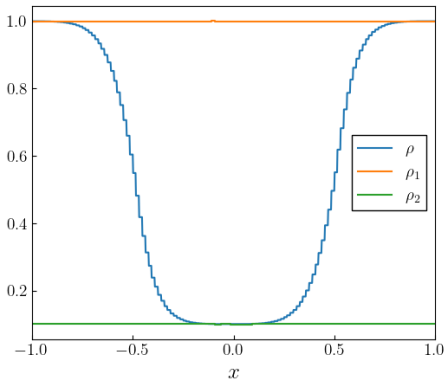

Density

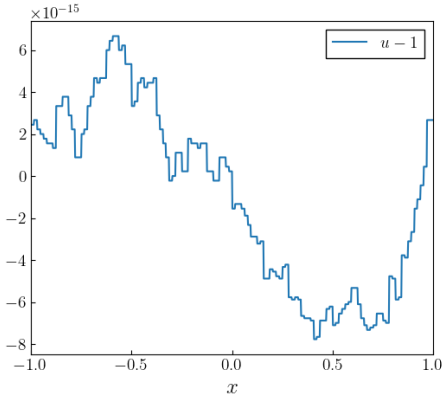

Velocity error

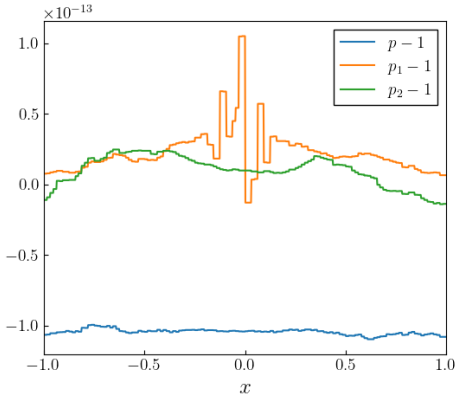

Pressure error

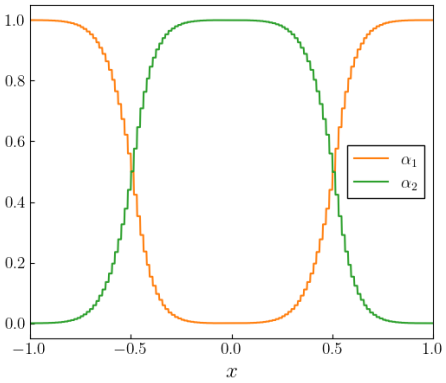

Volume fraction

Figure B-10. Primitive variable error profiles (b) and (c) and profiles (a) and (d) for the sharp 1-D interface advection problem (Config. 2) after 1 period using the spatial-averaging discretization (Section 3.4) with the Roe numerical flux.

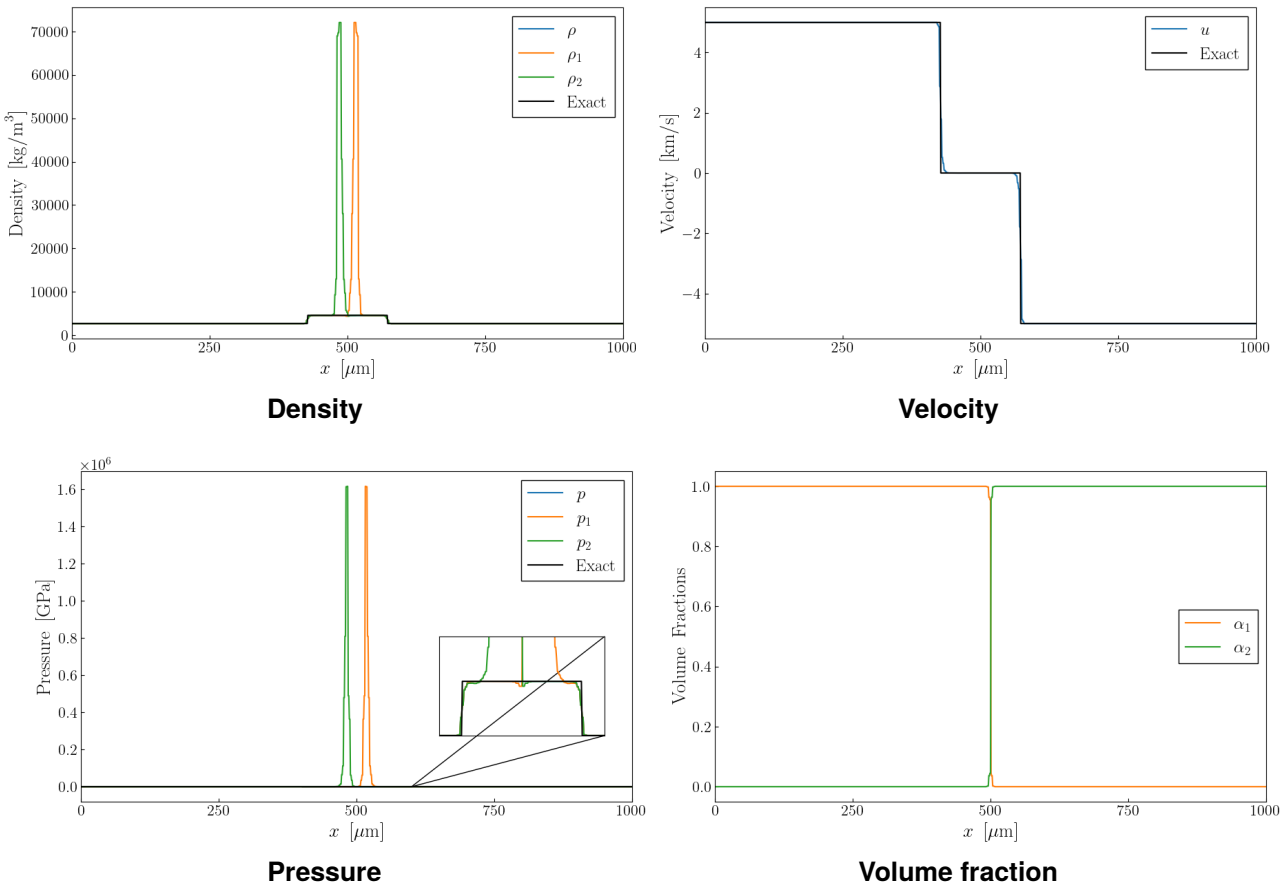

Figure B-11. Primitive variable profiles for the 1-D Al-Al collision problem at $t = 0.1$ s using the spatial-averaging discretization (Section 3.4) with the Roe numerical flux.

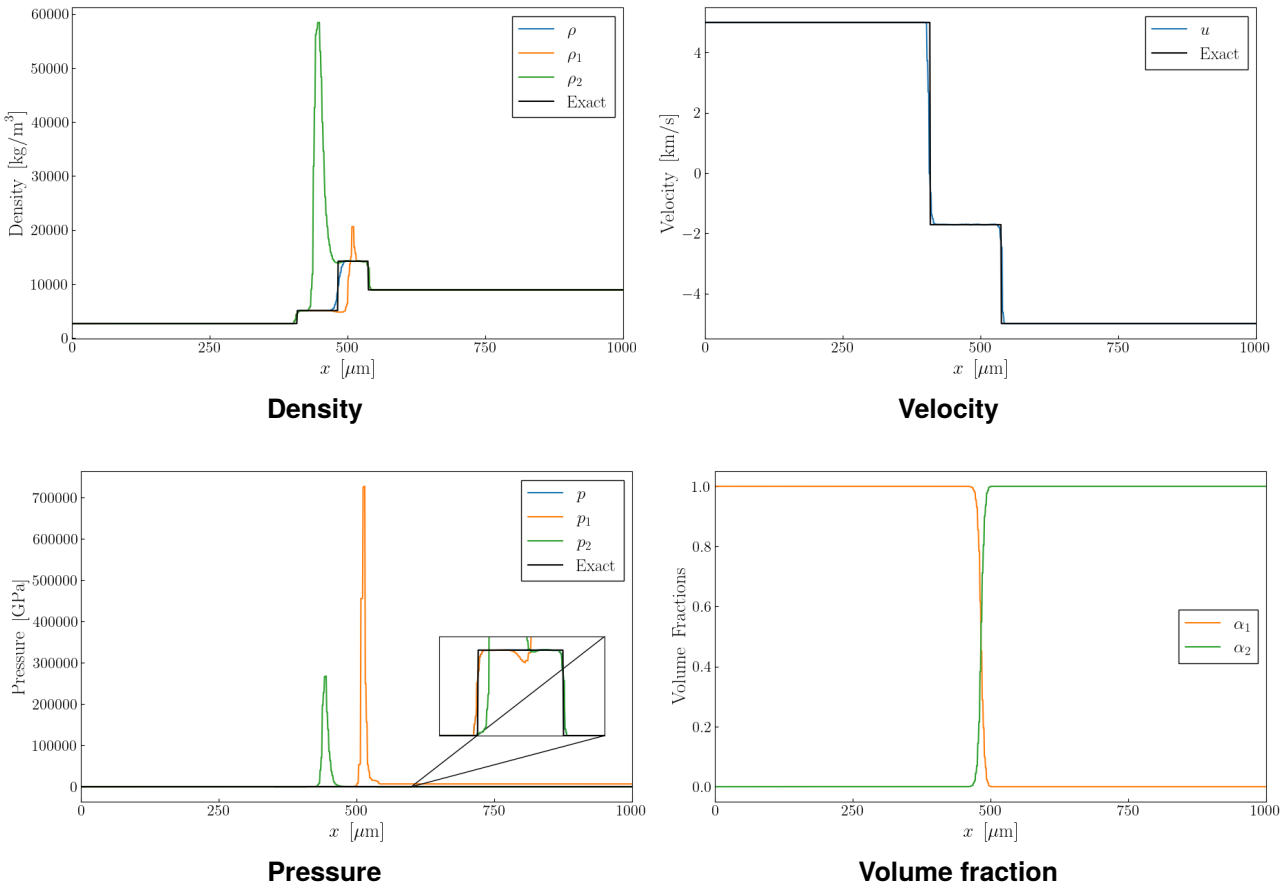

Figure B-12. Primitive variable profiles for the 1-D Al-Cu collision problem at $t = 0.1$ s using the spatial-averaging discretization (Section 3.4) with the Roe numerical flux.

DISTRIBUTION

Email—Internal

Name	Org.	Sandia Email Address
Technical Library	1911	sanddocs@sandia.gov

This page intentionally left blank.

Sandia National Laboratories

Sandia National Laboratories is a multimission laboratory managed and operated by National Technology & Engineering Solutions of Sandia LLC, a wholly owned subsidiary of Honeywell International Inc., for the U.S. Department of Energy's National Nuclear Security Administration under contract DE-NA0003525.